Linearly polarised photon beams at the BGO-OD experiment at ELSA

Dissertation
zur
Erlangung des Doktorgrades (Dr. rer. nat.)
der
Mathematisch-Naturwissenschaftlichen Fakultät
der
Rheinischen Friedrich-Wilhelms-Universität Bonn

von
Andreas Bella
aus
Bergisch Gladbach

Bonn, June 2016

Dieser Forschungsbericht wurde als Dissertation von der Mathematisch-Naturwissenschaftlichen Fakultät der Universität Bonn angenommen und ist auf dem Hochschulschriftenserver der ULB Bonn `http://hss.ulb.uni-bonn.de/diss_online` elektronisch publiziert.

1. Gutachter:	Prof. Dr. Hartmut Schmieden
2. Gutachter:	Priv. -Doz. Dr. Wolfgang Hillert

Tag der Promotion:	13.09.2016
Erscheinungsjahr:	2016

Abstract

The BGO-OD experiment, located at the electron stretcher facility ELSA in Bonn, is constructed for the study of meson photo-production reactions off the nucleon. The two main detector parts of the experimental setup are a central electromagnetic BGO calorimeter covering most of the solid angle and a magnetic spectrometer enclosing the most forward angles. This combination allows the detection of complicated mixed, charged and neutral, final states over almost the full solid angle and is optimised for the investigation of low momentum transfer processes at extreme forward angles. Physics proposals for the BGO-OD experiment include the measurement of the photon beam asymmetry Σ in different decay channels.

The highly energetic photon beam is produced from the electron beam of ELSA via the process of bremsstrahlung. Due to the continuous energy spectrum, the energy of the produced bremsstrahlung photon is a priori unknown. The energy E_γ corresponds to the difference between the energy E_0 of the incoming electron beam and the energy E_{e^-} of the post-bremsstrahlung electron. With a detector setup known as a photon tagger, consisting of a dipole magnet and a scintillator hodoscope, it is possible to measure the momentum of the post-bremsstrahlung electron and therefore to determine the energy of the produced bremsstrahlung photon.

The hodoscope of the BGO-OD photon tagger is designed, assembled and commissioned within this thesis. An energy range from $10\%E_0$ to $90\%E_0$ is covered with 120 plastic scintillators. The energy width of two adjacent scintillators ranges between $0.55\%E_0$ and $2.28\%E_0$. Since the post-bremsstrahlung electrons are detected with a time resolution of better than 210 ps, the tagger system also provides the time reference for the BGO-OD experiment.

Using a linearly polarised photon beam allows the measurement of the photon beam asymmetry. A linearly polarised photon beam can be achieved through coherent bremsstrahlung off a diamond crystal properly aligned with respect to the incoming electron beam. For the alignment of the crystal, the *Stonehenge technique* [1] performed with a goniometer system is made operational at the BGO-OD experiment within this thesis and has been successfully used since November 2014. Additionally, the C++ based program called COBRIS [2] used to determine the degree of polarisation of the produced bremsstrahlung photon beam is further improved. A more precise calculation of the degree of polarisation and the determination of its error based on the uncertainty of the input parameters is now possible.

A cross check on the determination of the degree of linear polarisation is performed through the measurement of the photon beam asymmetry in π^0 photo-production off the proton. The results are compared to calculations of the Bonn-Gatchina partial wave analysis [3], which is a representation of existing accurate measurements. The energy range from 1100 MeV to 1500 MeV was studied, in which the expected degree of linear polarisation amounts to at least $\sim 10\%$. From the comparison of the extracted photon beam asymmetries with the BnGn calculations it can be concluded, that the determination of the degree of linear polarisation is accurate at least within the errors of the extracted beam asymmetry. The relative error on the degree of polarisation derived from the error of the photon beam asymmetry is in the order of 10%. A more likely relative error of the degree of polarisation of $1\% - 2\%$ is determined from COBRIS.

Contents

CHAPTER 1

Introduction

Yukawa postulated in 1935 that the short range nuclear force can be explained through the exchange of a spinless and massive particle between the nucleons. Since the range of the nuclear force was known, the mass of the exchange particle was predicted to be $\sim$100 MeV. This particle is nowadays called π. The charged π was directly detected for the first time in cosmic rays by Cecil Powell in 1947. As soon as it was realised that pions can be produced in nuclear reactions using accelerators, several experiments were setup to characterise the π. Subsequently pion beams were used to perform pion scattering experiments off the nucleon to investigate the nuclear interaction. However, due to the intrinsic negative parity of the pion, it was not possible to access both parity states of excited nucleons which can be overcome by the use of real photon beams.

A common technique to produce real highly energetic photons is the process of bremsstrahlung off a nucleus. Via the process of coherent bremsstrahlung off a crystal also linearly polarised photons can be achieved. The complication of the bremsstrahlung process is its continuous energy spectrum. In the early stages, the energy of the bremsstrahlung photons could not be measured during the operation of the photo-production experiment, but only in dedicated photon flux measurements. The energy of the incoming bremsstrahlung photon and therefore the initial state of the photo-production process was unknown. Hence it was necessary to perform exclusive measurements, in which all particles of the final state of the reaction are detected.

An event-by-event based energy determination was possible with the development of high duty cycle electron accelerators and the design of a detector system called *photon tagger*. A *photon tagger* allows the determination of the energy of the produced bremsstrahlung photon event-by-event through the measurement of the momentum of the corresponding post-bremsstrahlung electron. Furthermore it is possible to determine the degree of linear polarisation of photons being produced via the coherent bremsstrahlung process through the measurement of bremsstrahlung spectra with the *photon tagger*.

The main part of this thesis documents the production and the commissioning of the photon tagger system as well as the production of linearly polarised photons, and the determination of their degree of polarisation for the currently operating BGO-OD[1] meson photo-production experiment located at the electron stretcher accelerator ELSA[2].

The total photoabsorbtion cross section off a proton target is plotted in figure 1.1 (red full circles) in dependence of the incoming photon beam energy (bottom axis) or, equivalently, of the square root of the Mandelstam variable s (top axis). Selected single and double meson final state cross sections are additionally shown. Enhancements in the cross section, which appear at specific values of the Mandelstam variable s, are visible for example for the $p\pi^0$ (blue full squares) and $p\eta$ (yellow full diamonds)

---

[1] **B**ismuth **G**ermanate **O**xide-**O**pen **D**ipole

[2] **EL**ectron **S**tretcher **A**ccelerator

final states. It may be assumed that in the energy regions of the enhancements the final state particles are produced through the excitation of the target proton and its subsequent decay. For other final states, for example for ΛK^+ photo-production (black empty circles), no outstanding structure is present in the total cross section. This behaviour may be explained instead through a dominant contribution of the t-channel exchange term.

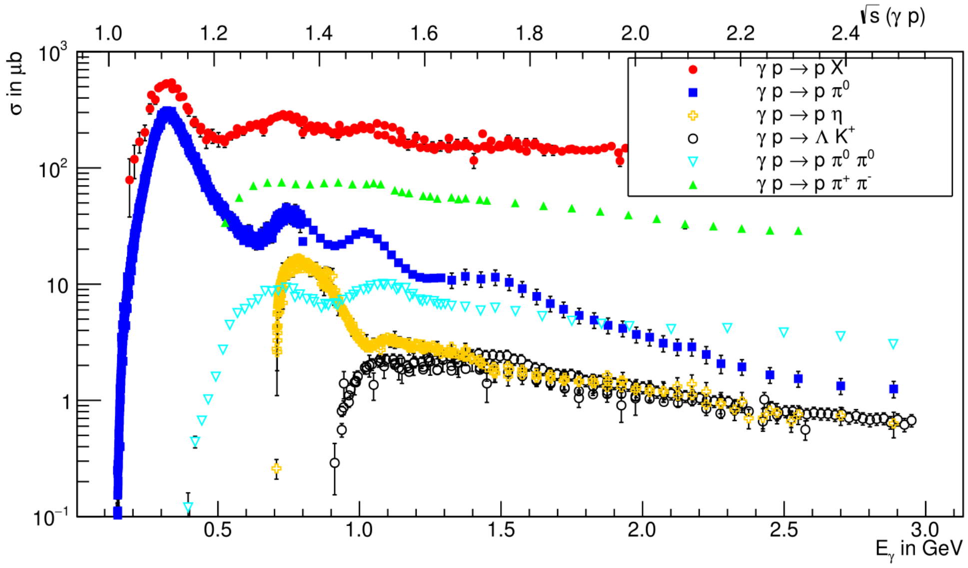

Figure 1.1: Total photoabsorption cross section off the proton [4] and total cross sections for selected final states [5–9].

The measurement of total and differential cross section is already a powerful tool to understand and characterise the dominant s- and t-channel mechanisms for a specific photo-production channel. To gather information concerning the non-dominant terms, the measurement of polarisation observables is required. Polarisation observables can be measured by the use of a polarised incoming photon beam, by the use of a polarised target and / or by the measurement of the polarisation of the recoiling baryon. In pseudo-scalar meson photo-production, 15 polarisation observables listed in table 1.1 can be measured. For a model independent description of meson photo-production processes, the differential cross section, the three single-polarisation observables Σ, T and P, and four carefully selected double-polarisation observables have to be measured according to [10].

Photon		Target			Recoil			Target-Recoil								
					x'	y'	z'	x'	x'	x'	y'	y'	y'	z'	z'	z'
		x	y	z				x	y	z	x	y	z	x	y	z
Unpolarized	$\frac{d\sigma_0}{d\Omega}$	–	T	–	–	P	–	$T_{x'}$	–	$L_{x'}$	–	Σ	–	$T_{z'}$	–	$L_{z'}$
Linearly	Σ	H	P	G	$O_{x'}$	T	$O_{z'}$	$L_{z'}$	$C_{z'}$	$T_{z'}$	G	σ	F	$L_{x'}$	$C_{x'}$	$T_{x'}$
Circularly	–	F	–	E	$C_{x'}$	–	$C_{z'}$	–	$O_{z'}$	–	E	–	H	–	$O_{x'}$	–

Table 1.1: The 15 polarisation observables in pseudo-scalar meson photo-production.

The single polarisation observable Σ, called photon beam asymmetry, can be measured by using a linearly polarised photon beam. The polarised differential cross section in dependence of the degree of polarisation $P_{\gamma,l}$ and of the photon beam asymmetry Σ is given by

$$\left(\frac{\mathrm{d}\sigma}{\mathrm{d}\Omega}\right)^{pol} = \left(\frac{\mathrm{d}\sigma_0}{\mathrm{d}\Omega}\right)^{unpol} \left[1 - P_{\gamma,l}(E_\gamma)\Sigma(E_{\gamma,\theta_M^{cms}})\cos 2\phi\right], \tag{1.1}$$

with the energy of the incident photon E_γ, the polar angle of the final state meson in the centre of mass system θ_M^{cms} and the azimuthal angle between the reaction plane and the incident photon polarisation vector ϕ.

A demonstrative illustration of the photon beam asymmetry Σ is given in [11], by an equivalent mechanism present in semi-inclusive deep inelastic scattering, with different degrees of freedom involved [12]. The origin of the $\cos 2\phi$ dependence of the cross section in pseudo-scalar meson photo-production using linearly polarised photon beams is ascribed to the spin-orbit interaction. The interaction appears between the spin of the final state baryon and the angular momentum of the final state meson. Depending on the potential $V = V_0 + V_{LS}\vec{L}\vec{S}$, the photon beam asymmetry Σ will be different from zero.

The photon beam asymmetry Σ is of special interest in this thesis, as it is used to perform a cross check on the determination of the linear degree of polarisation of the produced photon beam. Therefore the photon beam asymmetry Σ is determined in the final state $p + \pi^0$ measured with the BGO-OD setup, and compared to the BnGn solutions [3].

Experimental data provided by single- and double-polarisation experiments performed at BNL[3] and GRAAL[4] and currently operating at ELSA, JLAB[5], MAMI[6] and SPring-8[7] are used, for example by partial wave analysis (PWA) to determine excited baryon states [13]. Table 1.2 shows a list of newly added or further confirmed excited baryon states in the PDG[8] booklet. Large Hadron Collider beauty experiment The pattern of the baryon spectrum opened several questions which changed the point of view on the structure of the excited states. Why is the lowest positive parity excitation of the nucleon, N*(1440)1/2$^+$, lighter than its negative parity counterpart, N*(1535)1/2$^-$? Why is the Λ(1405)1/2$^-$

	PDG 2010	PDG 2012
N(1860)5/2$^+$		**
N(1875)3/2$^-$		***
N(1880)1/2$^+$		**
N(1895)1/2$^-$		**
N(1900)3/2$^+$	**	***
N(2060)5/2$^-$		**
N(2150)3/2$^-$		**
Δ(1940)3/2$^-$	*	**

Table 1.2: Newly added and confirmed baryon states in the PDG from 2012 compared to 2010. * = Evidence of existence is poor, ** = Evidence of existence is only fair, *** = Existence ranges from very likely to certain, but further confirmation is desirable and/or quantum numbers, branching fractions etc. are not well determined, **** = Existence is certain, and properties are at least fairly well explored.

---

[3] **B**rookhaven **N**ational **L**aboratory

[4] **Gr**enoble **A**nneau **A**ccèlèrateur **L**aser

[5] **J**efferson **Lab**oratory

[6] **Ma**inzer **Mi**crotron

[7] **S**uper **P**hoton **ring-8**GeV

[8] **P**article **D**ata **G**roup

lighter than the N*(1535)1/2$^-$, while the Σ(1620)1/2$^-$ is heavier? Discussion exist for several years if for example the Λ^*(1405) may be described by a genuine 3-quark object or a more complicated structure. Further interest is raised by recent observations of resonant states, which can not be interpreted as genuine $q\bar{q}$ mesons or qqq baryons. On the contrary, their quantum numbers are compatible with ones of systems built by $qq\bar{q}\bar{q}$ or $qqqq\bar{q}$ combinations. In the high energy region, this kind of states has been recently observed in several experiments:
the first one, called X(3872) was observed by Belle in 2003 and was initially interpreted as a loosely bound $D\bar{D}^*$ molecular state [14]. Several new states have been discovered by Belle, BaBar[9], BES III[10], CDF[11] etc., opening a recent field of research, namely the X,Y and Z meson sector.

Even more recently, the LHCb[12] collaboration observed a resonant state in the $\Lambda_b^0 \to J/\Psi K^- P$ decay, interpreted as a pentaquark [15].

The observation of all these states opened an intense discussion concerning their interpretation: some models would describe the newly discovered resonances as tetra(penta)-quarks; some others find a better description by the use of a molecular meson-meson(meson-baryon) bound state.

In the lower energy regime (< 3 GeV), hints for baryon-meson molecular states were also found at the CB[13]-ELSA/TAPS[14] experiment in the $K\Sigma$ final state [16]. A large drop in the $K^0\Sigma^+$ cross section was observed for small polar angles and at energies close to $K^{0*}\Sigma^+$ production threshold. One hypothesis is that a K^* is produced virtually in the t-channel mechanism and interacts at low momentum transfer with the produced hyperon until the K^* decays into a K and a rescattered π (see figure 1.2). Once the $K^{0*}\Sigma^+$ threshold is reached, real K^{0*} are produced and do no longer “feed” the K^0 channel anymore.

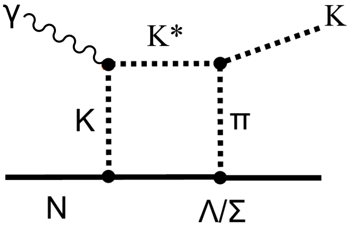

Figure 1.2: Subthreshold K^* production with subsequent coupling into the KΣ or KΛ channel through neutral or charged π rescattering.

The BGO-OD experiment is a newly commissioned meson photo-production experiment located at the electron stretcher facility ELSA in Bonn. It is assembled to study possible molecular baryon-meson states and to engage in the search for missing resonances with a broad variety of physics proposals. Many of them include the measurement of the photon beam asymmetry Σ and extended studies for associated strangeness photo-production.

The experimental setup includes two main detector parts: a central electromagnetic BGO calorimeter and a magnetic spectrometer including an open dipole magnet covering the most forward angles. This combination allows the detection of complicated mixed, charged and neutral, final states over almost the full solid angle and is optimised for the investigation of low momentum transfer processes at extreme forward angles.

---

[9] **B** **a**nd B-**bar**
[10] **Be**ijing **S**pectrometer III
[11] **C**ollider **D**etector at **F**ermilab
[12] **L**arge **H**adron **C**ollider **b**eauty
[13] **C**rystal **B**arrel
[14] **T**wo **A**rm **P**hoton **S**pektrometer

The electron beam provided by ELSA is used to produce a highly energetic photon beam via the process of bremsstrahlung. The process of incoherent bremsstrahlung off an amorphous radiator as well as the one of coherent bremsstrahlung off a crystal is presented in chapter 2.

Since the bremsstrahlung spectrum is continuous, a detector setup called *photon tagger* is required to determine the energy of the produced bremsstrahlung photons. In the third chapter, the ELSA facility, the principle of the photon tagger and its components, and the BGO-OD experiment are introduced.

Within this work, the *photon tagger* is designed, assembled and commissioned. The steps of the production and the commissioning of the *photon tagger* are documented in chapter 4.

The measurement of the photon beam asymmetry Σ requires the use of a linearly polarised photon beam. The details of the procedure for the production of the linearly polarised photon beam through coherent bremsstrahlung and the determination of the polarisation degree are presented in chapter 5.

A cross check of the determination of the produced photon beam's degree of polarisation is performed through the measurement of the photon beam asymmetry Σ in π^0 photo-production off the proton. Results from the analysis of the data sample taken in June/July 2015 are shown and compared with BnGn calculations in chapter 6.

CHAPTER 2

Bremsstrahlung

Photo-production experiments like the BGO-OD experiment use a highly energetic photon beam. A commonly used photon beam production mechanism is the process of bremsstrahlung of an electron beam.

In this case, electrons passing through material get decelerated and lose their energy by emitting bremsstrahlung photons. Because of four momentum conservation, the presence of a third particle (e.g. a nucleus), which takes the recoil momentum, is necessary. Figure 2.1 shows the lowest order Feynman graphs for the process of bremsstrahlung.

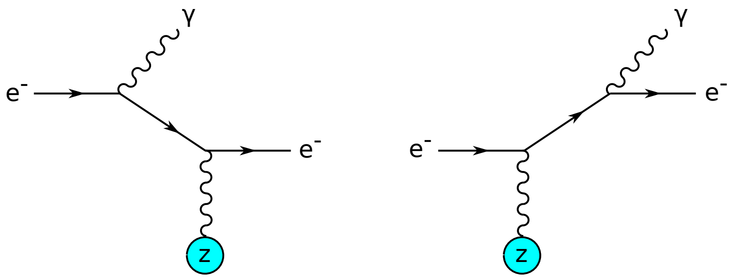

Figure 2.1: Feynman graph of lowest order for the bremsstrahlung process.

The electrical field vector of the bremsstrahlung photon lies in the plane which is spanned by the recoil momentum and the momentum of the incident electron. If an amorphous radiator is used for the production of incoherent bremsstrahlung, the distribution of collisions and the orientations of the recoil are isotropic meaning that no scattering planes are preferred. This leads to no effective linear polarisation of the photon beam. Taking advantage of the coherent bremsstrahlung process by using a crystal instead of an amorphous radiator, production of linearly polarised photon beams is possible.

In this chapter the kinematical conditions and the cross section for the incoherent bremsstrahlung process will be presented first. Subsequently, the modification of the cross section for coherent bremsstrahlung followed by the determination of the photon beam degree of polarisation will be illustrated. Since the degree of polarisation depends strongly on the orientation of the crystal with respect to the momentum of the primary electron beam, the necessary conditions of the crystal's orientation are described at the end of this chapter. The description of bremsstrahlung kinematics and cross sections is a complicated topic and therefore only the main formulas will be given. Detailed derivations and calculations can be found in [17], [18] and [19].

2.1 Incoherent Bremsstrahlung

2.1.1 Kinematics

For the bremsstrahlung process on a generic scattering partner N

$$e^- + N \to e^- + N + \gamma,$$

the energy-momentum conservation can be written as

$$E_0 = E + k + T \tag{2.1}$$

$$\vec{p}_0 = \vec{p} + \vec{k} + \vec{q} \tag{2.2}$$

where:

$E_0,\ \vec{p}_o$ = energy and momentum of the incident electron
$E,\ \vec{p}$ = energy and momentum of the outgoing electron
$k, \vec{k}$ = energy and momentum of the bremsstrahlung photon
$T, \vec{q}$ = recoil energy and momentum of the scattering partner.

For recoil momenta of $q \approx mc$, the recoil energy of $T = q^2/2M_N \approx 10^{-5}$ MeV can be neglected. However, the kinematically allowed range of the recoil momentum is very important for the coherent bremsstrahlung process of a crystal (see section 2.2). In the following, the limits of the recoil momentum are going to be deduced. Due to rotational symmetry with regard to the direction of the incident electrons it is possible to split the recoil momenta into longitudinal and transversal components, q_l and q_t, which is shown in figure 2.2.

$$q_l = p_0 - p\cos\theta_e - k\cos\theta_k \tag{2.3}$$

$$q_t^2 = p^2 \sin^2\theta_e + k^2 \sin^2\theta_k + 2pk\sin\theta_e \sin\theta_k \cos\psi \tag{2.4}$$

with:

$$\theta_e = \angle(\vec{p}_0, \vec{p}) \tag{2.5}$$

$$\theta_k = \angle(\vec{p}_0, \vec{k}) \tag{2.6}$$

$$\psi = \angle(\vec{p}_0, \vec{p})(\vec{p}_0, \vec{k}) \tag{2.7}$$

For highly energetic electrons, the produced bremsstrahlung photons will be emitted at small angles in forward direction. For $\theta_e \cong \theta_k \cong 0$, the transversal component of the recoil momentum tends to zero, while a sharp lower limit for the longitudinal component is obtained. This limit depends on the energy of the incident electron and of the emitted bremsstrahlung photon. The following approximation can be made[1] for high energies

$$p = \sqrt{E^2 - 1} \sim E - \frac{1}{2E} \quad \text{for} \quad (E_0, E \gg 1). \tag{2.8}$$

Using the relative photon energy $x = \frac{k}{E_0}$, the lower recoil boundary for the longitudinal component can

---

[1] The units which are used are given in the appendix A

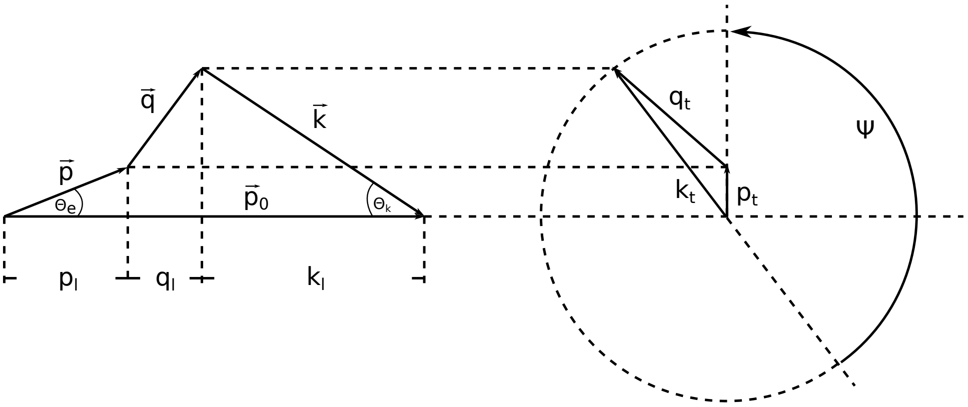

Figure 2.2: Kinematic of the bremsstrahlung process split into longitudinal and transversal components.

be expressed through

$$\delta(x) \equiv q_l^{min} = \frac{1}{2E_0}\frac{x}{1-x}. \tag{2.9}$$

Replacing θ_k by the characteristic opening angle θ_γ[2]$= m_e/E_0$ in equation 2.3, applying small angle approximation and neglecting q compared to p_0, p and k, the electron emission angle is given by

$$\theta_e = \frac{k}{EE_0} = \frac{1}{E_0}\frac{x}{1-x}. \tag{2.10}$$

Using the relativistic approximation $p = E$, an upper limit for the longitudinal recoil component is obtained

$$q_l^{max} \approx \frac{1}{E_0}\frac{x}{1-x} = 2\delta(x). \tag{2.11}$$

The transversal component has its maximum at $\psi = 0$ and its minimum at $\theta_e = \theta_k = 0$. The boundaries

$$0 \leq q_t \leq 2x$$

are obtained for q_t.

A more precise calculation of the recoil momentum limits can be found in [17]. In the following the results are summarised. The maximum transversal recoil momentum

$$q_t^{max} = \sqrt{2E_0(q_l - \delta(x))} \tag{2.12}$$

leads to the more precise recoil momentum limits

$$\delta(x) + \frac{(q_t^{max})^2}{2E_0} \leq q_l \leq \frac{\delta(x)}{x} \tag{2.13}$$

$$0 \leq q_t \leq 1 = q_t^{max}. \tag{2.14}$$

The approximated recoil momentum limits as well as the more precise calculations from [17] are illustrated in figure 2.3. These limits describe the kinematically allowed region of the bremsstrahlung process called *pancake* (see [20]). For a fixed longitudinal recoil momentum, a maximum relative photon energy for which the total recoil momentum is still lying in the kinematically allowed region is

---

[2] Half of the intensity is emitted in a cone with a half angle of the characteristic angle $\theta_\gamma = m_e/E_0$

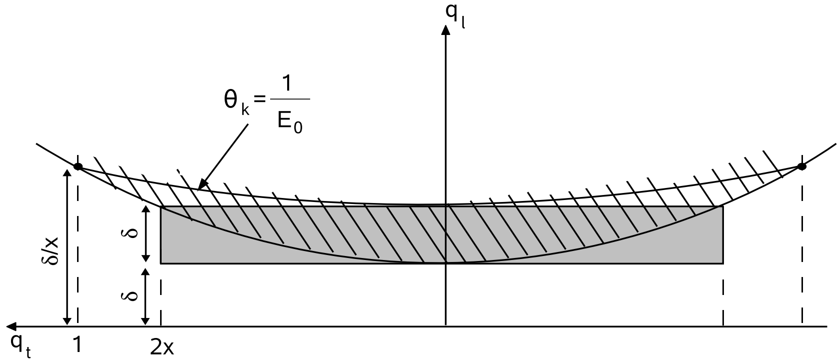

Figure 2.3: Schematical representation of the kinematically allowed region of the bremsstrahlung process. The grey box indicates the allowed region for q$_l$ and q$_t$ according to the approximation. The allowed region for q$_l$ and q$_t$ according to the precise calculation [17] is shown by the hatched shape. Since $q_l << q_t$ the q$_t$-axis is strongly compressed.

given by

$$x_d = \frac{2E_0 q_l}{1 + 2E_0 q_l}. \tag{2.15}$$

The cross section falls to zero if the relative photon energy is higher than x_d.

2.1.2 The incoherent Cross Section

Generally, the cross section of a scattering process of an electron off a nucleus with electromagnetic charge Z is described by

$$\sigma = \frac{|M_{if}|^2 \cdot \text{phase space factor}}{\text{time} \cdot \text{particle flux}} \tag{2.16}$$

$|M_{if}|$ denotes the matrix element, which describes the probability of the scattering process. According to [18], the cross section for incoherent bremsstrahlung is

$$\frac{d^3\sigma}{dk d\Omega_k d\Omega_p} = \frac{\alpha}{(2\pi)^4} \frac{E_0 E p k}{p_0} \left(\frac{\hbar}{mc}\right)^2 |M_{if}|^2 \tag{2.17}$$

and writing explicitly $|M_{if}|^2$, one gets

$$\begin{aligned}\frac{d^3\sigma_B}{dk d\Omega_k d\Omega_p} = \frac{\alpha Z r_0^2}{4\pi^2} \frac{p}{k p_0 q^4} \Bigg(&(4E^2 - q^2) \frac{p_0^2 \sin^2\theta_0}{(E_0 - p_0 \cos\theta_0)^2} (4E_0^2 - q^2) \frac{p^2 \sin^2\theta}{(E - p\cos\theta)^2} \\ &+ (4E_0 E - q^2 + 2k^2) \frac{2 p_0 p \sin\theta_0 \sin\theta \cos\phi}{(E_0 - p_0 \cos\theta_0)(E - p\cos\theta)} \\ &+ 2k^2 \frac{p_0^2 \sin^2\theta_0 + p^2 \sin^2\theta}{(E_0 - p_0 \cos\theta_0)(E - p\cos\theta)} \Bigg).\end{aligned} \tag{2.18}$$

with:

α = Electromagnetic coupling constant
r_0 = Classical electron radius
p_0, E_0 = Momentum and energy of incident electron
p, E = Momentum and energy of scattered electron
k = Energy of the bremsstrahlung photon
q = Transferred recoil momentum
θ_0 = Photon opening angle
θ = Scattered electron opening angle
ϕ = Angle between p_0 and p.

This is the Bethe-Heitler cross section. The cross section shows a dependency on the fourth power of the recoil momentum. Hence, small recoil momenta contribute to the cross section more than high recoil momenta. This dependency will be important for the coherent bremsstrahlung process off a crystal. An integration over all emission angles leads to the spectral distribution [19]

$$d\sigma_{B.H.} = 4Z^2\alpha a_0^2 \frac{dk}{k}\frac{E}{E_0}\left[\frac{E_0}{E} + \frac{E}{E_0 - \frac{2}{3}}\right]\left[ln\left(\frac{2E_0E}{k}\right) - \frac{1}{2}\right]. \tag{2.19}$$

In first approximation the bremsstrahlung spectrum is proportional to $1/k$.

The Bethe-Heitler cross section is derived under the assumption of a pure Coulomb potential generated by the electromagnetic charge of the nucleus. It has to be considered that the nucleus is screened by the shell electrons and hence, the proton number Z has to be replaced in the Bethe-Heitler cross section by Z[1-F(q)]. The formfactor F(q) describes the charge distribution of the shell electrons and thus the screening of the nucleus. F(q) is given by

$$F(q) = \int \rho(r) e^{-i\vec{q}\vec{r}} d^3r. \tag{2.20}$$

A detailed discussion about the consideration of screening especially on the coherent bremsstrahlung cross section by using various parametrisations for the formfactor is available in [21].

2.2 Coherent Bremsstrahlung

Linearly polarised photons can be obtained via the process of coherent bremsstrahlung using a crystalline radiator which has a periodical arrangement of atoms. Due to the lattice structure of a crystalline radiator, the cross section is modified. The degree of polarisation depends strongly on the orientation of the crystalline radiator relative to the primary electron beam.

2.2.1 Kinematics

The periodic arrangement of the atoms in the lattice of a crystal radiator allows, under proper conditions, constructive interference between the bremsstrahlung amplitudes of individual atoms. Similar to the Mößbauer effect [22], the recoil momentum gets absorbed practically recoilless by the whole crystal, with a mass much higher than the mass of a single atom. Hence, the recoil energy can be neglected. This process is called “coherent”, since the photon gets produced in a process where many indistinguishable atoms are involved. Similar to the scattering of X-rays, for recoil momenta which are equal to a multiple of a reciprocal lattice vector, the process of coherent bremsstrahlung fulfils the Laue-Bragg condition

$$\vec{q} = n \cdot \vec{g}. \tag{2.21}$$

Here $\vec{q}$ denotes the recoil momentum and $\vec{g}$ a reciprocal lattice vector. A reciprocal lattice vector describes a group of parallel planes in position space, while the components of the reciprocal lattice vector are given by the Miller indices [23]. As shown in equation 2.18, small recoil momenta contribute more to the cross section. Hence, small lattice vectors are preferred. As in the case of incoherent bremsstrahlung, the recoil momenta has to remain within the kinematical allowed *pancake* region.

2.2.2 The coherent Cross Section

In the bremsstrahlung process, atoms can be kicked out of the lattice and therefore the recoil is not taken by the full crystal. Additionally, real crystals have already lattice defects. Further deviations from a periodic structure are caused by thermal excitations which leads to zero-point oscillations of the atoms in the grid. Consequently, scattering of single atoms is possible resulting in the production of incoherent bremsstrahlung. Hence, the bremsstrahlung cross section from a crystal has to be written as the sum of

$$d\sigma_{crystal} = d\sigma_{coherent} + d\sigma_{incoherent}. \tag{2.22}$$

The effective cross section is composed of

- **the diffraction factor**
  The Bethe-Heitler cross section is extended by the diffraction factor to describe the coherent bremsstrahlung off a crystal

  $$d\sigma_N(\vec{q}) = D(\vec{q}) \cdot d\sigma(\vec{q}). \tag{2.23}$$

  It considers, that N atoms contribute simultaneously to the scattering process. For a large number of participating atoms the diffraction factor is written according to [17] as

  $$D(\vec{q}) = \left(\frac{2\pi}{a}\right)^3 \sum_{h_{kl}} \prod_{k=1}^{3} N_k \cdot \delta\left(q_k - \frac{2\pi h_{kl}}{a}\right). \tag{2.24}$$

  Here a stands for the lattice constant and h_{kl} the Miller indices of the reciprocal lattice vector. The δ-function works like the Laue-Bragg condition, which only allows scattering processes, where the recoil momentum is equal to a multiple of a reciprocal lattice vector.

- **the structure factor**
  Due to the structure of the crystal, contributions of different lattice planes will interfere with each other. Interference effects are taken into account by the structure factor $S(\vec{g})$ which for diamond is given by [17]

  $$S(\vec{g}) = [1 + e^{i\pi/2(h_1+h_2+h_3)}][1 + e^{i\pi(h_2+h_3)} + e^{i\pi(h_3+h_1)} + e^{i\pi(h_1+h_2)}]. \tag{2.25}$$

  Here h_i are the components of the reciprocal lattice vector $\vec{g}$. The selection rules for the structure factor are

  1. $|S(\vec{g})| = 64$, if h, k, l are even and (h + k + l) can be divided by four.

2. $|S(\vec{g})| = 32$, if all h, k, l are odd
3. $|S(\vec{g})| = 0$ for all other cases.

Using equations 2.24 and 2.25, the cross section 2.23 can be written as

$$d\sigma_N(\vec{q}) = \left(\frac{2\pi}{a}\right)^3 \frac{N}{8}\left[\sum_{g_v} |S(\vec{g})| \cdot \delta(\vec{q} - \vec{g_v})\right] \cdot d\sigma(\vec{q}). \tag{2.26}$$

- **the Debye-Waller factor**
  Similar to the Mößbauer-Effekt, the fraction of the recoilless contribution in the bremsstrahlung process off a crystal is given by the Debye-Waller factor

  $$f(q^2) = e^{-A(T)q^2}. \tag{2.27}$$

  The periodicity of the lattice is disturbed by zero-point oscillations due to thermal excitations. The mean displacement of the atoms in the crystal is described by

  $$A(T) = \frac{3m_e^2c^2}{4Mk_b\Theta}\left[1 + 4\frac{T}{\Theta}\Psi\left(\frac{\Theta}{T}\right)\right]. \tag{2.28}$$

  M is the mass of the atom, m_e the electron mass, k_b Boltzmann constant, T the temperature and Θ the Debye temperature. $\Psi(\frac{\Theta}{T})$ is the Debye function, which is defined in [24] as

  $$\Psi\left(\frac{\Theta}{T}\right) = \frac{T}{\Theta}\int_0^{\frac{\Theta}{T}} \frac{tdt}{e^t - 1} \tag{2.29}$$

  The incoherent part contributes with $(1 - f)$ to the crystal cross section. According to equation 2.27 and 2.28, the Debye-Waller factor decreases with increasing temperature. An improvement of the coherent bremsstrahlung contribution can be achieved by choosing a crystal with a high Debye temperature. For this reason Diamond ($\Theta = 2230K$) is preferred to other materials like Beryllium ($\Theta = 1160K$) and Silicon ($\Theta = 640K$).

- **the resulting coherent cross section**
  Including all above aspects, the total cross section for coherent and incoherent bremsstrahlung off a diamond can be written as

  $$d\sigma_{crystal}(\vec{q}) = \left[\frac{1}{8}\left(\frac{2\pi}{a}\right)^3 e^{-Aq^2}\sum_{\vec{g}_v} |S(\vec{g})|^2 \cdot \delta(\vec{q} - \vec{g_v}) + (1 - e^{-Aq^2})\right] \cdot d\sigma(\vec{q}) \tag{2.30}$$

  $$= d\sigma_{coherent} + d\sigma_{incoherent}. \tag{2.31}$$

2.2.3 Orientation of the Crystal with Respect to the Electron Beam

The orientation of the crystal with respect to the primary electron beam is important, as it affects the degree of polarisation of the produced bremsstrahlung photon beam. The relation between the crystal axes $\vec{b_1}, \vec{b_2}$ and $\vec{b_3}$, corresponding to the reciprocal lattice vectors [1,0,0], [0,1,0] and [0,0,1] of the crystal, and the momentum of the primary electron beam $\vec{p_0}$ is shown in figure 2.4. The orientation of

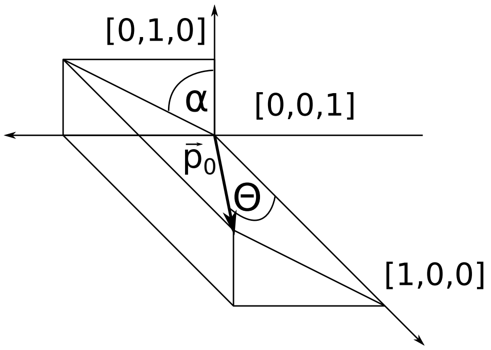

Figure 2.4: Schematical representation of the orientation of the crystal with respect to the primary electron beam in momentum space.

the crystal can be described in the following

$$\theta = (\vec{p_0}, \vec{b_1}) \tag{2.32}$$

$$\alpha = (\vec{b_1}, \vec{b_2})(\vec{p_0}, \vec{b_1}). \tag{2.33}$$

The parameters α and θ can be adjusted with a goniometer system which is going to be introduced in section 3.1.3. Generally, three different orientations can be distinguished:

1. **$\alpha = \theta = 0$ (figure 2.5):** for these angles, $\vec{b_1}$ and $\vec{p_0}$ are parallel to each other. In this orientation, several reciprocal lattice vectors lie in the kinematical allowed region and the intensity spectra are called *multipoint spectra*. The first lattice vectors lie on the lower sharp boundary of the *pancake* at $\delta = \frac{2\pi}{a}$. For the nominal ELSA electron energy of $E_0 = 3.2\,\text{GeV}$, this corresponds to $x_d = 0.978$. As shown in figure 2.8 the intensity peaking for this value of x_d is so small that no effective polarisation occurs.

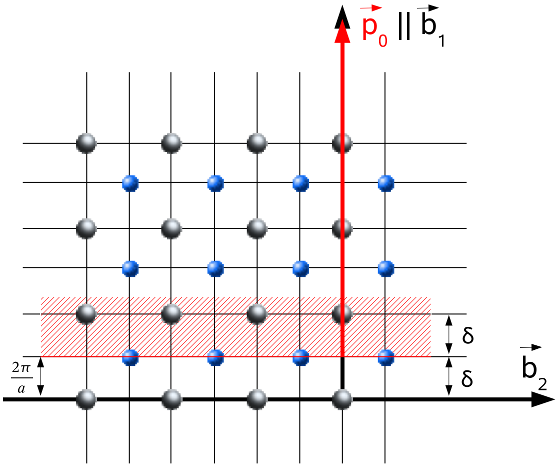

Figure 2.5: Relative orientation of the reciprocal lattice with respect to the primary electron beam momentum for the case $\theta = \alpha = 0$. $\vec{b_1}$, $\vec{b_2}$ and $\vec{b_3}$ denote the unit vectors of the reciprocal lattice, $\vec{p_0}$ is the momentum of the incident electron beam, a the lattice constant. The points represent the reciprocal lattice vectors while the hatched area displays the *pancake*.

2. **$\alpha = 0$ and $\theta \ll 1$ (figure 2.6):** in this orientation the *pancake* crosses the $\vec{b_2}\vec{b_3}$-plane. The first row of lattice vectors extended in the direction of $\vec{b_3}$ lies at $\tau^{-1} = \frac{\delta}{\theta} = \frac{4\pi}{a}$ on the lower sharp limit of the *pancake*. With $E_0 = 3.2\,\text{GeV}$, this corresponds to $x_d = 0.465$. In this region, large intensity peaking is possible, but several scattering planes can be perpendicular to each other. Hence, no or small effective polarisation is obtained.

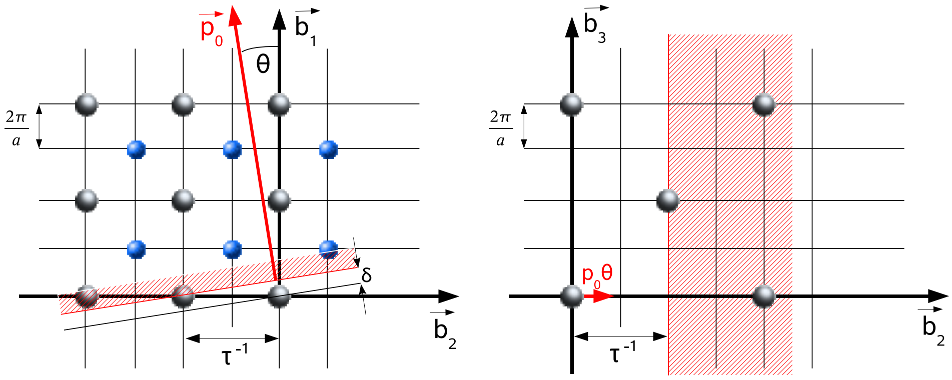

Figure 2.6: Relative orientation of the reciprocal lattice with respect to the primary electron beam momentum for the case $\theta \ll 1$ and $\alpha = 0$. Lattice vectors in $\vec{b}_3$ direction contributes to a multipoint spectrum leading to no or small polarisation.

3. **$\alpha < 1$ and $\theta \ll 1$ (figure 2.7):** it is possible to select one single lattice vector by choosing $\alpha \neq 0$. Intensity spectra which are caused by one single lattice vector are called *one point spectra*. It is possible to rotate the crystal such that for example only the [022] vector lies on the lower boundary of the *pancake*. The intensity peaking is not as high as for the *multipoint spectra*, but due to the fact, that only one lattice vector contributes to the intensity spectrum, a high degree of polarisation can be achieved.

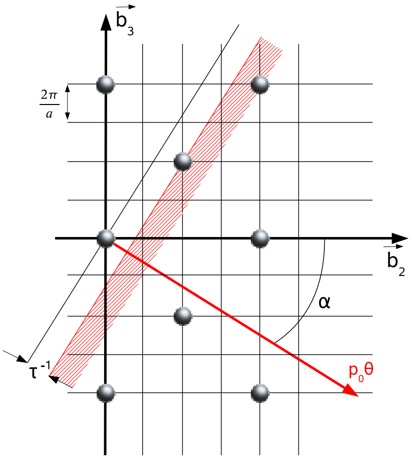

Figure 2.7: Relative orientation of the reciprocal lattice with respect to the primary electron beam momentum for the case $\theta \ll 1$ and $\alpha < 1$. The selection of one lattice vector is possible and a high degree of polarisation is obtained.

2.2.4 Intensity Distribution of Incoherent and Coherent Bremsstrahlung

Using a crystal radiator, the relative intensity distribution of bremsstrahlung can be written, according to [17] and [25], as the sum of the cross sections which includes the linear polarised contributions perpendicular $\sigma_\perp$ or parallel $\sigma_\parallel$ to a reference plane

$$I = \frac{k}{\sigma_0}\frac{d\sigma_{cry}}{dk} = \frac{k}{\sigma_0}\frac{d\sigma^{\parallel} + d\sigma^{\perp}}{dk} = (1+(1-x)^2)(\Psi_1^c + \Psi_1^{inc} + \Psi_1^{inc,e}) - \frac{2}{3}(1-x)(\Psi_2^c + \Psi_2^{inc} + \Psi_2^{inc,e}), \quad (2.34)$$

with $\sigma_0 = (\frac{Z^2}{137})(\frac{e^2}{mc^2})^2$ and k = photon energy. The incoherent distribution is described by the functions $\Psi^{inc}_{1,2}$. According to [17] $\Psi^{inc}_{1,2}$ can be approximated by $\Psi^{inc}_1 = 14.1$ and $\Psi^{inc}_2 = 13.2$. In addition to the incoherent distribution, the intensity distribution of shell electrons, which is called the electron-electron bremsstrahlung has to be considered, too. According to [26], these contributions are $\Psi^{inc,e}_1 = 4.1$ and $\Psi^{inc,e}_2 = 4.0$. The approximations are valid for a diamond radiator.

The functions $\Psi^c_{1,2}$ describe the coherent contribution and are given through

$$\Psi^c_1 = \frac{1}{2}\frac{(2\pi)^2}{a^3}\delta(x)\sum_{\vec{g}}|S(\vec{g})|^2 e^{-Ag^2}\frac{(1-F(g^2))^2}{g^4}\frac{q_t^2}{q_l^2} \tag{2.35}$$

$$\Psi^c_2 = 3\frac{(2\pi)^2}{a^3}\delta(x)^2\sum_{\vec{g}}|S(\vec{g})|^2 e^{-Ag^2}\frac{(1-F(g^2))^2}{g^4}\frac{q_t^2(q_l-\delta(x))}{q_l^4}, \tag{2.36}$$

being $\delta(x)$ already defined in section 2.1.1. The summation is only performed over reciprocal lattice vectors which are located inside the *pancake* area. As mentioned before, it is possible to determine a relative photon energy x_d for each lattice vector, for which the cross section falls discontinuously to zero. The intensity distribution has its maximum at $x = x_d$, because Ψ^c_2 is zero due to $q_l = \delta$. The resulting intensity distribution at the discontinuity for different reciprocal lattice vectors is according to [17]

$$I^c_{x_d} = \chi(x_d)\cdot E_0\frac{(2\pi)^2}{a^3}|S|^2 e^{-Ag^2} g^2 F(g^2) \tag{2.37}$$

with

$$\chi(x_d) = [1 + (1-x_d)^2](1-x_d)/x_d. \tag{2.38}$$

The enveloped curve is shown in figure 2.8, which grows for $x_d \to 0$, but falls to zero for $x_d \to 1$. For relative photon energies which are smaller than the discontinuity, the intensity spectrum is described by

$$I^c(x, x_d) = \chi(x, x_d)\cdot E_0\frac{(2\pi)^2}{a^3}|S|^2 e^{-Ag^2} g^2 F(g^2) \tag{2.39}$$

with

$$\chi(x, x_d) = \frac{xQ^2}{1-x}\left(1 + (1-x)^2 - \frac{4x^2Q^2}{1-x}\left(\frac{(1-x)}{xQ} - 1\right)\right), \quad Q = \frac{1-x_d}{x_d}. \tag{2.40}$$

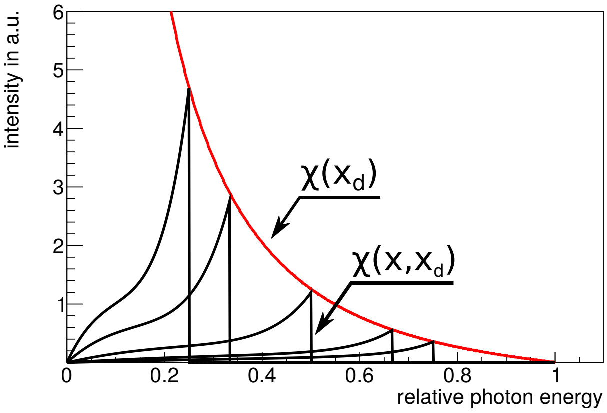

Figure 2.8: $\chi(x, x_d)$ (eq. 2.40) describes the coherent one-point intensity contribution depending on the photon energy for five different orientations of the same lattice vector. Shown in red is $\chi(x_d)$ (eq. 2.38), the maximum intensity contribution in dependence of x$_d$. The normalisation is arbitrary.

Figure 2.9a shows a one-point bremsstrahlung spectrum (see section 2.2.3) off a diamond compared with the one off an amorphous bremsstrahlung radiator. The crystalline spectrum consists of an incoherent part which behaves exactly as for the amorphous radiator case, and several coherent peaks originating from different contributing reciprocal lattice vectors. According to the coherent bremsstrahlung cross section and the structure function, the strongest contributing reciprocal lattice vector is the [0,2,2]. The position and the extension of the *pancake* on the reciprocal lattice depends on the produced bremsstrahlung photon energy (see eq. 2.9 and section 2.2.3). Hence, for higher photon energies other reciprocal lattice vectors lie in the *pancake* and therefore contribute to the diamond bremsstrahlung spectrum. The calculations presented in this chapter do not consider experimental conditions like for example primary electron beam divergence or multiple scattering in the radiator. If these effects are included in the calculations, the peaks in the intensity spectrum appears smeared out as shown in figure 2.9b.

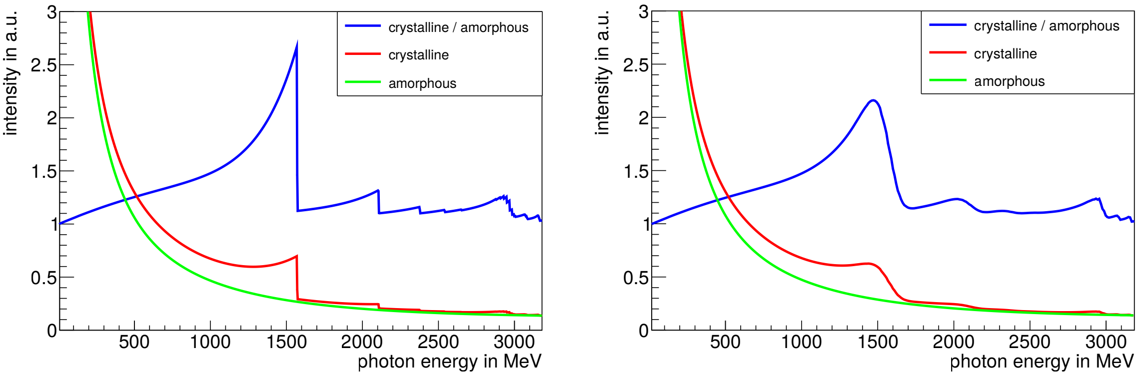

(a) Calculations for the ideal case. Primary electron beam divergence and multiple scattering in the radiator were not considered.

(b) Primary electron beam divergence and multiple scattering in the radiator are approximated with Gaussian distributions. Discontinuities are smeared out.

Figure 2.9: Amorphous and crystalline bremsstrahlung spectra. The blue curve shows the ratio of the crystalline to the amorphous bremsstrahlung spectra. Visible, as peaks in the crystalline and relative bremsstrahlung spectra, are the various coherent contributions originating from different reciprocal lattice vectors.

2.2.5 Determination of the Degree of Polarisation

By considering the coherent and incoherent contribution, the degree of polarisation can be written [17] as

$$P = \frac{k}{\sigma_0} \cdot \frac{d\sigma^{\parallel} - d\sigma^{\perp}}{d\sigma^{\parallel} + d\sigma^{\perp} + \sigma_{inc}} = 2(1-x)\frac{\Psi_3^c}{I_{inc}} \tag{2.41}$$

with

$$\Psi_3^c = -\frac{1}{2}\frac{(2\pi)^2}{a^3}\delta^3 \sum_{\vec{g}} |S(\vec{g})|^2 e^{-Ag^2} \frac{(1-F(g^2))^2}{g^4} \frac{q_t^2 \cos 2\phi}{q_l^4}. \tag{2.42}$$

Here ϕ denotes the angle between the reference plane and the $(\vec{p}_0, \vec{q})$ plane. Theoretically, the maximum degree of polarisation is obtained for disappearance of the incoherent contribution and if only one lattice vector contributes to the coherent intensity distribution. The degree of polarisation at the discontinuity can be described by

$$P(x_d)_{ideal} = \frac{2(1-x_d)}{(1+(1-x_d)^2)}. \tag{2.43}$$

For photon energies x much smaller than the discontinuity x_d, the degree of polarisation is given by

$$P(x, x_d)_{ideal} = \frac{2x^2Q^2}{1-x}\left(1 + (1-x)^2 - \frac{4x^2Q^2}{1-x}\left(\frac{1-x}{xQ} - 1\right)\right)^{-1}, \quad Q = \frac{1-x_d}{x_d} \tag{2.44}$$

which is shown in figure 2.10. For $x_d \rightarrow 0$ the enveloping curve increases asymptotically until full polarisation of the bremsstrahlung photons is achieved, while for $x_d \rightarrow 1$ the degree of polarisation drops to zero. Generally, the maximum degree of polarisation of the photon beam at the discontinuity cannot be accomplished, because several reciprocal lattice vectors will lie in the *pancake*, which contribute destructively to the degree of polarisation. In addition, the contribution of the incoherent spectrum decreases the degree of polarisation.

$$P(x, x_d)_{real} = \frac{P(x, x_d)_{ideal}}{1 + \frac{I^{inc}}{I^c}}, \quad x \leq x_d. \tag{2.45}$$

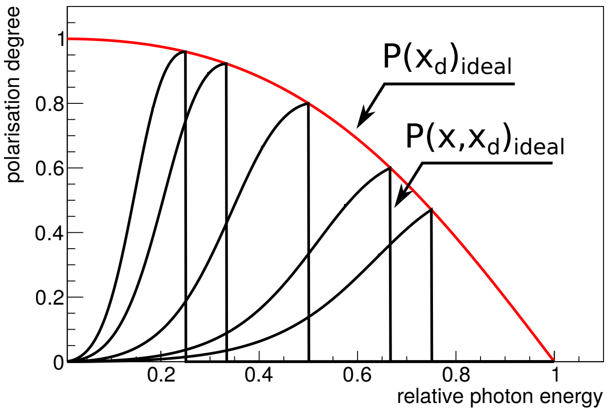

Figure 2.10: P(x,x_d)$_{ideal}$ (eq. 2.44) describes the degree of polarisation for five different crystal orientations of one reciprocal lattice vector in dependence of the photon energy. P(x_d)$_{ideal}$ (eq. 2.43) indicates the maximum degree of polarisation in dependence of the photon energy in red.

2.2.6 Collimation

According to equation 2.45 it is possible to increase the degree of polarisation by reducing the incoherent intensity contribution. Because the angular distribution of incoherent bremsstrahlung (eq. 2.48) is much broader than for coherent (eq. 2.46), a collimator reduces the incoherent contribution more effectively and an increase in the degree of polarisation can be achieved. Due to the different angular distributions of the coherent and the incoherent part, collimation in the calculations has to be treated separately for each intensity contribution. Photons produced in the coherent bremsstrahlung process are emitted in extreme forward directions. The angular distribution for the coherent intensity distribution, according to [17], is given by

$$u_k^2 = \frac{1-x}{x} \cdot \frac{x_d}{1-x_d} - 1. \tag{2.46}$$

Equation 2.46 shows, that the photon opening angle increases with decreasing photon energy. A collimator placed in the beam axis, defines an upper limit for the photon opening angle $u_c = \theta_c E_0$. The corresponding minimum photon energy is given by

$$x_c = \frac{x_d}{1 + u_c^2(1 + x_d)}. \tag{2.47}$$

In this case for coherent bremsstrahlung an upper sharp limit in the *pancake* area, due to the collimator, can be realised.

According to [27], the angular distribution of the incoherent intensity spectrum is given as

$$d^3\sigma^{incoh} \approx d\sigma^{incoh} \frac{u_k du_k d\omega}{(1+u_k^2)^2} \quad \text{with} \quad u_k = \theta_k E_0. \tag{2.48}$$

Here θ_k describes the photon opening angle, ω the azimuthal emission angle and E_0 the primary electron energy. To describe the collimation in the incoherent part, the intensity contribution has to be multiplied by a reduction factor. The reduction factor (see [17]) which is given by equation 2.49 is determined by the ratio of the collimated and the uncollimated intensity distribution.

$$f_c = \frac{\int\limits_0^{u_c} d^3\sigma^{incoh}}{\int\limits_0^{\infty} d^3\sigma^{incoh}} = \frac{u_c^2}{1+u_c^2}. \tag{2.49}$$

CHAPTER 3

BGO-OD Experiment

In this chapter the **El**ectron **S**tretcher **A**ccelerator at the University of Bonn and the components required for the production of a real photon beam of known energy via the process of bremsstrahlung are introduced. The second part describes the target and the detector components of the BGO-OD experiment used for the detection of final state particles of photon induced hadronic reactions. The trigger conditions for data taking are presented at the end.

3.1 Production of real photon beams and beam detectors

3.1.1 ELSA

The **El**ectron **S**tretcher **A**ccelerator ELSA consists of three stages. In figure 3.1 the full setup of ELSA is shown. Two electron sources each followed by a LINAC[1] make up the first stage. At LINAC 1 unpolarised electrons are produced by a thermal source with an energy of 120 keV and subsequently accelerated to an energy of 20 MeV. Longitudinally polarised electrons with an energy of 50 keV can

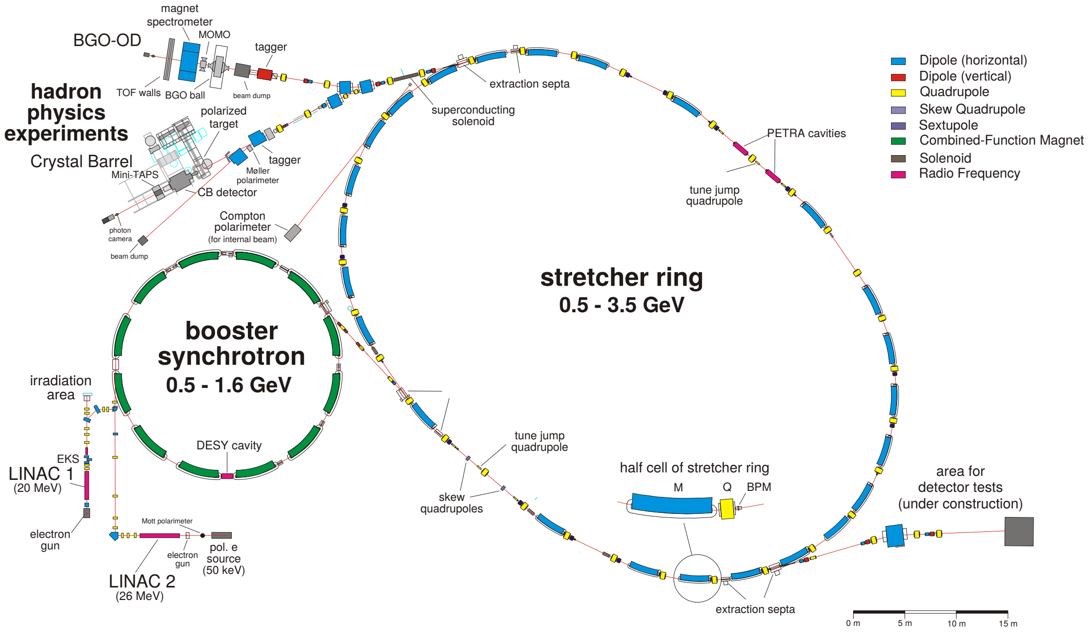

Figure 3.1: The electron stretcher accelerator.

---

[1] **Lin**ear **Ac**celerator

be provided at LINAC 2 by using the process of photoionisation, impinging circularly polarised laser light on a Be-InGaAs/Be-AlGaAs super lattice crystal. The electrons are accelerated in LINAC 2 to an energy of 26 MeV.

After the acceleration in one of the LINACs, the electrons are injected into the booster synchrotron being the second stage in the ELSA setup. It is used as a preaccelerator for the last stage being the electron stretcher accelerator giving the name to the facility. The booster synchrotron is operating with a frequency of 50 Hz accelerating the electrons to energies between 0.5 GeV and 1.6 GeV. With an energy of typically 1.2 GeV the electrons are injected into the electron stretcher. Since the stretcher ring has a larger circumference, the injection from the booster synchrotron is repeated until the stretcher ring is homogeneously filled.

ELSA is used to convert the short electron pulses of the booster synchrotron into a quasi continuous electron beam with energies up to 3.5 GeV. In dependence of the requirements on the stretcher ring, one of the three following operation modes can be chosen.

1. **Acceleration mode:** after the stretcher ring is homogeneously filled, the injected electrons are further accelerated. The maximum reachable energy amounts 3.5 GeV. The extraction of the electrons called *spill* is protracted quasi continuously[2] over typically 4 s until the stretcher ring is emptied. Within ~1.5 s, the electron stretcher is refilled over several injection cycles by the booster synchrotron. Thus, a high duty cycle of about >70% is reached.

2. **Stretcher mode:** this mode is identically to the first one without further acceleration. This means, that the energy of the electron beam is given by the energy with which the electrons are injected from the synchrotron into the stretcher ring.

3. **Storing mode:** for former synchrotron light experiments, after being accelerated, the electrons were stored for several hours depending on the energy.

The acceleration mode is used for photo-production experiments at the BGO-OD setup.

3.1.2 Tagging principle

The production of real photons via the process of bremsstrahlung was explained in chapter 2 and is commonly used already in various experiments including the BGO-OD experiment. The bremsstrahlung spectrum is continuous. Energy and time information of a produced bremsstrahlung photon are a priori unknown. A detector setup called photon tagger allows to assign the correct energy and the production time to these photons. If a tagged bremsstrahlung photon induces a hadronic reaction, it is possible to relate this photon to its corresponding reaction.

The working principle of the photon tagger is illustrated in figure 3.2. The primary electron beam provided by ELSA with a given energy E_0 impinges on a thin bremsstrahlung target, the radiator. Generally a thin metal foil or a crystal is used (see chapter 2). An electron which is involved in the bremsstrahlung process emits a real photon with a certain energy E_γ due to the deceleration within the radiator, mostly in the Coulomb field of the nuclei. Due to the high mass of the nucleus, the energy transfer to the recoil nucleus is negligible. Hence, by knowing the energy of the post bremsstrahlung electron, the energy of the produced bremsstrahlung photon can be determined via

$$E_\gamma = E_0 - E_{e^-}. \tag{3.1}$$

---

[2] The electron beam is extracted bunch-wise with a periodicity of 2 ns. The width of each bunch depends on the energy and amounts to ~120 ps in the worst case.

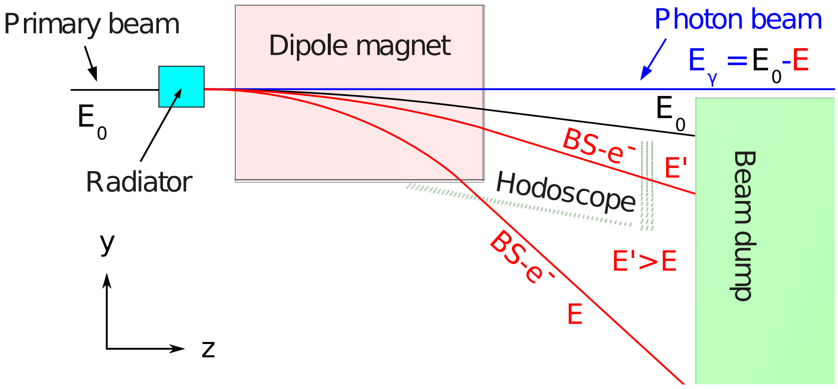

Figure 3.2: Components and working principle of the photon tagger at the BGO-OD experiment.

To determine E_{e^-}, the post-bremsstrahlung electron is momentum analysed by a magnetic spectrometer consisting of a dipole magnet and a detector hodoscope. According to its momentum and to the integrated magnetic field strength $\int B \cdot dl$, the post-bremsstrahlung electron is bend by the dipole magnet into the hodoscope. From the detection position in the hodoscope the energy E_{e^-} of the post-bremsstrahlung electron and therefore the energy of the produced bremsstrahlung photon can be determined. The electrons which are not involved in the bremsstrahlung process are bend into a beam dump.

3.1.3 Tagger system components

Most of the components of the photon tagger system of the BGO-OD experiment are illustrated in figure 3.3 which shows a technical scheme of the full setup. In this section, the single components are introduced.

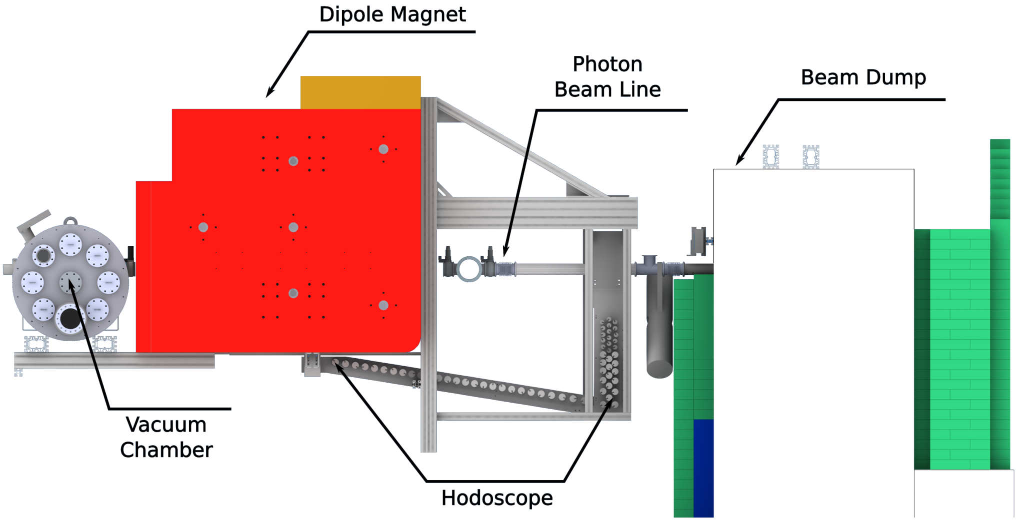

Figure 3.3: Technical scheme of the photon tagger system. Main components are the vacuum chamber including the bremsstrahlung radiators and beam monitoring tools, the dipole magnet and the detector hodoscope. The hodoscope is connected with R+K^{3}profiles to the dipole magnet. Visible at the end is the electron beam dump.

Radiators and beam monitoring Several bremsstrahlung radiators and tools for beam monitoring purposes are mounted on a goniometer system which will be introduced later. It is installed within a vacuum chamber and placed in front of the dipole magnet (see figure 3.3). A list of the installed radiators and beam monitoring tools is given in table 3.1. In total, four different amorphous radiators of different thickness and materials and one crystalline radiator are installed. Amorphous radiators are used to measure incoherent bremsstrahlung spectra to normalise the measured bremsstrahlung spectra of a diamond. The normalised diamond spectra are used to compute the degree of linear polarisation (see section 5.2). To determine the shape and the position of the beam profile, a fluoresce screen made of $Al_2O_3 : Cr$ also known as Chromox is used. It can be placed with an angle of 45° relatively to the reference electron beam direction, which allows to observe the fluorescent spot with a camera perpendicular to the electron beam direction. For a more precise analysis of the beam profile, two nickel-steel wires are included in the goniometer system. These wires can be moved orthogonally with respect to the reference electron beam direction along the horizontal or vertical axis. While moving the wires stepwise through the beam, the post-bremsstrahlung electrons are detected by the tagging hodoscope. Hence, an iterative scan of the beam profile is possible by plotting the total tagging rate in dependence of the position of the wire (see figure 3.4).

Material	Thickness in μm
Copper	50
Copper	100
Kapton	125
Copper + Kapton	67 + 65
Diamond + Kapton	560 + 65
Nickel-Steel wires	400
Chromox	1000

Table 3.1: Radiators and beam monitoring tools used for the BGO-OD experiment.

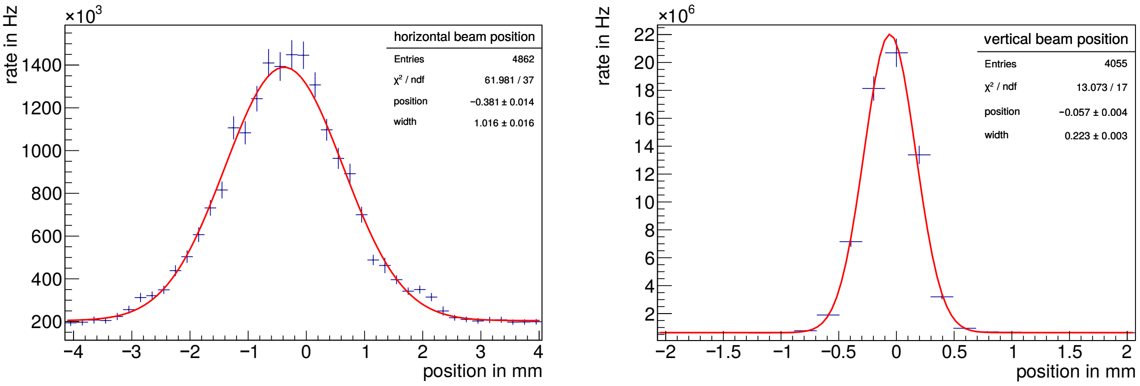

(a) Horizontal beam scan.

(b) Vertical beam scan.

Figure 3.4: Measured primary electron beam profile and position performed with two wire scans. Errors originate from statistics. Each distribution is fitted with a Gaussian function.

---

[3] Rose und Krieger

Goniometer The goniometer system is used to choose between different radiators and beam monitoring tools. However, the main task of the goniometer system is the precise alignment of the diamond radiator. From chapter 2.2 it is known, that the energetic range for the production of linearly polarised photons and subsequently the degree of polarisation of the produced photon beam is sensitive to the relative position of the diamond with respect to the direction of the primary electron beam. Therefore, a goniometer system with a proper accuracy in positioning and reproducibility is required. The commercial goniometer system from NEWPORT[4] consists of five motorised positioning units. This setup allows translations horizontally and vertically relative to the reference electron beam direction and rotations along all three spatial axis. The important specifications of the individual motorised units are listed in table 3.2 and 3.3. For the precise alignment of the diamond radiator, a holding structure was developed [28] which keeps the diamond radiator in the intersection point of the three rotational units. The goniometer system was extended in January 2014 for the determination of the degree of polarisation of circularly polarised photons. These modifications required a new vacuum chamber. The motorised unit responsible for horizontal translations with respect to the reference electron beam direction was enlarged to install a second rotational stage beside the existing goniometer system. This rotational stage is used for the orientation of a solenoid including a Møller radiator [29]. The current setup of the goniometer system is illustrated in figure 3.5.

	MTM250PE1B	UZS80PP
travel range	250 mm	4.5 mm
resolution	1 μm	0.01 μm
uni directional rep.	1.5 μm	1.4 μm

Table 3.2: Specifications of the motorised translation units.

	URS100BPP	BGS80PP	RVS80PP
travel range	360°	±45°	360°
resolution	0.0002°	0.0001°	0.0001°
uni directional rep.	0.016°	0.001°	0.002°

Table 3.3: Specifications of the motorised rotational units.

Dipole Magnet The dipole magnet is used to bend the post-bremsstrahlung electrons according to their momentum on different trajectories into the hodoscope. Electrons which are not involved in the bremsstrahlung process are bend into the beam dump. The magnet used by the BGO-OD experiment is identical to the one used in the neighbouring Crystal Barrel experiment [30]. It is a dipole magnet from Brown-Bovery Switzerland (type MC) which can be operated with currents up to 1500 A, corresponding to a maximum field value of B = 2.0 T. The deflection angle of the primary electron beam is defined by the geometry of the electron beam dump and amounts to 7.74°. For high relativistic electrons, the deflection depends only on the ratio B_0/E_0. A deflection angle of 7.74° is reached for $B_0/E_0 = 0.43$ T/GeV. Since primary electron beam energies up to 3.2 GeV are used, magnetic field values up to 1.376 T are necessary. Figure 3.6b shows that the deviation from a linear behaviour of the magnetic field value with respect to the applied current is less than 1% at a magnetic field value of 1.5 T. Field maps of the dipole magnet of the Crystal Barrel experiment have been established for five different primary electron beam

---

[4] www.newport.com

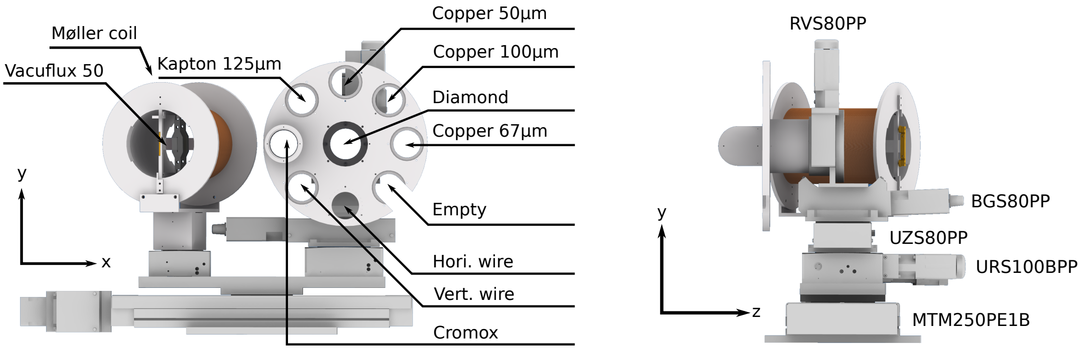

Figure 3.5: Technical scheme showing front and side view of the goniometer and Møller system containing the bremsstrahlung radiators.

energies [30]. These field maps were used in simulations for the development of the BGO-OD photon tagging system. Since the BGO-OD tagging magnet operates with a lower magnetic field for the same primary electron beam energies, the field maps have to be scaled down. This is possible for field maps with primary electron beam energies of up to E_0 = 2400 MeV, where the linearity of the Crystal Barrel dipole magnet is still fulfilled.

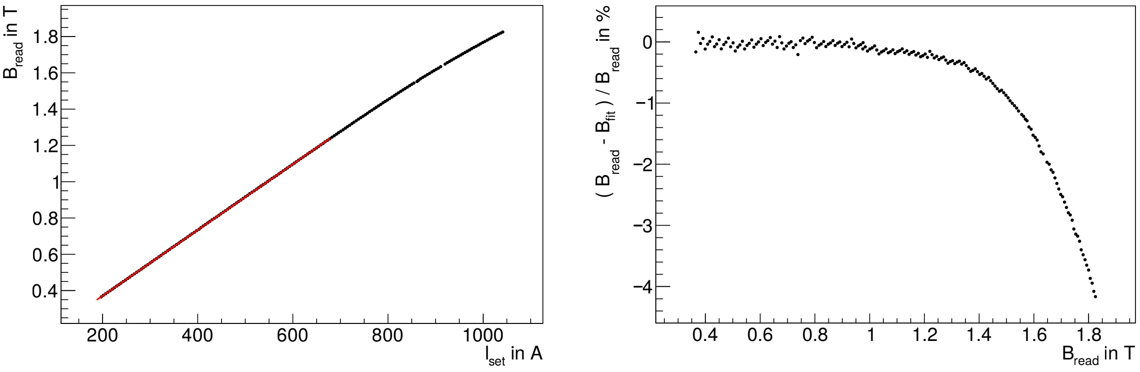

(a) Measured magnetic field vs applied current. The black dots are the measured field values. The red line reflects a linear correlation between the applied current and the measured magnetic field.

(b) Difference between the measured and the expected magnetic field value depending linearly on the applied current versus the measured magnetic field values as a function of the measured field.

Figure 3.6: Dependence of magnetic field value to applied current.

Hodoscope The hodoscope of the tagging system consists of 120 plastic scintillators covering an energy range of 10%E_0 to 90%E_0. It is split into two parts. 54 scintillators are inserted into the horizontal part and the remaining 66 scintillators are installed in the vertical part. Two adjacent scintillators overlap by ~55%. Such overlaps are considered as a coincidence channel providing the momentum of the detected post bremsstrahlung electron. Requiring the coincidence of two neighbouring scintillators as a trigger condition reduces the background. The energy width of a coincidence channel varies from 0.55%E_0 in the horizontal part to 0.80%E_0 - 2.12%E_0 in the vertical part (see 4.4.4). The scintillator bars of the hodoscope are read out via photomultipliers from one side. For geometrical reasons (see 4.3.4), two different kind of photomultipliers are used, namely ETEnterprise 9111 and Hamamatsu R7400U. A time resolution of ~210 ps for the ET9111SB and of ~180 ps for the Hamamatsu R7400U is achieved (see 4.4.1). The following table shows some of the specifications of the scintillating material and the photomultipliers.

	R7400U	9111SB		EJ-204
spectral response:			emmission spectrum:	
range in nm	300-650	280-630	range in nm	<380-500
peak in nm	420	350	λ of max. emission in nm	408
time:			time:	
rise time in ns	0.78	1.8	rise time in ns	0.7
transit time in ns	5.4	15	decay time in ns	1.8

Table 3.4: Specifications of photomultipliers and scintillating material used for the photon tagger system

Construction, installation and commissioning of the tagging hodoscope are the main topics of this PhD thesis. A detailed description of the tagging hodoscope and of its performances is given in the dedicated chapter 4.

Collimator and cleaning magnet At a distance of 3.25 m to the radiator a system of two collimators and one permanent magnet is installed. The collimators are made of lead and are both 20 cm long. The first collimator has a diameter of 3 mm. Its purpose is to reduce the incoherent contribution in the bremsstrahlung spectrum using a diamond radiator for the production of a linearly polarised photon beam resulting in an enhancement in the degree of polarisation (see chapter 2). Due to the collimation of the photon beam, electron-positron pairs are produced. Hence, a permanent magnet is placed directly after the first collimator to clean the photon beam from charged particles. The second collimator with a diameter of 7 mm is placed after the cleaning magnet to stop high energetic charged particles which could not be removed from the vacuum beam guidance by the cleaning magnet.

3.1.4 FluMo and GIM

The **Flu**x **Mo**nitor and the **G**amma **I**ntensity **M**onitor [31] are placed at the end of the BGO-OD experiment. These detectors allow the measurement of the photon flux, which is required to perform normalisations e.g. for cross section determinations. The GIM is a fully absorbing lead glass detector. An incoming photon will produce an electromagnetic shower which is detected by its produced Črenkov light. However, the GIM suffers radiation damage and therefore it can not be kept continuously in the photon beam and therefore the photon flux is measured with the FluMo.

The FluMo is a detector setup consisting of a plastic scintillator used as a veto and two additional plastic scintillators. This setup detects photons which did convert into electron-positron pairs behind the veto detector. It measures only a fraction of the bremsstrahlung photons with respect to the GIM. Photon Flux measurements with the FluMo require the knowledge of its detection efficiency. It is determined with data taken by triggering on the GIM detector. Coincidences between the tagger system and the GIM are identified on software level. For each coincidence, it is verified if the FluMo did detect in both channels an electron-positron pair originating from a bremsstrahlung photon. The discriminator thresholds have to be set in order to assure the detection of both minimal ionising particles (MIP). Figure

3.7 shows the ADC[5] spectra of both FluMo channels plotted against each other. The two peaks, which are well separated, correspond to single and double MIP detection. The single MIP peak can be cut by properly setting the discriminator thresholds.

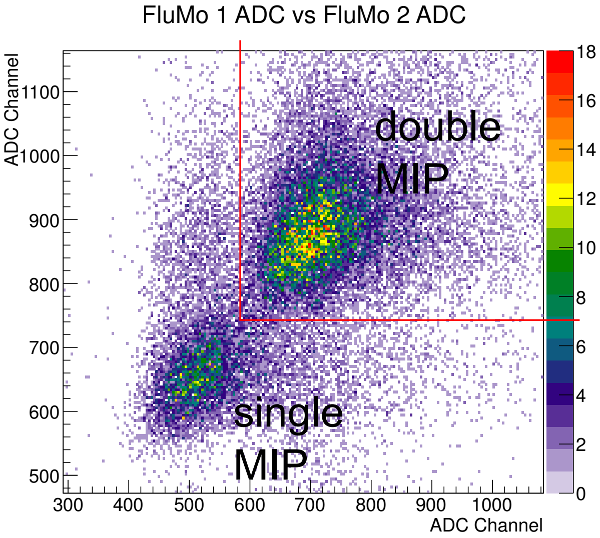

Figure 3.7: Raw ADC spectra of both FluMo detectors plotted against each other [31]. The double MIP peak is well separated from the single MIP peak.

Beside the photon flux measurement, collimated bremsstrahlung spectra can be obtained by requiring a coincidence between the FluMo and the tagger hodoscope. If a produced bremsstrahlung photon passes the collimator and does not induce a hadronic reaction in the central detector setup, it may be detected by the FluMo.

3.2 Experimental Setup

The BGO-OD experiment is a fixed target experiment for the study of meson photo-production reactions off the nucleon. Its main goal is the simultaneous investigation of excited baryon resonances and t-channel processes. Figure 3.8 shows the full setup including the photon tagger. The name of the experiment comes from the central BGO[6] calorimeter enclosing the target cryostat and the magnetic spectrometer at forward angles including an **o**pen **d**ipole magnet. This setup is optimised for the detection of mixed charged and neutral final states and well suited for the investigation of low momentum transfer processes.

After collimation, the produced bremsstrahlung photon beam impinges on a liquid hydrogen or deuterium target. The target cell has a length of 6 cm and a diameter of 3 cm. Front and back of the target cell are closed with Myler foil [32].

The central detection system, shown in figure 3.9a, surrounds the target and consists of two MWPC's[7], a plastic scintillator barrel and the BGO electromagnetic calorimeter.

The MWPC used for charged particle tracking consists of two chambers. Figure 3.9b shows the schematic overview of one of them. Each chamber includes anode wires running parallel to the beam

---

[5] Analogue to digital converter

[6] **B**ismuth **G**ermanate **O**xide

[7] **M**ultiple **W**ire **P**roportional **C**hamber

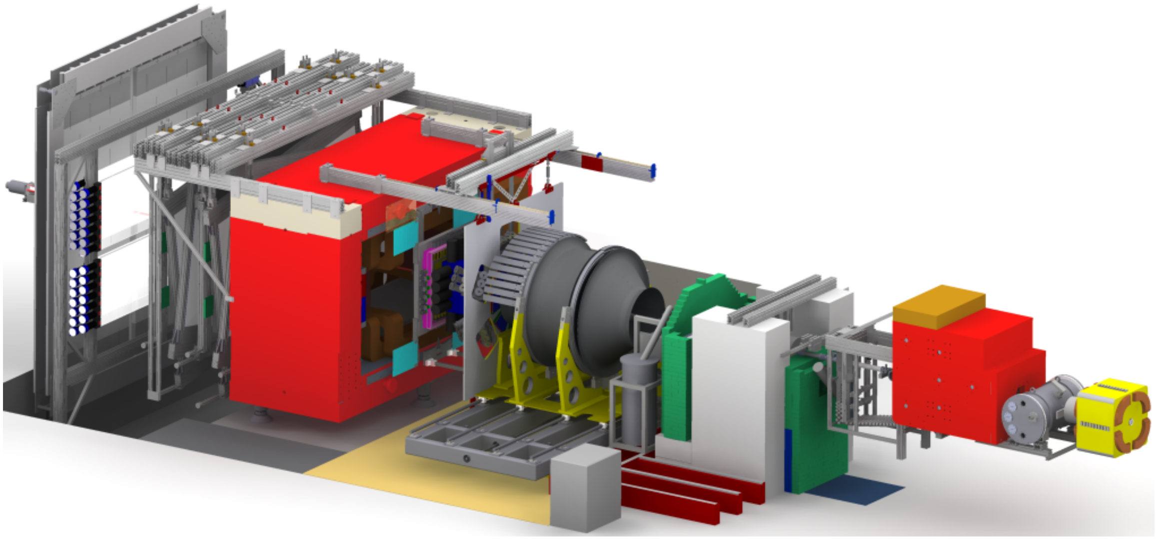

Figure 3.8: Setup of the BGO-OD experiment.

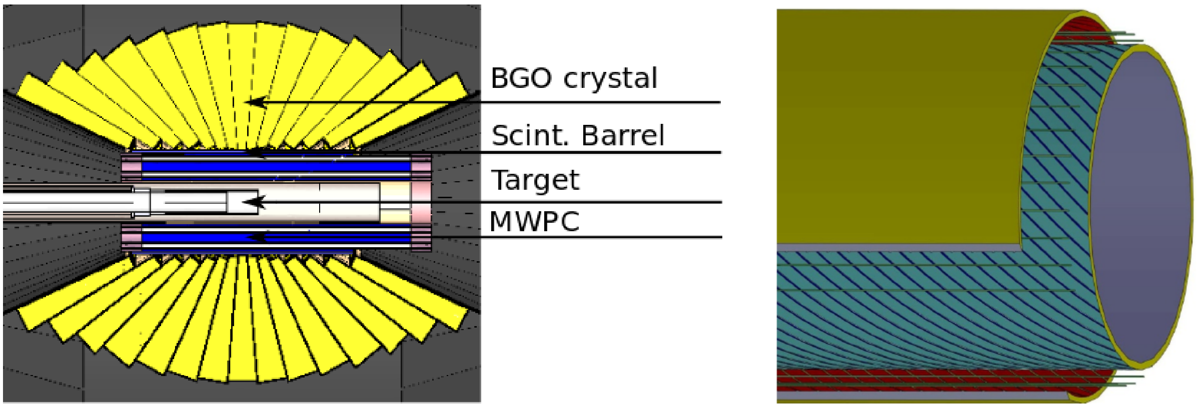

(a) Slice view in xy-plane of the central detector setup.

(b) Schematic overview of one MWPC chamber.

Figure 3.9: Central detector setup.

axis and, inner and outer cathode strips tilted by ±45° with respect to the wires. Over a length of 520 mm, inner and outer strips intersect twice in two different points given by z and ϕ. The intersection of the strips with the corresponding wire allows an unambiguous reconstruction of the particle's impact point. Absolute tracks can be reconstructed by combining the information of both chambers. An angular resolution of $\Delta\phi = 2°$ and $\Delta\theta = 1°$ and longitudinal resolution of $\Delta z = 300\,\mu$m is expected [33].

The scintillator barrel, placed between the MWPC and the BGO calorimeter consists of 32 bars. Each strip has a thickness of 5 mm and a length of 43 cm. Particle identification is performed with the scintillator barrel via the measurement of the energy loss dE/dx [34].

The BGO calorimeter covers a polar angular range of 25° to 155° with 15 crowns. Each crown consists of 32 crystals and covers the full azimuthal angle ϕ. Each crystal has a length of 24 cm, which corresponds to 21 radiation lengths. As a results, photons deposit nearby all their energy in an electro magnetic shower which spreads over several adjacent crystals. It has an energy resolution of 3% at 1 GeV. The performances of the detector have been already exploited by the GRAAL collaboration

([35],[36],[37],[38],), where the detector has been used up to 2008.

The magnetic spectrometer covering the most forward angles consists of two scintillating fibre detectors, the open dipole magnet and eight driftchambers. The magnetic spectrometer covers an angular range of 8° in vertical and 10° in horizontal direction. In the following the single components are presented.

The first detector in the spectrometer setup is a scintillating fibre vertex detector and placed 113 cm behind the target. It consists of 672 fibres distributed in six modules positioned in three layers. The modules are rotated by 60° to each other, resulting in an sensitive circular area with a diameter of 44 cm. A 4.5 cm central hole in the detector allows the photon beam to pass through [39].

Attached to the dipole magnet is the second scintillating fibre detector. It has a rectangular shape of 66 cm x 51 cm. 640 fibres are arranged in two layers, 288 fibres horizontally and 352 vertically. A central hole of 4 cm x 4 cm allows the photon beam to pass through [40].

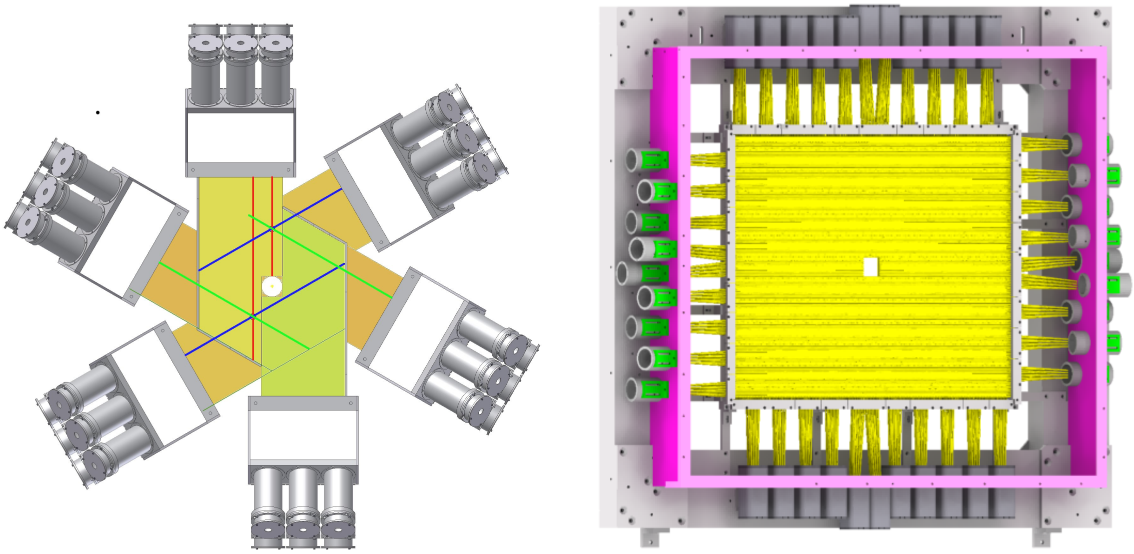

(a) Technical scheme of the scintillating fibre vertex detector.

(b) Technical scheme of double scintillating fibre detector.

Figure 3.10: Forward scintillating fibre detectors used for particle tracking.

The open dipole magnet is a MD type on permanent loan basis from DESY[8]. For the BGO-OD experiment the vertical opening was increased and the total gap amounts to 150 cm x 84 cm. With the maximum current I_{max} = 1340 A given by the power supply, a maximum central magnetic field strength of B_{max} = 0.54 T and a bending power of $\int B dl \approx 0.74$ Tm is expected from simulations [41].

Charged particle tracking behind the open dipole magnet is performed by eight double layer drift chambers with sensitive area of 246 cm x 123 cm. For unambiguous track reconstruction, the dift chambers are installed in four different orientations in the xy-plane. Two chambers are installed vertically and horizontally, while the remaining four chambers are tilted by ±9° with respect to the vertical axis. A central insensitive area of 5 cm x 5 cm is realised by additional gold plating of 200μm which allows the photon beam to pass through [42].

For particle identification in forward direction, two time of flight walls are placed behind the magnetic spectrometer setup, 5 m far from the target. One detector wall consists of 10 x 340 cm x 21 cm x 6 cm

---

[8] **De**utsches **E**lektronen **S**ynchrotron

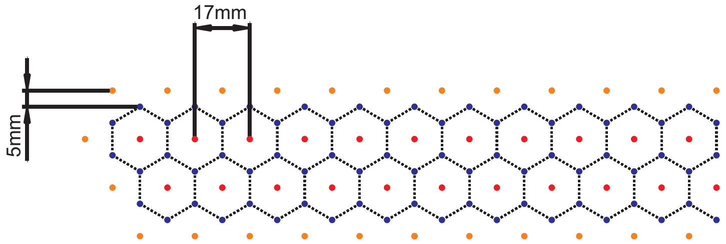

Figure 3.11: Cell arrangement in the drift chambers.

plastic scintillators bars, the other contains 14 x 270 cm x 20 cm x 4.5 cm plastic scintillator bars. Each bar is read out by photomultipliers at both ends, which allows to correct for the light propagation [43].

Between the central detector system and the forward spectrometer exists an uncovered angular area from 8° to 25°. This area is going to be covered by a MRPC[9] called Daisy. It consists of 16 modules with in total 512 channels delivers an expected spatial resolution of 1 cm^2. A high time resolution of 80 ps is estimated[44]. While Daisy is under commissioning, the angular range is covered by a plastic scintillator ring detector called SciRi. It is segmented in 96 pieces, each covering $\Delta\phi = 11.25°$ and $\Delta\theta = 5°$. The plastic scintillators are read out with avalanche photodiodes. The full detector setup is placed inside the carbon structure of the BGO calorimeter [45].

3.3 Trigger conditions

Background suppression and time saving during data taking can be achieved by setting conditions under which reactions of interest are stored. At the BGO-OD experiment the trigger logic is composed of two parts [46], [47]. During data taking, local trigger signals are generated for almost each detector. Such conditions, like deposited particle energy or defined hit patterns depend on the function of the installed detectors. Table 3.5 shows an overview of the detectors which are able to give trigger signals and their trigger conditions during nominal data taking. However, for some detectors it is possible to adapt the trigger condition for special applications or testing purposes.

Detector	Trigger condition
Tagger	AND of two adjacent channels
Scint. barrel	OR of all single channels
BGO	Sum of deposited energy of all crystals
SciRi	OR of all single channels
SciFi2	OR of all single channels
TOF	OR of all single channels
	Mean time of bar signals
FluMo	Detector hit in one specific channel
GIM	Detector hit

Table 3.5: Detectors and trigger conditions.

In the second step, the local trigger signals are given to the global trigger logic which is programmed

---

[9] **M**ultigap **R**esistive **P**late **C**hamber

on an FPGA[10] board. At this stage several combinations of logical ANDs and ORs on any subset of local trigger signals can be build. Local trigger signals may be used as VETO signals as well. The output of such logics is ORed and if required prescaled to generate the final trigger condition. The standard trigger condition for data taking is

- **General_ physics_ trigger:**

$$\begin{aligned} & (Tagger \ \wedge \ BGO) \\ \vee \ & (Tagger \ \wedge \ BGO \wedge SciRi) \\ \vee \ & (Tagger \ \wedge \ BGO \wedge SciFi \wedge TOF) \\ \vee \ & (Tagger \ \wedge \ SciRi \wedge SciFi \wedge TOF) \end{aligned}$$

Runs dedicated to the normalisation of the diamond bremsstrahlung spectra are acquired with the trigger condition

- **FluMo:**

$$FluMo \ x \ scalingfactor$$

The temporal coincidence between tagger and FluMo is required on software level. The scaling factor in the FluMo trigger is adjusted according to the primary electron beam intensity.

---

[10] **F**ield **P**rogrammable **G**ate **A**rray

CHAPTER 4

Photon Tagger

The main part of this PhD thesis is the design, assembly and commissioning of the tagger hodoscope of the BGO-OD experiment. In this chapter are presented first the requirements on the tagging system and the electronics used for the read out of the detector setup. Secondly, the various steps in the computation of the final scintillator arrangement and the resulting expected energy resolution of the tagger hodoscope based on the detector concept developed in [48] are shown. The design of the mechanical frame of the tagger hodoscope is deduced from the scintillator arrangement. Schematics of the main parts of the mechanical structure will be presented. At the end, the results of the commissioning consisting of the characterisation and the energy calibration of the tagger hodoscope will be shown.

4.1 Requirements

The design of the photon tagger system is defined by several aspects, for example by the spatial conditions given in the experimental hall or by demands of the experiments being performed with the BGO-OD setup. Hence, compromises had to be taken between desired requests on the detector and geometrical or technical constraints. The design goals on the photon tagger system are:

(i) A post-bremsstrahlung electron tagged energy range from 10% to 90% of the primary electron beam energy E_0. This energy range is limited by the geometry of the dipole magnet for energies lower than $10\%E_0$. For energies larger than $44\%E_0$ the focal plane (see section 4.3.1) of the dipole magnet lies within the beam dump. Hence, the tagger hodoscope had to be split into a horizontal and a vertical part. Since the bremsstrahlung cross section is $\propto 1/E_\gamma$, scintillators and photomultipliers are possibly subject to radiation damages on a short time scale for energies higher than $90\%E_0$.

(ii) The energy E_{e^-} of the detected post-bremsstrahlung electron is given by the overlap of two neighbouring scintillator bars. Two adjacent scintillators are considered as a coincidence channel and overlap by ~55%. The energy width ΔE of a coincidence channel depends on the geometrical width of the scintillators and their positioning in the hodoscope. By keeping ΔE constant and arranging the coincidence channels in energy bins of ΔE, a linear dependency between coincidence channel and post-bremsstrahlung electron energy over the full tagged energy range is achieved. This allows a simple determination of the energy of the produced bremsstrahlung photons. Since the bend trajectories are getting closer for higher post-bremsstrahlung electron energies, the scintillators have to be made thinner to keep ΔE constant. The manufacturing of arbitrarily small scintillators is not possible and would additionally make the design of the hodoscope unnecessarily complicated. Consequently, the hodoscope is sub-divided in five sections with different energy bin sizes (see section 4.3.2).

(iii) Requiring the coincidence of two adjacent scintillators reduces the detection of particles which do not originate from expected post-bremsstrahlung electron trajectories, like scattered particles from the floor or the beam dump. To additionally reduce the neutron detection efficiency the thickness of the scintillators amounts 5 mm which reduces the probability of the neutron being detected in two overlapping scintillators to $< 1\%$ [48].

(iv) Different components of the hodoscope like scintillators and photomultipliers undergo ageing processes and have to be exchanged by time. The replacement of those parts can affect the energy calibration of the tagging system. Hence, the mechanical structure was designed such, that changes in the energy calibration caused by maintenance work are negligible (see section 4.4.4).

(v) The BGO-OD collaboration covers a physics program including the investigation of photo-production experiments with low cross sections requiring high photon fluxes. Hence, the tagging system has to work in a stable condition at total rates of 50 MHz (see section 4.4.2).

4.2 Electronics

A schematic overview of the front-end electronics is shown in figure 4.1. It consists of an active splitter and amplifier stage, a dual-threshold discriminator and shaper stage, and an FPGA stage including the trigger logic and a TDC[1]. In addition, the FPGA allows time alignment of the signals coming from the several channels of the tagger hodoscope and delivers the scaler information for single and coincidence channels (see figure 4.2).

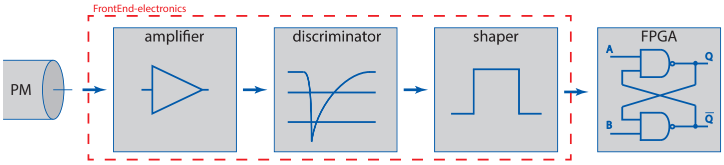

Figure 4.1: Read out electronics scheme for the tagger system.

Each analogue signal of the photomultipliers is sent to a splitter and amplifier board (AFA[2]) which is developed in-house [49]. Two outputs with different amplifications (x1, x2) relative to the input signal are available. The x2 amplified signal is send to the discriminator. If required, the x1 output is given to an ADC for HV[3] adjustments of the photomultipliers, otherwise it is terminated with a 50 Ω resistance. The measured time jitter between input and output is less than 15 ps.

The amplified signal is then sent to a dual- threshold discriminator and shaper board called B-FrED[4] which is also developed in-house [49]. Each board has 16 input channels and 16 LVDS[5] output channels. The output signals have a fixed length of 3.2 ps. Since originally TDC and trigger logics were separated, the B-FrED output has a fan-out of two. The double pulse resolution of the discriminator amounts 7.5 ns and the time jitter between input and output is less than 10 ps. Using a micro-controller, the thresholds of each channel can be set individually via Ethernet.

---

[1] **T**ime to **D**igital **C**onverter

[2] **A**nalogue **F**an-out **A**mplifier

[3] **H**igh **V**oltage

[4] **B**ig-**Fr**ont **E**nd **D**iscriminator

[5] **L**ow **V**oltage **D**ifferential **S**ignaling

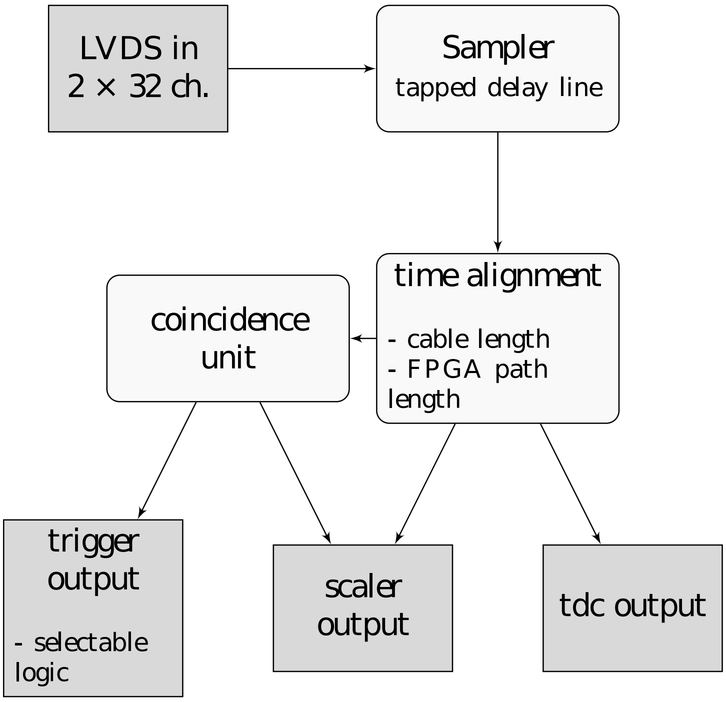

Figure 4.2: Flow chart of the tagger FPGA firmware.

One of the LVDS outputs of the B-FrED is sent to the FPGA board containing the TDC and trigger logic. It is an extensible ELB[6] VFB6 Module with VMEbus interface equipped with a Xilinx Spartan 6 chip. The module can be equipped with three mezzanine boards allowing flexible usage also for other detector systems in the BGO-OD setup. For the tagging system, the VFB6 module is equipped with a NIM_IO[7] mezzanine card, used for triggers and service purposes and two LVDS input mezzanine cards to connect the output of the B-FrEDs. The firmware is an in-house development for which detailed information can be found in [50]. For each input channel on the FPGA, the input signal is analysed in a carry chain using the tapped delay method. A time resolution of better than 40 ps is achieved using a clock of 200 MHz. Subsequently, a time alignment between all input channels can be performed with an accuracy of 5/6 ns allowing the compensation of the different path lengths of the post-bremsstrahlung electrons and additional minor effects like cable lengths and inner FPGA path lengths. If required, an additional logic unit checks for coincidences between two signals originating from adjacent tagger channels. The time window in which a coincidence between two signals is defined can be set to 1.7, 2.5, 3.3 or 4.1 ns. The output signal of this coincidence unit is given as the OR of all 119 coincidence channels and can be further used as a trigger. In addition to the trigger and TDC information, life-time gated scalers for single and coincidence channels are available.

4.3 Design

Based on the spatial restrictions and the requirements listed in 4.1, simulations were performed to determine geometry and position of the scintillator bars used in the tagging hodoscope to achieve the desired energy width per coincidence channel for the detector. The optimal layout of the scintillator

---

[6] http://www.elbonn.de

[7] **N**uclear **I**nstrument **M**odule, **I**nput **O**utput

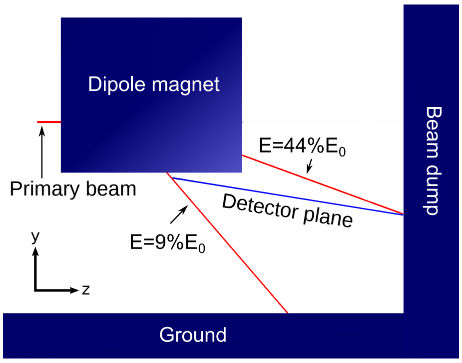

Figure 4.3: Simulated focal plane. The red lines indicate post-bremsstrahlung electron trajectories. The blue line shows the calculated focal plane of the dipole magnet.

bars was used to design a mechanical frame foreseen to keep the scintillator bars and photomultipliers in position and to allow simple maintenance on the full detector setup. In this section, the simulations and the mechanical design will be presented.

4.3.1 Simulation: Focal Plane

In a general approach, the optimal position of the hodoscope is defined by the focal points forming the focal plane, which depends on the imagine properties of the dipole magnet. The focal points are the positions in which the trajectories of bent electrons with same energy have their minimal spatial distribution and therefore offer the best energy resolution. Simulations are performed [48] to determine these focal points using the magnetic field map measurements mentioned in 3.1.3. In these simulations, electron trajectories through the magnetic field were calculated for uniformly distributed post-bremsstrahlung electron energies. The primary electron beam spot size and divergence as well as the expected divergence caused by multiple scattering in the radiator were considered in the simulation and described by Gaussian distributions.

In a second step, the focal points are extracted from the simulated post-bremsstrahlung electron trajectories. Figure 4.3 shows the resulting focal plane for bremsstrahlung electron energies from 9%E_0 to 44%E_0. For energies larger than 44%E_0, the focal plane collides with the beam dump. Hence, the tagging hodoscope is split in two separate parts. One part lies in the focal plane of the dipole magnet. It is called “horizontal part”. The second “vertical part” is mounted vertically close to the beam dump. The geometry and the arrangement of the scintillator bars in both parts of the tagging hodoscope is presented in the following section.

4.3.2 Simulation: Scintillator Positioning

The energy information E_{e^-} of the detected post-bremsstrahlung electron is given by the overlap of two neighbouring scintillator bars. Two Adjacent scintillators are considered as a coincidence channel. The geometry of the scintillator bars and their positioning define the energy width ΔE of the coincidence channels. It is desired to keep ΔE constant and arrange the coincidence channels in energy bins of ΔE to achieve a linear dependency between the coincidence channels and the post-bremsstrahlung electron energies over the full tagger hodoscope. A simple algorithm [48] performs this calculations within two steps. At first, the lower edge of each scintillator bar is matched to a fixed post-bremsstrahlung electron energy such, that the energy difference of the lower edges of two neighbouring scintillator bars remains constant (see figure 4.4). In a second step, the size of the scintillator bars are adjusted in order to keep a spatial overlap of ~55% of two neighbouring scintillators, keeping in mind that the trajectories of post-bremsstrahlung electrons are getting closer for higher post-bremsstrahlung electron energies along the dispersion direction. The algorithm is slightly modified for the positioning of the scintillator bars in the

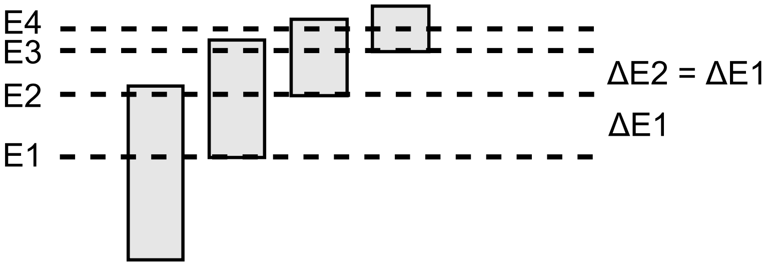

Figure 4.4: Adjusted positions of the scintillator bars resulting in constant energy width.

vertical part which does not lie within the focal plane. After placing the first scintillator in the vertical part, it is checked if the next scintillator can be placed directly above the first one. If not enough space is available, the following scintillator is placed behind the first one (see figure 4.5). This procedure is

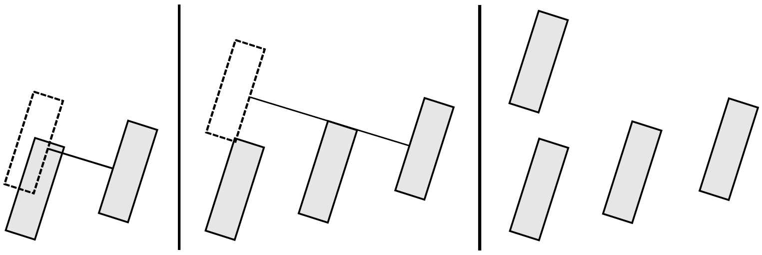

Figure 4.5: Staggering of the scintillator bars in the vertical part of the hodoscope.

repeated until the intended energy range is covered. By requiring an energy binning of 0.4%E_0 over the full tagged energy range, the scintillator arrangement shown in figure 4.6a is achieved. The vertical part would consist of 21 stacks with up to 6 scintillator bars per stack. This arrangement implies a complicated design of the mechanical frame of the detector. In addition, multiple scattering in the air or in the scintillator bars can cause ambiguous hit pattern, which would spoil the energy determination. In order to set the number of scintillator bars within one stack constantly equal to three, the geometrical width of the scintillators and consequentially the energy width ΔE of the coincidence channels has to be increased four times in the vertical part of the hodoscope (see figure 4.6b). The energy binning in the four regions of the vertical part of the tagger are 0.6%E_0, 0.8%E_0, 1.3%E_0 and 1.7%E_0. Figure 4.7 shows the scintillator arrangement for the full tagger hodoscope.

4.3.3 Simulation: Energy mean values and energy widths

To perform a cross check on the positioning of the scintillator bars, the scintillator layout is included into the simulation of the electron trajectories. The energy mean value and the energy width are determined for each coincidence channel. In this simulation the primary electron beam spot size and divergence as well as the expected divergence caused by multiple scattering in the radiator are described by Gaussian distributions. For each simulated event, the energy of the post-bremsstrahlung electron and the coincidence channel where the electron itself is detected are stored. Figure 4.8a shows the relation between the post-bremsstrahlung electron energies and the index of the coincidence channel of the tagger hodoscope. A magnetic field map for a primary electron beam energy of 2.4 GeV is used. It is visible that the post-bremsstrahlung electron energy increases linearly with increasing coincidence channel. Five

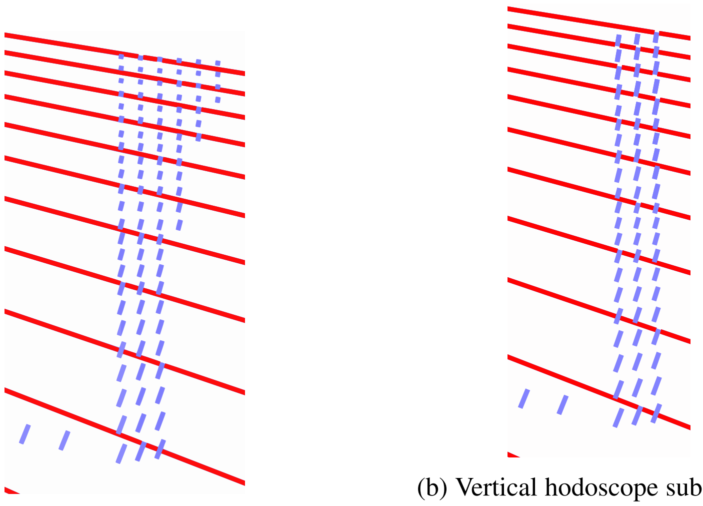

(a) Vertical hodoscope with constant energy bin size of 0.4%E_0.

(b) Vertical hodoscope subdivided in four regions with energy bin sizes of 0.6%E_0, 0.8%E_0, 1.3%E_0 and 1.7%E_0.

Figure 4.6: Calculated scintillator arrangement of the vertical tagger hodoscope. Red lines indicate post-bremsstrahlung electron trajectories in steps of 200 MeV.

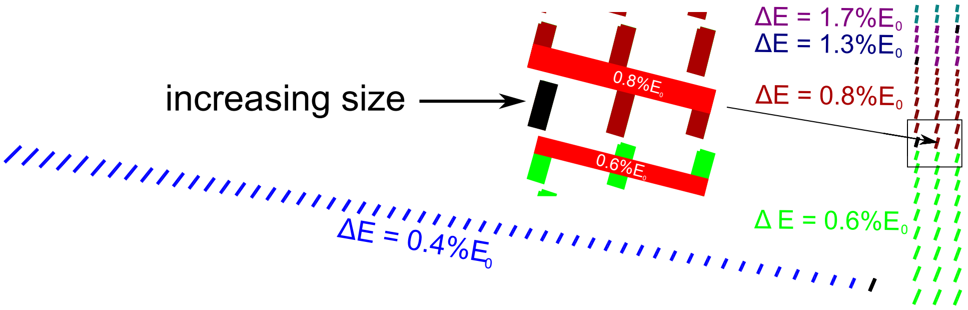

Figure 4.7: Full hodoscope with subdivided sections of different energy bin sizes. The black scintillators indicate the position in which the spatial width of the scintillators is enlarged.

regions of linearity are observed. The first region ranging from coincidence channel 1 to 53 corresponds to the horizontal part of the tagger (blue scintillators in figure 4.7). According to section 4.3.2, the energy binning changes four times in the vertical part of the hodoscope. This change results in an increased slope of the linear relation between the post-bremsstrahlung electron energies and the index of the coincidence channel. The slope changes at the expected coincidence channels 54, 82, 103 and 114. The energy mean value and the energy width of each coincidence channel are extracted by fitting the post-bremsstrahlung electron energy distribution with a product of two error functions

$$f(x) = \frac{p_2}{4} \cdot \left(1 + Erf\left(\frac{x - p_0 + p_1}{p_3}\right)\right) \cdot \left(1 + Erf\left(\frac{-x + p_0 + p_1}{p_3}\right)\right). \tag{4.1}$$

Here, the parameter p_0 is the mean value of the distribution, p_1 is the half width, p_2 represents the maximum while p_3 gives the slope of the error function. In the ideal case, based on the geometry of the scintillators a rectangular energy distribution is expected. This distribution is smeared out due to the size and the divergence of the primary electron beam. As an example, the energy distribution of

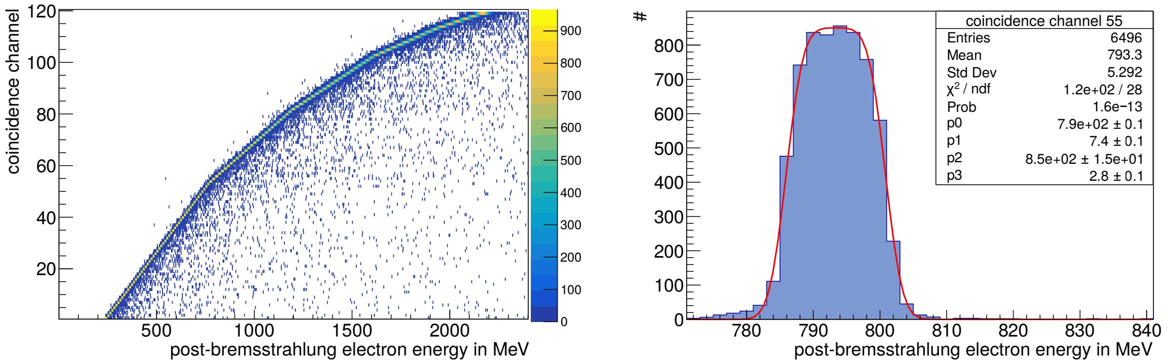

(a) Coincidence channel being hit depending on the simulated post-bremsstrahlung electron energy. The colour code give the number of entries.

(b) Energy distribution for coincidence channel 55 fitted with eq. 4.1.

Figure 4.8: Simulation of expected energy mean value and energy width per coincidence channel of the tagger hodoscope.

the post-bremsstrahlung electrons detected in the coincidence channel 55 is given in figure 4.8b. The expected smearing of the energy distribution is clearly visible. The results of the fit by equation 4.1 are also shown.

Figure 4.9a shows the extracted energy mean values which are fitted with linear slopes considering the five regions of different energy binning. The slopes of the fits shown in red correspond to the energy binning of the hodoscope. The energy bins amount to $0.42\% E_0$, $0.63\% E_0$, $0.84\% E_0$, $1.26\% E_0$ and $1.72\% E_0$ and agree with the design values presented in section 4.3.2. In figure 4.9b it is visible that the energy widths of the coincidence channels do not remain constant starting from channel 86. This is expected, since the vertical hodoscope can not be placed in the focal plane of the dipole magnet. Still, for coincidence channels smaller than 86, the energy widths match with the energy binning. After veri-

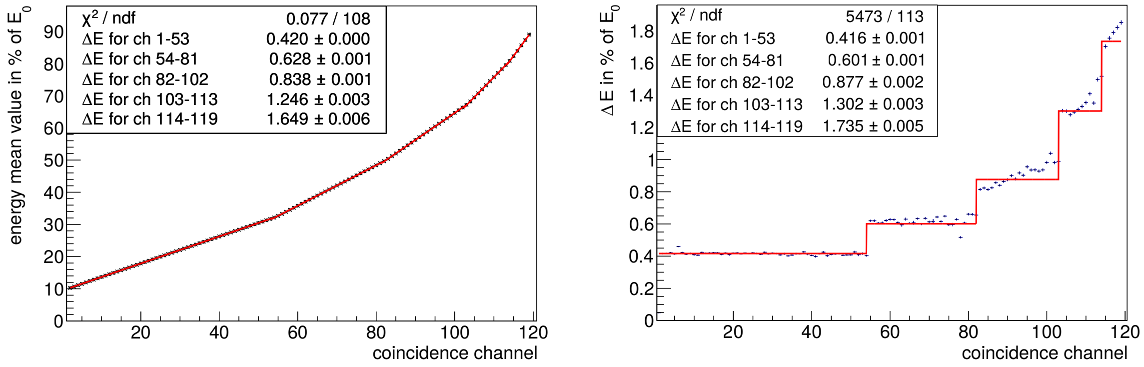

(a) Energy mean values in % E_0 for each coincidence channel. Each region of different energy binning is fitted with a linear function shown in red. Linear behaviour is given over the full tagged energy range. The slopes of the linear functions correspond to the energy binning and are in agreement with the design values by better than 5%

(b) Energy widths in % E_0 for each coincidence channel. The energy widths remain constant in the first two regions. Since the vertical part of the hodoscope is not placed in the focal plane of the dipole magnet the energy widths do not remain constant for the subsequent regions.

Figure 4.9: Expected energy mean values and energy widths for each coincidence channel of the tagger hodoscope.

fying that the designed scintillator positioning reflects in the simulation the desired linear dependency of the post-bremsstrahlung electron energy on the coincidence channels, the mechanical frame of the hodoscope is developed. The design of the mechanical structure of the hodoscope is presented in the following sections.

4.3.4 Mechanics

Based on the scintillator positioning described in section 4.3.2 the mechanical structure of the tagger hodoscope is developed. Due to spatial constraints (see section 4.1) the hodoscope has to be split into a horizontal and a vertical part (see figure 3.3). Both parts of the hodoscope are mounted separately to the dipole magnet and fixed together with dowel pins. For the mechanical design of the hodoscope, the main focus was set to a simple maintenance of scintillators and photomultipliers without affecting the energy calibration (see section 4.4.4). Since the horizontal part can be placed in the focal plane of the dipole magnet, it is possible to keep the design of the mechanical support simple (see figure 4.10a and 4.10b).

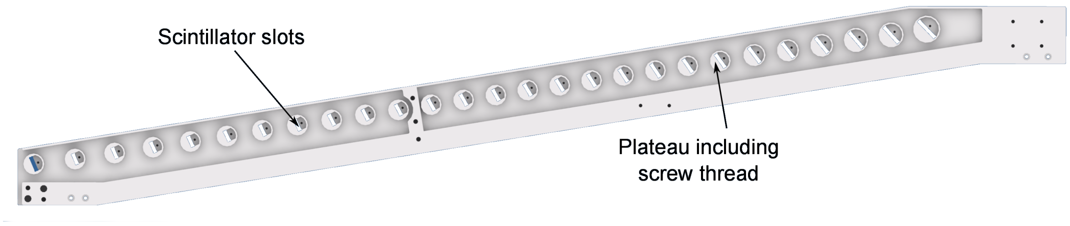

(a) Technical scheme: Side view of horizontal tagger hodoscope.

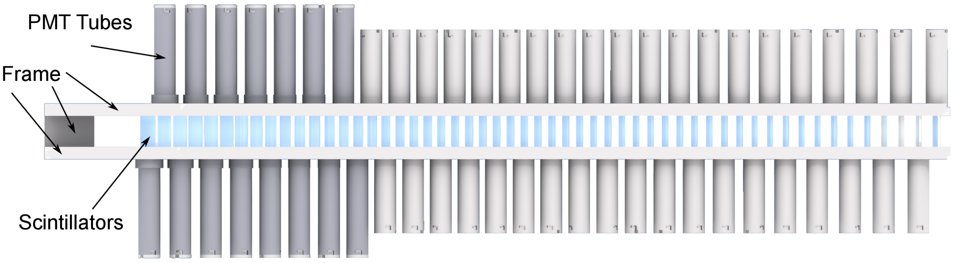

(b) Technical scheme: Top view of the horizontal tagger hodoscope.

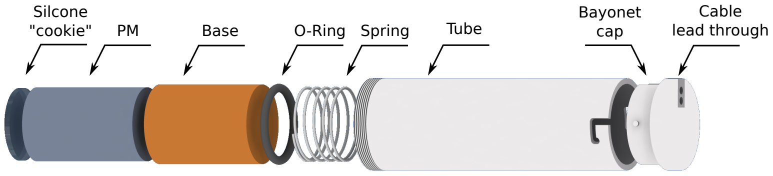

Figure 4.11: Technical scheme of a Photomultiplier assembly.

Both frames of the horizontal and vertical hodoscope are made of aluminium. The horizontal one consists of two side walls, which are connected at both ends with each other. The scintillators are inserted through rectangular slots which are contained in the side walls and can be positioned with a precision of

< 0.2 mm. Each scintillator is wrapped in one layer of aluminium foil to enhance the light collection and to avoid cross talk. The rectangular scintillator slots are surrounded by a plateau. Each plateau includes a screw thread and allows to mount an aluminium or iron tube (see section 4.3.5) which is used to keep a photomultiplier for the read out of the scintillator. Some aluminium tubes which are closer to the dipole magnet are longer than the remaining ones. In this case the scintillators are wider than the diameter of the active area of the photomultipliers. Hence, light guides are required for an effective light collection. Due to the additional material of the light guides the tubes have to be prolonged. Figure 4.11 shows a technical scheme of one photomultiplier assembly. The photomultipliers are arranged in alternating order due to the dimension of the photomultipliers.

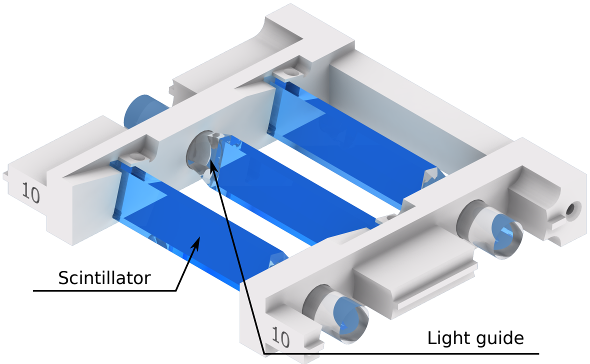

(a) Scintillator slide.

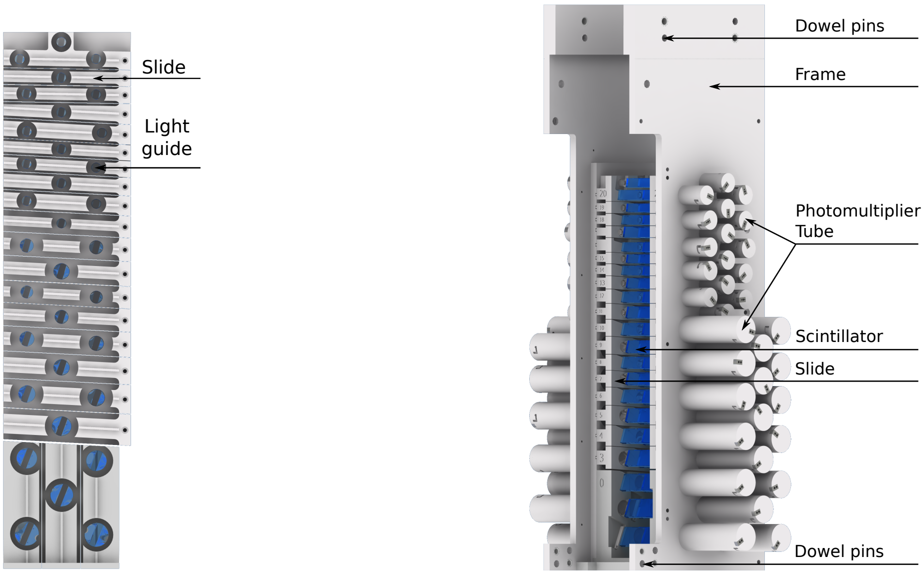

(b) Side view of the scintillator slides setup without frame and aluminium tubes.

(c) Full setup of the vertical tagger hodoscope.

Figure 4.12: Technical schemes of the vertical tagger hodoscope.

For the optical connection a ~2 mm thick round layer of silicone (cookie) is placed between the scintillator and the photomultiplier. The silicone cookie is kept in position by pressing the photomultiplier against the scintillator with a spring which is placed between the base of the photomultiplier and the closing of the tube. To keep the horizontal part light tight, the frame is closed with black foil. This design allows to perform maintenance on single channels. For the vertical part, a more complicated design is required, which is based on the design of a vertical prototype [48]. The detector is divided into 21 horizontal aluminium slides. Three scintillators are group together in 20 slides (see figure 4.12a), while one slide contains six scintillators. Each slide consists of two side walls with individually matched slots for precise positioning of the scintillators by < 0.2 mm. Both side walls are connected with an additional aluminium bar and dowel pins. Light guides are glued to the scintillators, since the width of the scintillators is larger than the diameter of the sensitive area of the photomultiplier. Due to their size, the photomultipliers are arranged in alternating order also in the vertical hodoscope. As in the horizontal part, each scintillator is wrapped in aluminium foil and the optical connection is done with a silicone cookie. The slides are kept in position with a precision of < 0.2 mm by an aluminium frame which is shown in figure 4.12c. Aluminium tubes which include the photomultipliers and their bases are screwed inside the frame. Due to the use of different kind of photomultipliers, these aluminium tubes have different sizes. With this design it is possible to have access to single photomultipliers and groups of three or six scintillators. The replacement of slides does not affect the energy calibration, as discussed in section 4.4.4.

4.3.5 Fringe field of the dipole magnet

18 photomultipliers on the horizontal part of the tagger are installed under the dipole magnet at distances ranging between 4.5 cm and 10.5 cm. The effect of the magnetic field on the photomultipliers is studied in order to identify the best solution to shield the photomultipliers. The x and y component of the fringe field were measured with a hall probe at the position of the closest photomultiplier to the dipole magnet. Operating the magnet for a primary electron beam energy of 3.2 GeV, leads to a measured field value of 2.8 mT for the larger component B_x. A pair of Helmholtz coils was setup in a black box to produce a homogeneous magnetic field of 2.8 mT. To study the effects of such a field on the photomultipliers of the tagging system, one of them is placed in between the Helmholtz coils and powered with the nominal supply voltage of 700 V. As a light source a LED light pulser is used to illuminate the photomultiplier. The amplitude of the photomultiplier output is observed with an oscilloscope with an without powered Helmholtz coils. The effect of the magnetic field on the photomultiplier is investigated for different

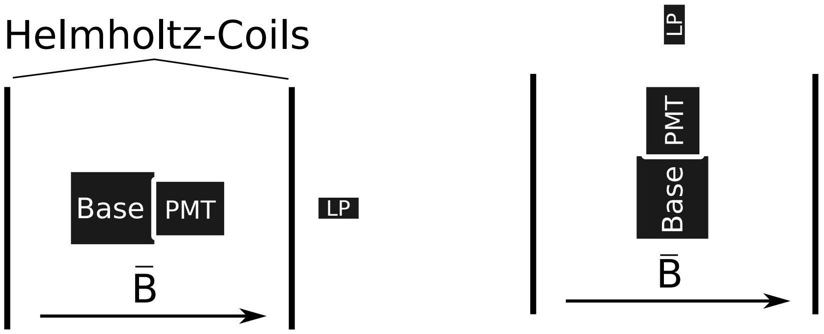

(a) Magnetic field parallel orientated to PMT axis.

(b) Magnetic field orthogonally orientated to PMT axis.

Figure 4.13: Test setup to investigate the influence of a homogeneous magnetic field on the PMT using Helmholtz coils.

orientations of the photomultiplier in the magnetic field of the Helmholtz coils. Figure 4.13a and 4.13b show a scheme of the test setup with the two different orientations of the photomultiplier in the magnetic field. The measured amplitude of the output signal of the photomultiplier in absence of the externally applied magnetic field amounts to 226.4 mV. By turning on the Helmholtz coils and orientating the photomultiplier longitudinally to the external magnetic field as shown in 4.13a the amplitude of the output signal drops by 45% to 124.4 mV (see figure 4.14a and 4.14b). For a transversal orientation of the photomultiplier to the magnetic field, the amplitude drops by 11% to 201.2 mV (see figure 4.14c). In a next step the photomultiplier including its base is placed into a shielding iron tube of 2 mm thickness

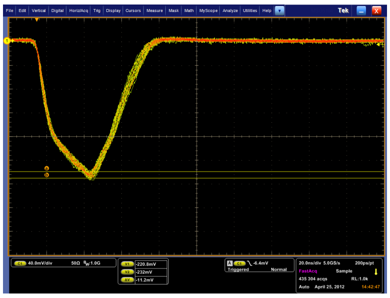

(a) PMT parallel orientated to magnetic field (figure 4.13a). Helmholtz coils turned off and without shielding.

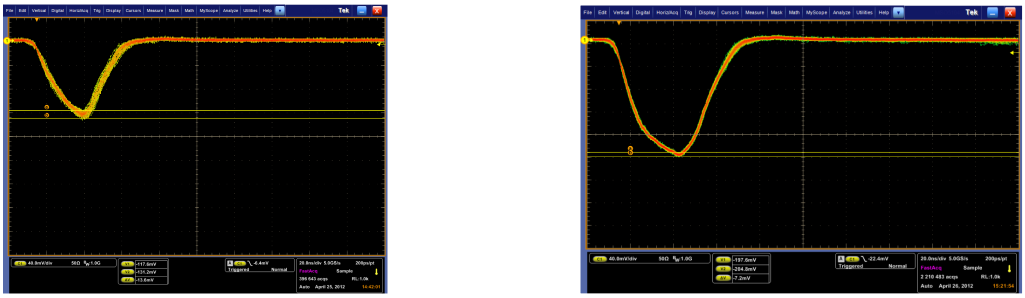

(b) PMT parallel orientated to magnetic field (figure 4.13a). Helmholtz coils turned on and without shielding.

(c) PMT orthogonally orientated to magnetic field (figure 4.13b). Helmholtz coils turned on and without shielding.

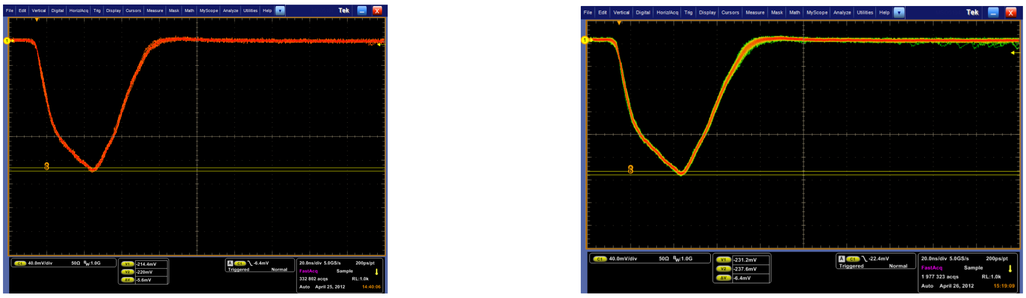

(d) PMT parallel orientated to magnetic field (figure 4.13a). Helmholtz coils turned on and with shielding.

(e) PMT orthogonally orientated to magnetic field (figure 4.13b). Helmholtz coils turned on and with shielding.

Figure 4.14: Measured PMT signal using a LED light pulser.

and the amplitude of the output signal is remeasured while the Helmholtz coils were turned off. Figure 4.14d and 4.14e show the output signal of the shielded photomultiplier longitudinally and transversally orientated to the magnetic field. For longitudinal orientation, the amplitude of the shielded photomultiplier is not fully recovered, being still 5% lower than without external magnetic field. In contrast, due to the shielding of the earth's magnetic field, the amplitude is even slightly higher for the transversal orientation. At the end the aluminium tubes closest to the dipole magnet are replaced by 3 mm thick iron tubes.

4.4 Commissioning and calibration

In this chapter, the characteristics like time resolution, rate stability and detection efficiency are presented. Subsequently, the energy calibration of the hodoscope and its stability against maintenance are discussed.

The function of the tagging system is to provide a precise energy and time information of the produced bremsstrahlung photons. This requires an energy calibration of the tagging hodoscope. Its stability with respect to maintenance needs to be investigated.

Since, the BGO-OD experiment investigates photo-production experiments with low cross sections, high photon fluxes are required. The other main requirement of the tagging system is, that is has to work in a stable condition up to total rates of 50 MHz. Further important characteristics like time resolution, rate stability and detection efficiency are determined.

4.4.1 Detector configuration and time resolution

The gain matching of all photomultipliers is the first step to bring into operation the tagger hodoscope. Therefore, as mentioned in section 4.2, the x1 amplified outputs of the AFAs are fed to a 16 channel CAEN DT5742 sampling ADC. Figure 4.15 shows as an example an ADC pulse spectrum of one gain matched photomultiplier using an arbitrarily chosen high threshold of 75 mV. The expected Landau distribution is clearly visible. After the gain matching of all the photomultipliers, the thresholds on the B-FrED boards are set. The B-FrED is based on the dual-threshold technique, meaning that the analogue

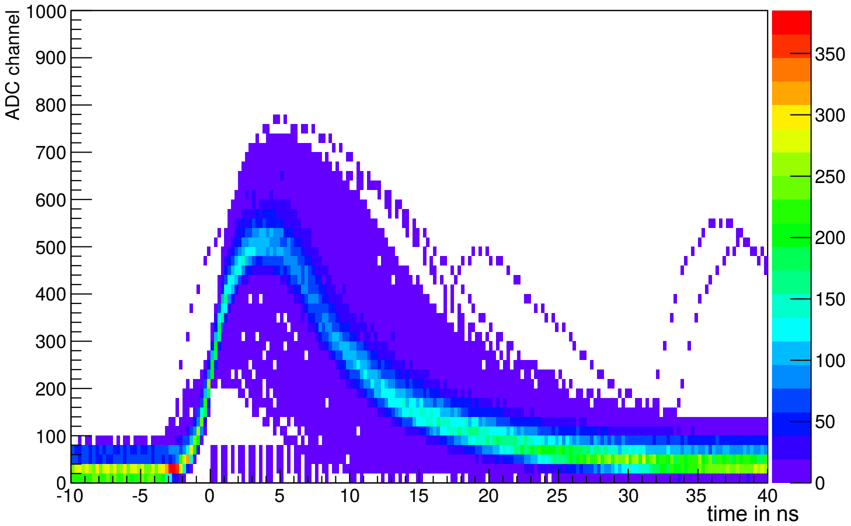

Figure 4.15: Typical ADC pulse spectrum in dependence of the time in ns of a gain matched PMT.

signal is compared to a low and a high threshold. The signal has to exceed the high threshold in order to not be ignored. The timing of the signal is measured in correspondence of the low threshold minimising the time-walk and improving the time information. To choose an appropriate pair of thresholds, a threshold scan is performed. This means that in an interactive process, low and high threshold of the B-FrEDs are changed and for each pair of thresholds, the scaler rate of each tagger channel is normalised by the FluMo scaler rate. The values of the threshold used in a scan are listed in table 4.1 leading to 42 data sets for each tagger channel. The figures 4.16a and 4.16b show the scaler rate distributions for a low threshold of 40 mV and a high threshold of 100 mV for channel 66.

Low Th in mV	10	20	30	40	50	60	70
High Th in mV	70	80	90	100	110	120	

Table 4.1: Thresholds used in a threshold scan.

As displayed in figure 4.16a, the scaler rate of the tagger channel decreases by increasing the high threshold which has several reasons. For high thresholds up to 90 mV noise is reduced. Starting from 120 mV, were the high threshold is too large compared to the low threshold, signals get lost. The signal is compared to both, low and high threshold. Since the low threshold is exceeded first, it is delayed by a fixed time (see figure 4.17). Once the high threshold is reached, a gate opens to check for the delayed signal which did exceed the low threshold. If the high threshold is too high, the signal needs too much time to overcome the high threshold. Consequently, the gate opens too late. For much larger high thresholds values, the signal does not overcome the threshold. In the example of figure 4.16a, a good high threshold value would be between 90 mV and 110 mV for which the scaler rate remains constant.

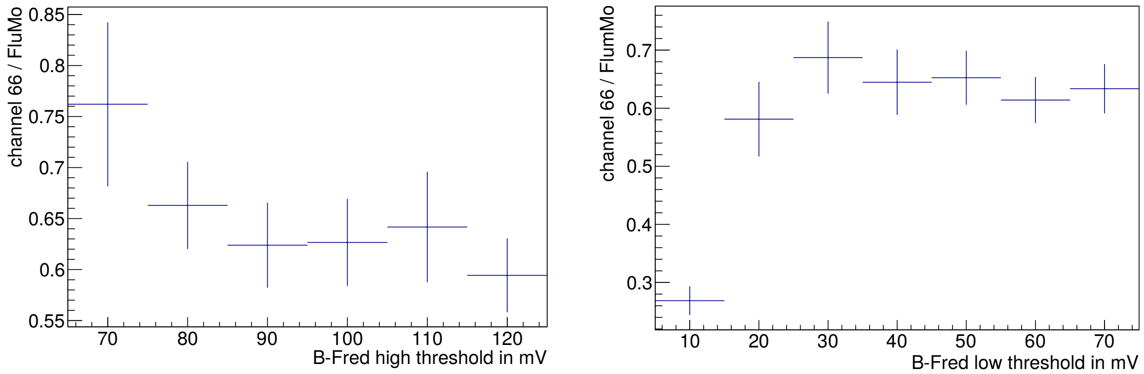

(a) Normalised scaler rates for a fixed low threshold of 40 mV and varying high thresholds.

(b) Normalised scaler rates for a fixed high threshold of 100 mV and varying low thresholds.

Figure 4.16: Scaler rates of tagger channel 66 normalised by FluMo scaler rates for different low and high thresholds.

Figure 4.16b shows the scaler rates in dependence of the low threshold. One can see that almost no signals are accepted for a low threshold of 10 mV. The logical scheme of the shaper stage is shown in figure 4.17 to illustrate this problem. The shaper stage is realised using two D-FlipFlops for which the output signal Q_i is synchronised with a clock C_i. Q_i transmits the signal D_i if a rising edge is detected at C_i. If the low threshold is too low, the input at C_2 is always active. Hence, no rising edge can be detected and therefore no output signal is transmitted by the shaper stage. Starting from 30 mV, no significant change in rate is visible in figure 4.16b and therefore a value of at least 30 mV should be choosen for the low threshold.

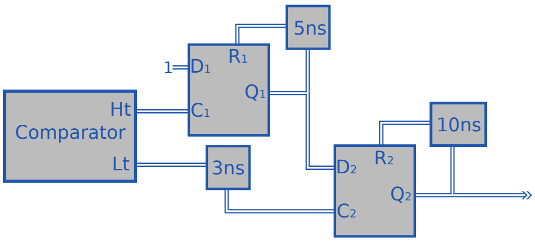

Figure 4.17: Scheme of the discriminator shaper stage. The signal shaping is performed using two D-FlipFlops. A gate shown by D_2 is opened for 5 ns by the high threshold signal in which the low threshold signal delayed by 3 has to arrive in order Q_2 delivers a 10 ns long active signal

It is expected that the time resolution of the tagger channels is mainly affected by the low threshold. The time resolution is determined in dependency of low and high threshold for each tagger channel separately to choose the appropriate low threshold and cross check the dependence of the time resolution on the high threshold. For the determination of the time resolution, the time difference distribution of two adjacent tagger channels is fitted to a Gaussian function. The standard deviation of the Gaussian fit corresponds to the combined time resolution of the two adjacent tagger channels. Assuming that both channels contributes in the same way to the error, the time resolution of a single channel is given by $\sigma_{ch} = \sigma_{coinc}/\sqrt{2}$. Figure 4.18a and 4.18b show the time resolution for a single channel depending on low and high threshold for a subset of ETEnterprise and Hamamatsu photomultipliers. The error bars on

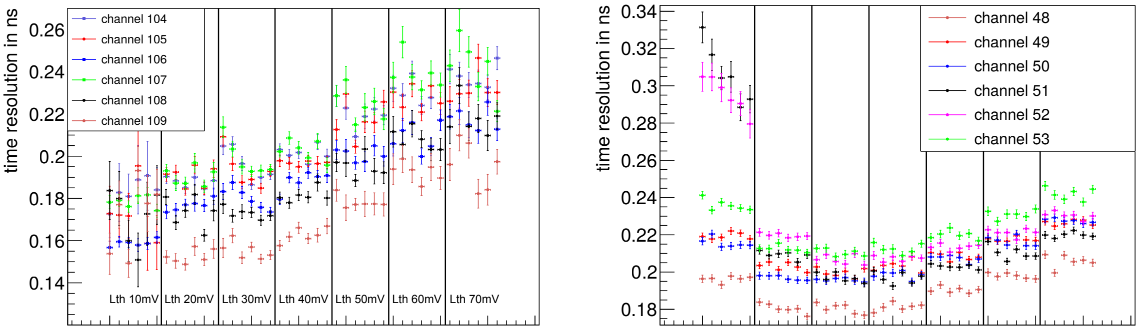

(a) Time resolution of randomly chosen Hamamatsu PMTs.

(b) Time resolution of randomly chosen ETEnterprise PMTs.

Figure 4.18: Time resolution of the Hamamatsu and ETEnterprise PMTs depending on low and high thresholds. The black lines indicate measurement with same low threshold in bins of 10 mV.

the time resolution are the errors on the standard deviation from the Gaussian fit. Each block indicated by the black solid lines corresponds to a fixed low threshold for which the high threshold is changed according to table 4.1. It is visible that the time resolution strongly depends on the low threshold. In the case for figure 4.18a and 4.18b the thresholds for both kind of photomultipliers are set to $Lt = 30\,\mathrm{mV}$ and $Ht = 100\,\mathrm{mV}$.

4.4.2 Rate Stability and detection efficiency

One of the main requirements on the tagging system is the stable operation at high rates. Due to the bremsstrahlung cross section which is proportional to dE_γ/E_γ, photomultipliers covering the region of high energetic electrons are exposed to the highest rates. Figure 4.19 shows the scaler rates of each single channel of the tagger hodoscope using a copper radiator with a thickness of 67 μm and a primary beam current of about 500 pA. Starting from channel 117 the scaler rates do not increase corresponding to the bremsstrahlung cross section. The reason for this deviation is most probable saturation of these photomultipliers. Photomultipliers which cover low energetic post-bremsstrahlung electron energies are also exposed to the lowest rates. They are expected to not suffer saturation effects and therefore can be used as reference channel to test the rate stability. For the investigation of the rate stability of the photomultipliers which are exposed to the highest rates, scaler rate distributions are measured for different primary beam currents and different thicknesses of the copper bremsstrahlung radiator. Figure 4.20a and 4.20b show the scaler rates of reference channel 59 against the scaler rates of channels 115 to 120 for primary beam currents ranging from 257 pA to 583 pA and radiator thicknesses of 100 μm and 200 μm. Except for channel 118 it can be seen that, the tested photomultipliers start to saturate for rates between 5 MHz and 7 MHz. For the example shown in figure 4.19 a stable condition is guaranteed for channels up to 116 with a total tagging rate of about 54 MHz.

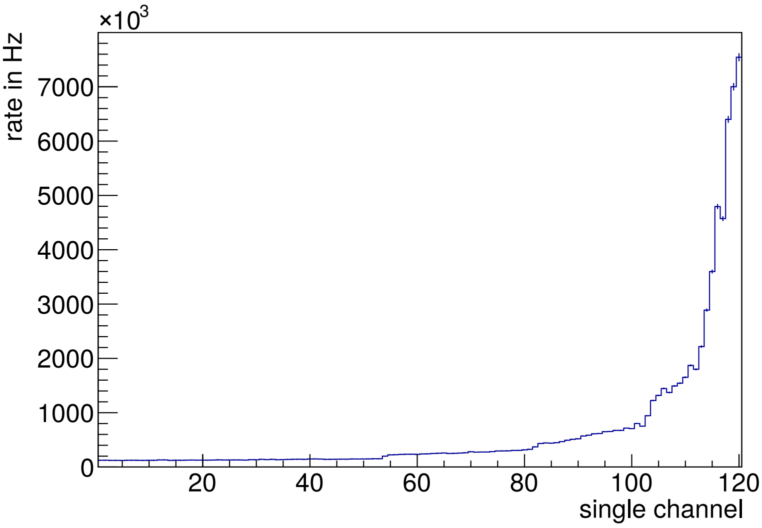

Figure 4.19: Single channel tagger spectrum with optimised high voltages and discriminator thresholds.

Due to the saturation of the photomultipliers, it is expected that the detection efficiency decreases. Figure 4.21 illustrates the principle of a detection efficiency test. The test detector is sandwiched by two smaller trigger detectors, one providing the start and one the stop time. If a particle originating from the source is seen by the start and stop detector, it is expected, that within the time window given by the trigger detectors, the particle is seen by the test detector. The detection efficiency can be written as:

$$\varepsilon = \frac{N_{start,test,stop}}{N_{start,test,stop} + N_{start,stop}} \tag{4.2}$$

Due to the arrangement and geometry of the scintillators, this concept cannot be applied on the tagger hodoscope and has to be slightly modified. Instead of using a start and stop detector, the trigger is generated by an OR of all single channels of the hodoscope. Still, due to the arrangement, except for the first and last one, each scintillator is partially sandwiched by two neighbouring scintillators. The algorithm to test the detection efficiency of one tagger channel is the following. First, it is looked for two scintillators with index $i-1$ and $i+1$, which have seen a particle within a time window corresponding to three times their time resolution. Secondly, it is checked if scintillators with index $i-2$ and $i+2$ were hit in the same time window. If such neighbouring hits are found, these events are treated as background

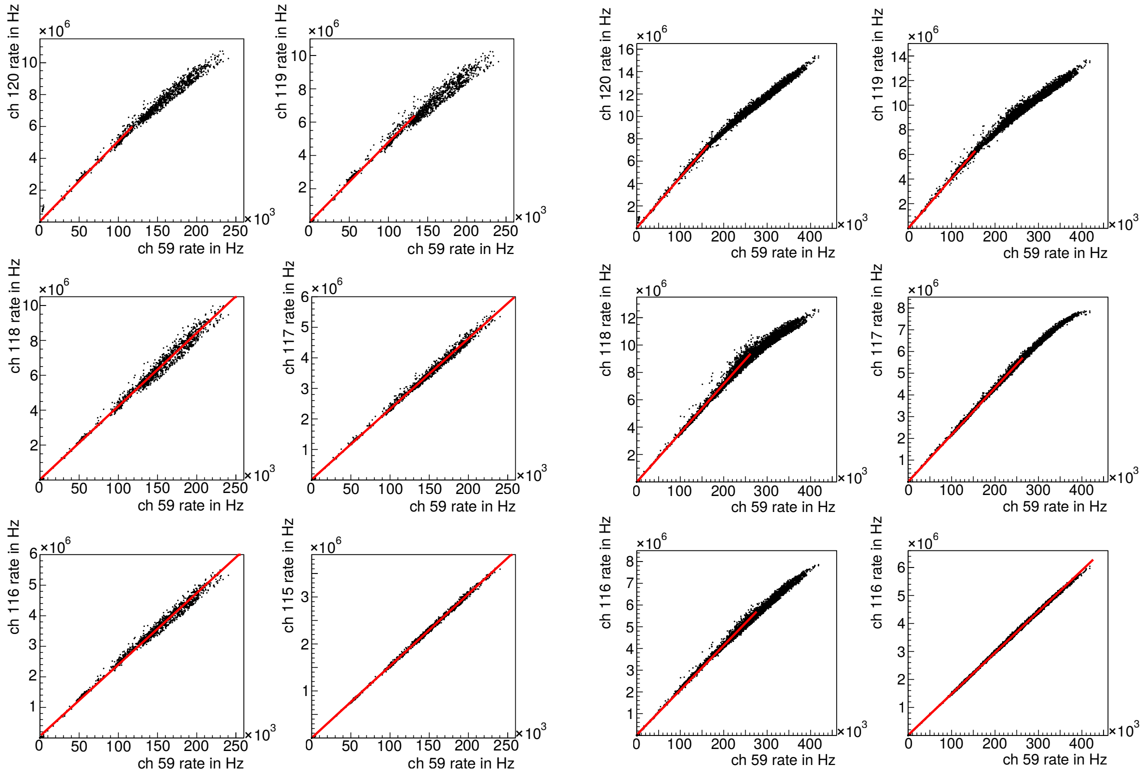

(a) Scaler rates using a 100 μm copper radiator.

(b) Scaler rates using a 200 μm copper radiator.

Figure 4.20: Scaler rates for tagger channels 115 to 120 versus scaler rates of channel 59 with two different radiators.

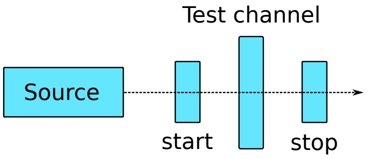

Figure 4.21: General efficiency measurement. Particles emitting from a source penetrate three detectors. If a particle is seen in a certain time window by the first and the last detector, the particle should be seen by the sandwiched one.

and are rejected. In this way it is avoided to consider coincidences of four and more scintillators which are geometrically not allowed. The last step is to check if a hit has been seen in scintillator i within the time window. If scintillator i was hit, the event is treated as efficient. The detection efficiency is then determined via

$$\varepsilon = \frac{N_{i-1,i,i+1}}{N_{i-1,i,i+1} + N_{i-1,i+1}} \tag{4.3}$$

Figure 4.22 shows the resulting determined detection efficiencies for the tagger channels 2 to 118. It is remarkable, that for the lower half of the hodoscope the determined efficiencies are in general lower than for the upper half. The only known difference is that the two halves of the detector are connected to two different FPGA boards. Further investigations are necessary to reach an unambiguous interpretation of this discrepancy. Detection efficiencies of ~99% are determined in the upper half for channels up to index 88. For higher channels, two structures are visible. First, the detection efficiency drops for channels

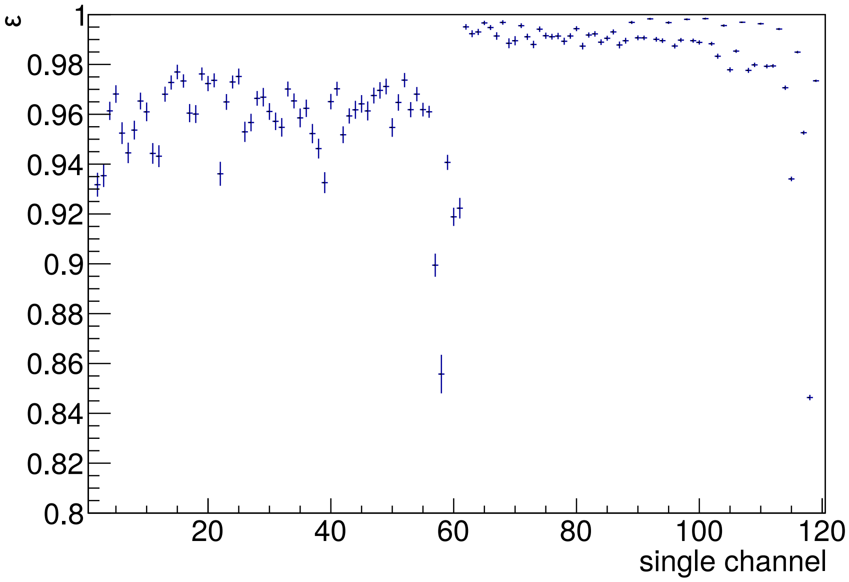

Figure 4.22: Determined detection efficiencies for each tagger channel.

starting from channel 113 which is related to the previously discussed saturation of the photomultipliers. Secondly, each third channel shows a larger detection efficiency, which is related to the geometry of the vertical part of the tagger hodoscope. The scintillators in the first and third column of the hodoscope are not sandwiched by two neighbouring scintillators and therefore the determination of the detection efficiency is effected by background as illustrated in figure 4.23. The scintillators are arranged such, that the surface of the scintillators is perpendicular to the expected post-bremsstrahlung electron trajectories. Hence, a post-bremsstrahlung electron has to pass through two or three adjacent scintillators. This is shown by the solid black lines. Particles not originating from expected post-bremsstrahlung electron trajectories illustrated by the dotted lines (scattered post-bremsstrahlung electrons or secondary particles) can pass through scintillators which are not adjacent. The amount of scattered and secondary particles increases with rate and post-bremsstrahlung electron energy. These particles produce hit patterns in the tagger hodoscope, which are identified as inefficient events and therefore lower the determined detection efficiencies.

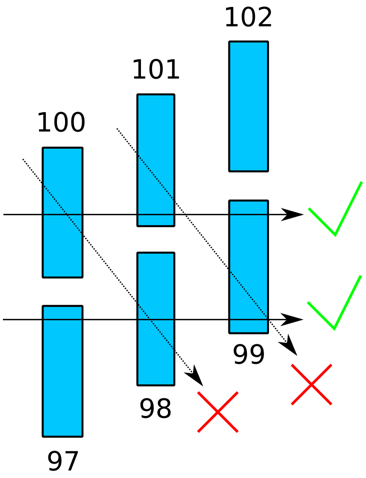

Figure 4.23: Particles not originating from expected post-bremsstrahlung electron trajectories cause wrongly determined inefficiencies.

4.4.3 Tagger time alignment and clustering

Due to its good time resolution, the tagging system provides the start time of an event for the BGO-OD experiment for data trigger conditions. In the ideal case, a tagger trigger signal is generated if an electron passes through two adjacent scintillators within a time window of 4.2 ns. Therefore all single channels have to be aligned with respect to each other. Data is taken requiring the coincidence between FluMo and an OR of all tagger channels as trigger condition to perform the time alignment of the tagger signals. Subsequently, the time difference between FluMo and all single tagger channels is determined. The time differences are adjusted on the FPGA within steps of 5/6 ns. Figure 4.24a shows a not aligned time spectrum of the tagger hodoscope for all single tagger channels.

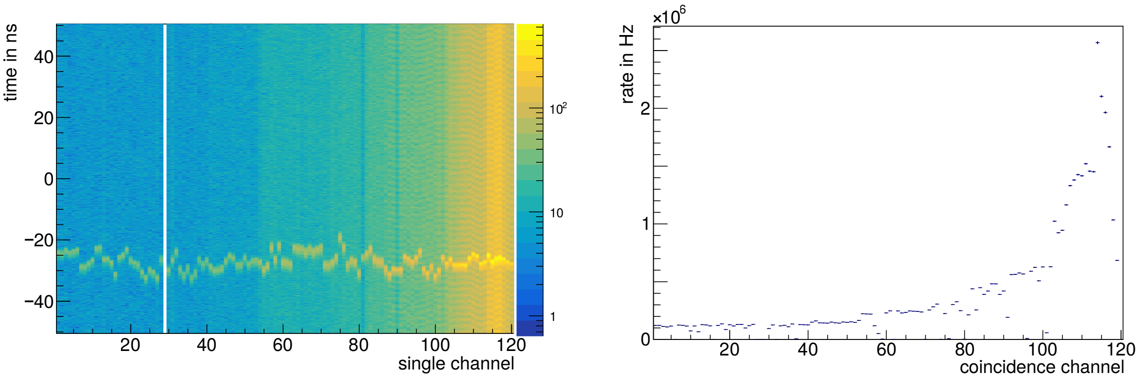

(a) Single tagger channel vs time in ns. The colour code gives the number of entries in logarithmic scale. Neighbouring tagger channels are misaligned by more than 7 ns.

(b) Coincidence scaler rates without time alignment. Coincidence scaler rates decrease if the time difference between two neighbouring single tagger channels is more than the coincidence time window.

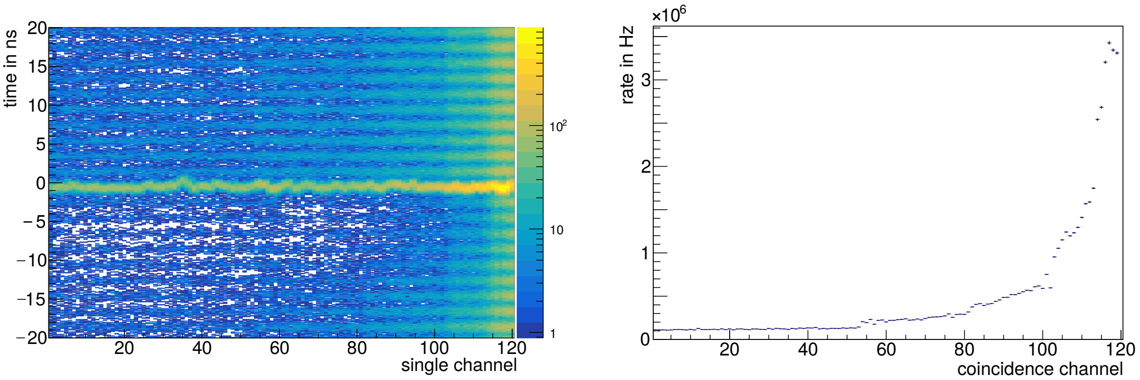

(c) Single tagger channel vs time in ns. The colour code gives the number of entries in logarithmic scale. The times of all single tagger channels are aligned in steps of 5/6 ns and shifted to zero. A periodic structure of 2 ns is visible which corresponds to the bunch wise extraction of the electrons.

(d) Coincidence scaler rates for an aligned tagger hodoscope. No holes in the coincidence channel spectrum compared to figure 4.24b are present.

Figure 4.24: Time spectrum of the tagger hodoscope and the corresponding coincidence tagger spectrum.

It is visible that neighbouring tagger channels are misaligned by more than the coincidence time window. Consequently, coincidences are not detected and therefore less coincidence trigger signals are generated. Figure 4.24c shows the same spectrum after time alignment. Hence, the missed coincidences are restored as shown in figure 4.24d.

An event based time correction on software level is applied to improve the time resolution of each single tagger channel. It is checked which coincidence channel is closest in time with the trigger time. The time of the later hit member of the coincidence is determined. Subsequently, the times of all single tagger channels are corrected by this offset. Figure 4.25a shows the time distribution for all single tagger channels after the event time correction is applied on the data shown in figure 4.24c. A sharp line at zero caused by the event time correction can be seen. A better separation of the bunch structure of the electron beam and therefore a better identification of the electron which generated the trigger is achieved with the event time correction. The time distribution of the signals coming from all the channels of the tagging hodoscope is shown in figure 4.25b. Clearly visible is the prompt peak around 0 ns, which includes the events correlated to the trigger.

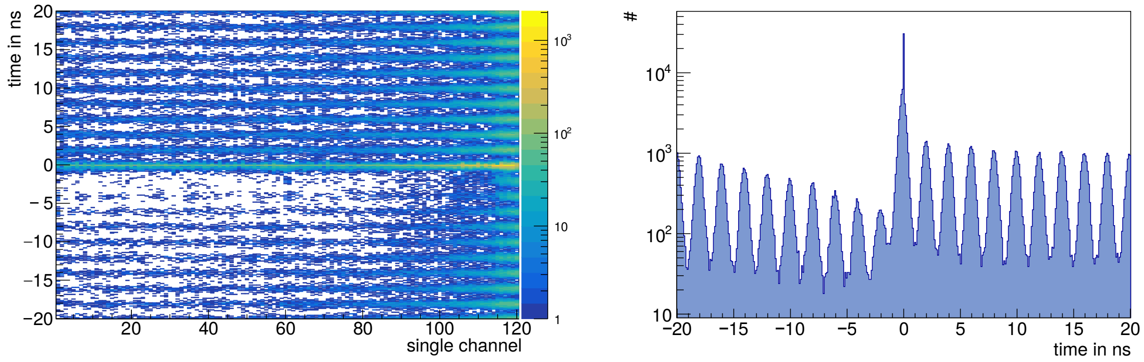

(a) Single tagger channel vs time in ns. The colour code gives the number of entries in logarithmic scale. The periodic structure of 2 ns did become more sharp.

(b) Tagger time spectrum in logarithmic scale. The bunches of the extracted electron beam are well isolated. The event time correction cleans the events caused by the trigger from detected electrons coming from neighbouring bunches and increases the time resolution.

Figure 4.25: Time spectrum after the time alignment and event time correction.

Post bremsstrahlung electrons which pass through the tagger hodoscope on their nominal trajectories are usually detected by two or three adjacent scintillators. After the time alignment is performed, the reproduction of double and triple hits, which are called cluster, is investigated in data and compared with simulation. The time information of each single channel is used to reconstruct the clusters. Hits from two or more adjacent scintillators form a cluster if they are all in a time window of 3σ of the tagging hodoscope time resolution. For simulated data, single electron events are generated. Hence, double electron events which can occur due to high rates are not considered. To be able to compare the measured data with the simulation, only events which are lying inside the prompt peak are considered. Figure 4.26a and 4.26b show the number of reconstructed clusters per event for simulated and real data. In simulations, where only one electron is simulated in each event, ~0.5% of the events show more than one cluster. These additional clusters originate from particles generated in scattering processes in the kapton foil of the tagging magnet, in the air and in the scintillators. In real data, more than 5% of the events show more than one cluster in the prompt peak, corresponding to several bremsstrahlung processes taking place in the radiator almost at the same time due to the high intensity of the primary electron beam. Figure 4.27a and 4.27b show the reconstructed clustersize for simulated and real data. After the selection of clusters lying within the prompt peak, the cluster size distribution for real data

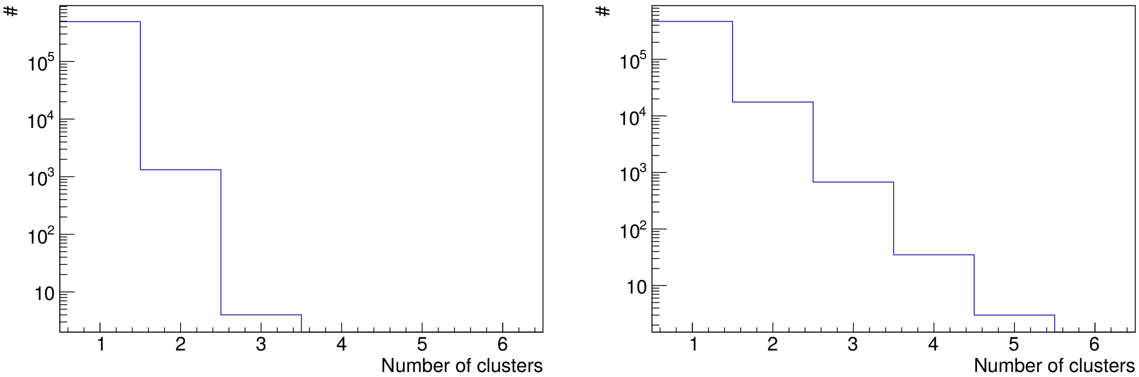

(a) Number of clusters for simulated single electron events.

(b) Number of clusters for real data.

Figure 4.26: Number of clusters per event for simulated and real data. Due to the high intensity of the primary electron beam, the tagger hodoscope detects more than one particle per event.

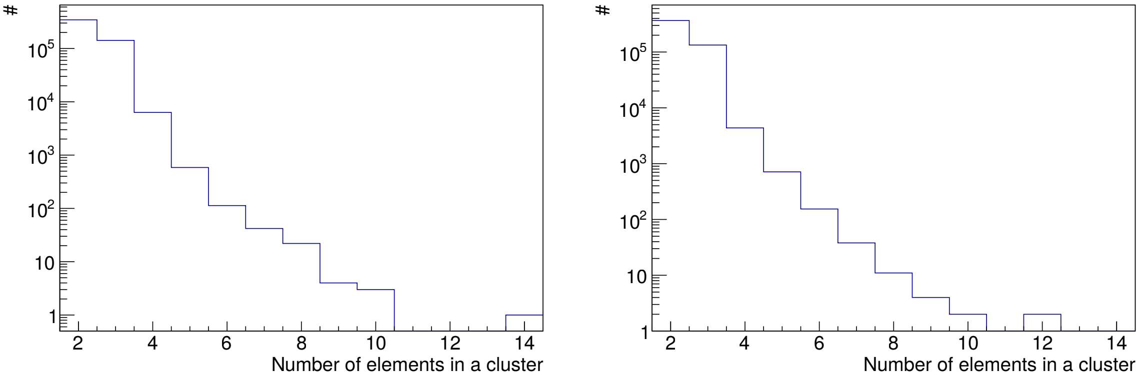

(a) Cluster size for simulated single electron events.

(b) Cluster size for real data.

Figure 4.27: Clustersize per event for simulated and real data.

resembles the one of simulated data. Clusters with more than 3 members correspond to rescattering of the post-bremsstrahlung electron within the scintillator or to the presence of secondarily produced particles hitting the tagger hodoscope.

4.4.4 Energy calibration

The main purpose of the photon tagger is to determine the energy of the produced bremsstrahlung photons, by detecting the corresponding post-bremsstrahlung electrons in the tagger hodoscope. The direct information given by the hodoscope is the index of the coincidence channel which did detect a post-bremsstrahlung electron. Hence, an energy calibration of the hodoscope is necessary to assign to each coincidence channel the corresponding post-bremsstrahlung electron energy. This allows to obtain the post-bremsstrahlung electrons energy from its detection position in the tagger hodoscope and therefore to determine the energy of the produced bremsstrahlung photon.

To perform an energy calibration, the primary electron beam with low intensity and with known energy E is bent by the tagging magnet directly into the hodoscope without previously hitting the bremsstrahlung radiator. By changing stepwise the magnetic field B, which is measured by a hall probe mounted at a fixed position inside the magnet, the beam is swept over the hodoscope (see figure 4.28a). This procedure provides the detection position in the hodoscope of the primary electron beam in dependence of the magnetic field strength B_{coinc} for a fixed primary beam energy E. Using this dependence together with the nominal values of E_0 and B_0 set during the performance of photo-production experiments (see figure 4.28b), the coincidence channels can be assigned their corresponding post-bremsstrahlung electron energy via:

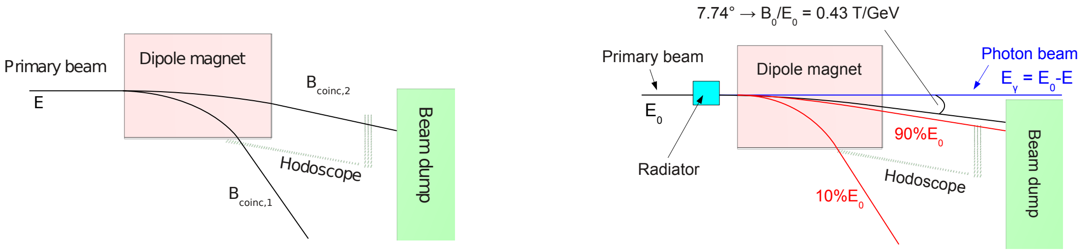

(a) The primary electron beam with energy E is bend for different values of B at different positions into the tagger hodoscope. For each value of B data is taken to determine the position of the electron beam in the tagger hodoscope.

(b) Nominal setting of the primary electron beam and the dipole magnet during data taking.

Figure 4.28: Principle of the energy calibration of the tagger hodoscope.

$$\frac{E_{coinc}}{E_0} = E \cdot \frac{B_0}{E_0} \cdot \frac{1}{B_{coinc}}. \tag{4.4}$$

To avoid radiation damage of the scintillators or saturation in the photomultipliers, the intensity of the primary beam was reduced such, that a rate of about 300 kHz was observed in the full tagger hodoscope. In figure 3.6b it is visible that for magnetic field values higher than 1.55 T the deviation of the linear behaviour of the dipole magnet is larger than 1%. Therefore, the energy calibration is started with an magnet field value of 1.5 T and reduced until the primary electron beam does not hit the vertical part of the hodoscope anymore. For each magnet current setting, 50.000 coincidence trigger events are taken. The energy calibration is performed with three different primary beam energies to verify the consistency of the results. In table 4.2 are shown the primary electron beam energies and the magnetic field step sizes used in the performed energy calibrations. The figures 4.29a, 4.29b and 4.29c show for each primary electron beam energy the dependency of all 119 coincidence channels on the magnetic field. The colour code illustrates the number of coincidental hits in two adjacent scintillators. No entries are available for channel 5 to 19, since these were not equipped during the energy calibration. Different

Primary electron beam energy in MeV	800	1270	1730
Magnet current step in A	1	10	3
Magnetic field step in mT	~1.7	5	17

Table 4.2: Electron beam and magnet parameters during tagger hodoscope energy calibration.

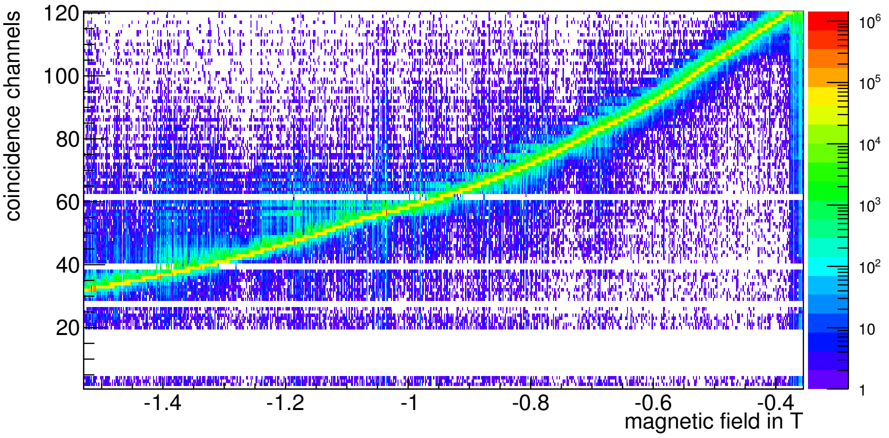

(a) Series of measurement using a primary electron beam energy of 800 MeV.

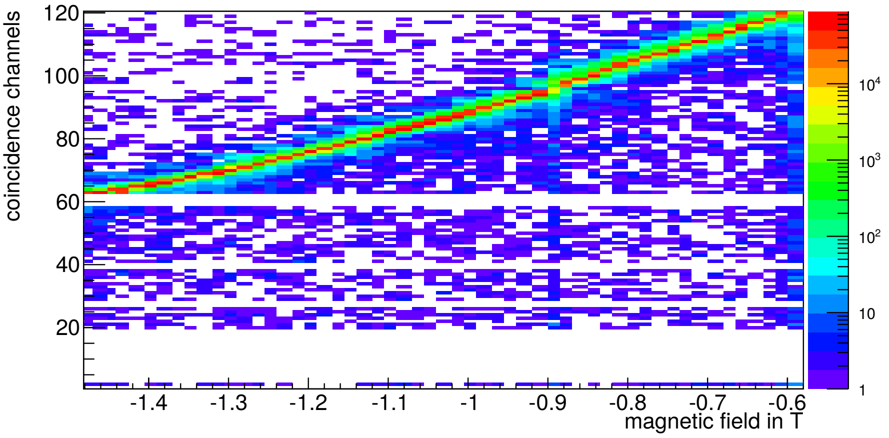

(b) Series of measurement using a primary electron beam energy of 1270 MeV.

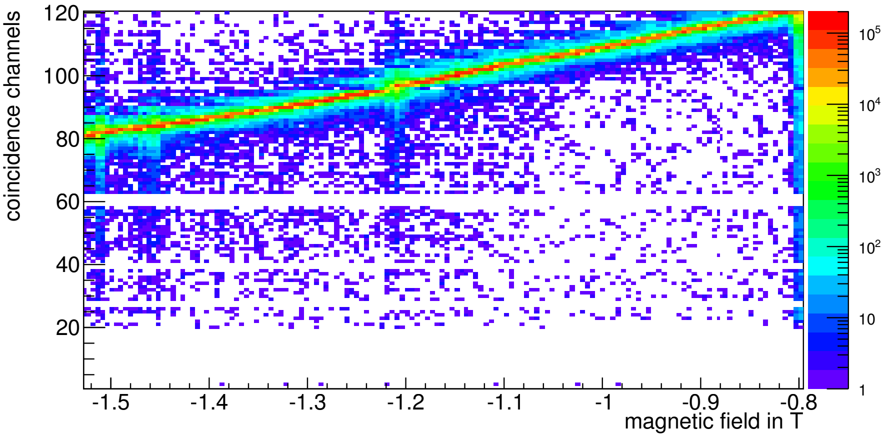

(c) Series of measurement using a primary electron beam energy of 1730 MeV.

Figure 4.29: Results of the energy calibration measurement for different primary electron beam energies. Plotted is the absolute magnetic field value versus the coincidence channel of the tagger hodoscope. The colour code gives the number of entries. The thresholds for channels 27, 39 and 61 could not be set correctly for technical reasons. Hence, only the primary electron beam is seen by these channels. The channels 5 to 19 were not equipped during the energy calibration, which explains the missing entries in the plots.

parts of the tagger hodoscope can be scanned with different primary electron beam energies using the same starting value for the magnetic field. With a starting magnetic field value of 1.5 T it is not possible to scan the full tagger hodoscope. For a complete scan of the tagger hodoscope a larger magnet field value would be required, but from figure 3.6b we know that the magnetic field value would not scale linearly with the applied supply current anymore. Hence, for the coincidence channels smaller than 36, the corresponding post-bremsstrahlung energy has been extrapolated.

To determine the energy mean value per coincidence channel, the same analysis as presented in section 4.3.3 is performed. Figure 4.30b shows for the hit distribution of coincidence channel 60, depending on the magnetic field using a primary electron beam energy of 800 MeV. One can see, that the hit distribution resembles the expected shape of a smeared rectangular function, which is fitted by equation 4.1. Using the mean value of the magnetic field distribution, given by p_0, allows the determination of the energy mean value per coincidence channel via equation 4.4. The errors on the mean value and the width of the distribution resulting from the fit are close to zero. The considered systematic errors are given by the resolution of the Hall probe, which amounts to 1 mT, and the uncertainty on the primary electron beam energy which is $10^{-3}E_0$. For the determination of the final errors on the energy mean value and the energy width, Gaussian error propagation is applied. Figure 4.31a shows the resulting energy mean

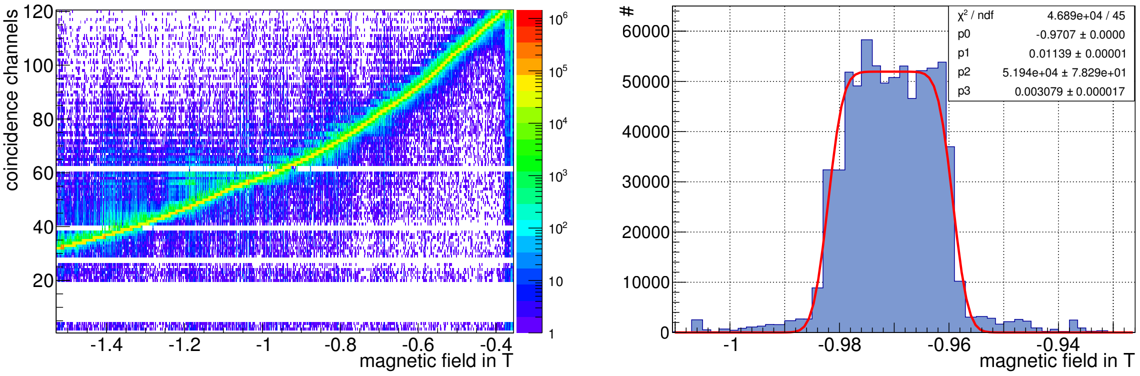

(a) Series of measurement using a primary electron beam energy of 800 MeV.

(b) Projection of coincidence channel 60 fitted with equation 4.1.

Figure 4.30: Determination of energy mean values and energy widths.

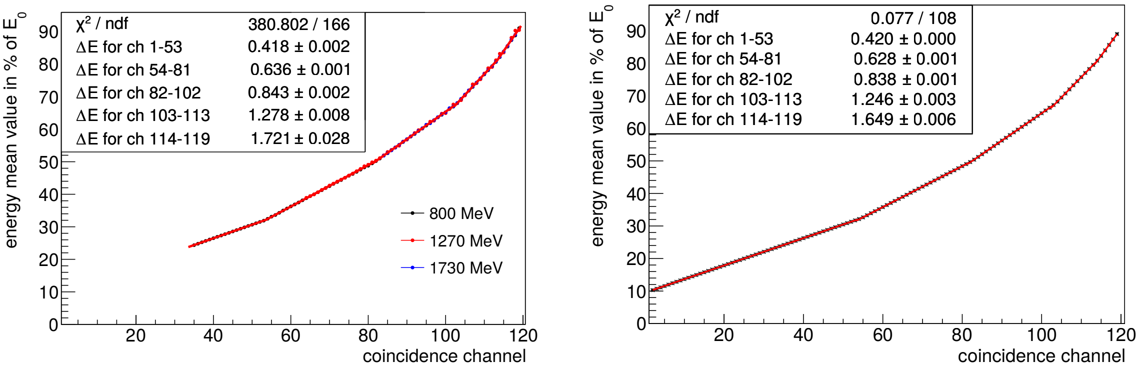

(a) Resulting energy mean values for real data.

(b) Resulting energy mean values for simulated data.

Figure 4.31: Resulting energy mean values compared with simulated data.

values in %E_0 for the primary electron beam energies of 800 MeV, 1270 MeV and 1730 MeV. Since the errors are of the order of ~0.5%, the errors are not visible in this plot. It can be seen that all the data points are in a very good agreement with each other. As already mentioned in section 4.3.3 the distribution consists of five regions in which the energy raises linearly but with different slopes in dependence on the coincidence channel. The slope of these linear functions corresponds to the energy binning of the hodoscope. Each region of different energy binning is fitted with a linear function. Comparing the results with simulated data (see figure 4.31b), an agreement of better than 2% is achieved.

The ratio of the resulting energy mean values from real to simulated data is shown in figure 4.32a and close to one. Constants are fitted to each region of different energy width which show an agreement of real to simulated data by better than 1%. A larger spread is observed in the data acquired at 1270 MeV. This effect is ascribed to the fact, that the step size in the magnet current was 3 to 10 larger compared to the other measurements. Figure 4.32b shows the comparison of the energy mean values from real data to simulated data considering the results from the series of measurement using a primary electron beam energy of 800 MeV and 1730 MeV. Beside a good agreement of real to simulated data, the comparison of the energy mean values show a systematic effect. The agreement of real to simulated data decreases for lower coincidence channels. To identify the reason for this decrease in agreement, a simulation with a misaligned beam and tagger hodoscope within the precision of the positioning was performed. Neither a transversal displacement of the primary electron beam from its central axis nor a misalignment of the tagger hodoscope within the positioning precision would contribute to this deviation. A second simulation was performed considering an angular displacement of the primary electron beam with respect to its nominal axis. It was observed that an angular displacement of the primary electron beam by 0.1 mrad can cause an effect comparable to the one visible in figure 4.32b. Other experimental observations discussed in section 5.1.5 support the hypothesis that an angular displacement of the primary electron beam by 0.1 mrad is present.

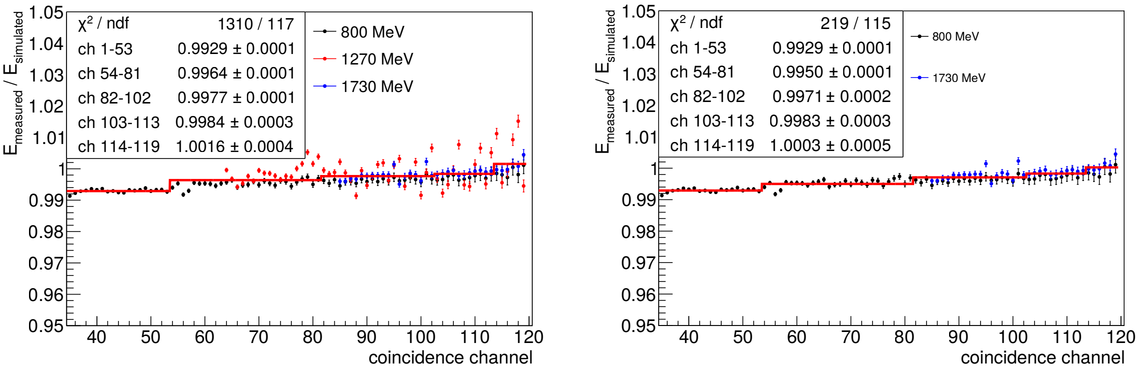

(a) Ratio of energy mean values of real to simulated data using the results from all three series of measurements.

(b) Ratio of energy mean values of real to simulated data without considering the results gained with a primary energy beam energy of 1270 GeV.

Figure 4.32: Energy mean value ratio of real to simulated data. Real data agrees with simulated data by better than 1%. The ratio approaches the value 1 for higher coincidence channels. Simulations show, that the deviation from 1 cannot be caused by beam and tagger hodoscope misalignments within the positioning precision.

A cross check is performed on the energy widths of each coincidence channel, which can be determined using the fit results as shown in figure 4.30b via:

$$\frac{\Delta E}{E_0} = E \cdot \frac{B_0}{E_0} \cdot \left(\frac{1}{B_{coinc} - \Delta B} - \frac{1}{B_{coinc} + \Delta B} \right). \tag{4.5}$$

Here, the fit parameter p_0 corresponds to B_{coinc} and p_1 corresponds to ΔB. The extracted energy widths per coincidence channel are shown in figure 4.33a in comparison with simulated data shown in figure 4.33b. It can be seen, that the extracted energy widths from real data are about 20% to 25% larger than the energy widths from simulated data. This deviation can be ascribed to two effects which are not included in the simulation. The hodoscope is closed with black foil to avoid light reaching the scintillators. Scattering processes on this foil are not considered. In addition, the primary electron beam carries a not yet understood background, which is probably generated at the extraction point and whose distribution in space is unknown. As mentioned in section 4.3.4, the design of the mechanical

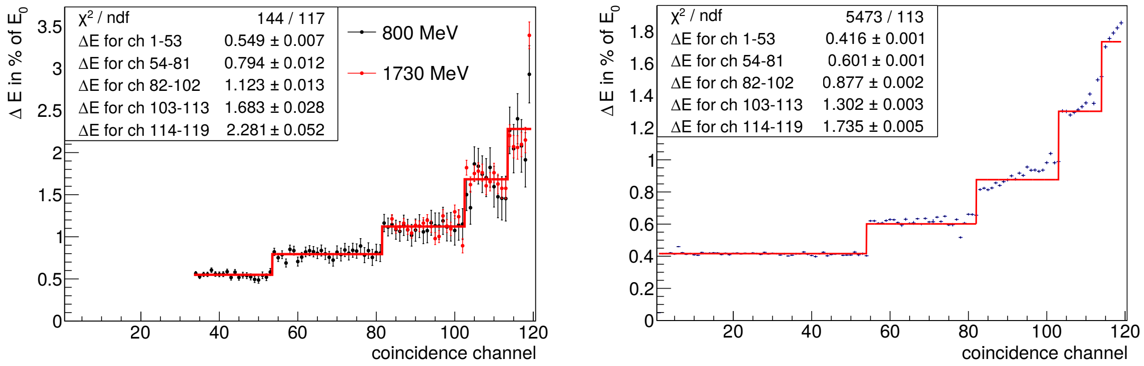

(a) Extracted energy widths for real data using a primary electron beam energy of 800 MeV and 1730 MeV.

(b) Extracted energy widths for simulated data.

Figure 4.33: Extracted energy width per coincidence channel for real and simulated data. The results from real data deviate between 20% and 25% from simulated data.

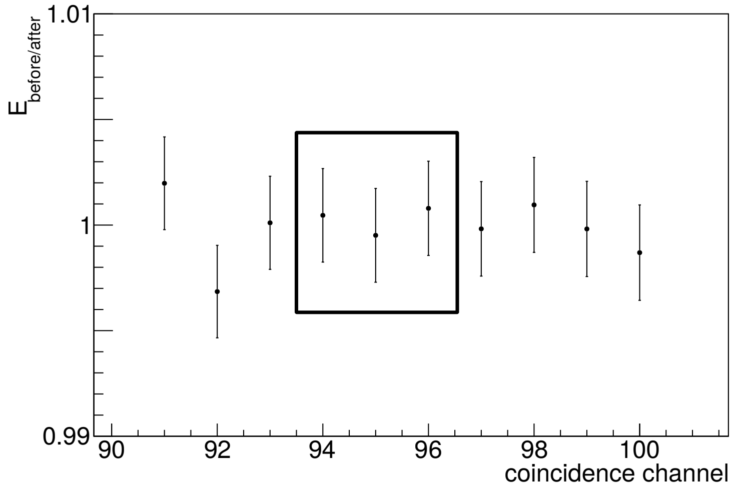

Figure 4.34: Ratio of energy mean values before and after removal of a scintillator slide. The black box indicates the channels which were removed and reinstalled.

structure of the vertical hodoscope shall allow maintenance on the scintillators without affecting the energy calibration. To proof the stability of the energy calibration under maintenance, one slide of scintillators (see section 4.3.4) is removed and reinstalled after the energy calibration. A further energy calibration is then performed in the region around the slide which was moved. Figure 4.34 shows the ratio of energy mean values per coincidence channel before and after the removal of the scintillator slide. The black box indicates the coincidence channels which includes the reinstalled scintillators. No significant change compared to untouched channels is observed. The variation is within the errors. Hence, the stability of the energy calibration is ensured.

CHAPTER 5

Production of linearly polarised photon beams at ELSA

Taking advantage of the coherent bremsstrahlung process off a crystal, linearly polarised photon beams can be produced. However, the crystal has to be aligned precisely with respect to primary electron beam momentum. The alignment mechanism of the crystal radiator using a goniometer system is explained in this chapter. Subsequently, the monitoring of the coherent bremsstrahlung spectrum and the determination of the expected degree of polarisation will be shown.

5.1 Crystal Alignment

We know from section 2.2.3, that a precise positioning of the diamond crystal with respect to the primary electron beam is essential to obtain a one-point coherent bremsstrahlung spectrum which leads to the highest expected degree of polarisation. A goniometer system which is introduced in section 3.1.3 fulfils the requirements on the accuracy of the alignment. In addition to the positioning accuracy of the goniometer, the knowledge of the angular offsets between the crystal and goniometer system as well as between the primary electron beam and the goniometer system are of significance. Since the angular offsets of the goniometer system to the primary electron beam direction depend on the stability of the primary electron beam, the offsets have to be determined on demand. An additional uncertainty which has to be corrected by the goniometer is a possible displacement during the installation of the crystal into the goniometer system. The method to determine these offsets used at the BGO-OD experiment is the *Stonehenge technique* developed by Ken Livingston [1] and already successfully used at the neighbouring CB-ELSA experiment, Jefferson Laboratory and the Mainzer Microtron. In the following, the diverse coordinate systems and their relation between each other are illustrated.

5.1.1 One-point spectra of coherent bremsstrahlung

For the ideal case, in which no offsets between the beam, goniometer and crystal coordinate systems exist, the angles α and θ introduced in section 2.2.3 are used to describe the production of one-point spectra of coherent bremsstrahlung and to determine the expected degree of polarisation. For simplicity reasons in the crystal alignment, new angles c, i and ϕ are introduced describing the relation between the primary electron beam and the crystal coordinate system shown in figure 5.1a.

- c: the main coherent peak corresponding to the [0,2,2] reciprocal lattice vector and its subsequent harmonics [0,4,4], [0,6,6] etc. can be set at any position in the bremsstrahlung spectrum. These peaks are controlled by the angle c between the electron beam and the [0,2,2] reciprocal lattice

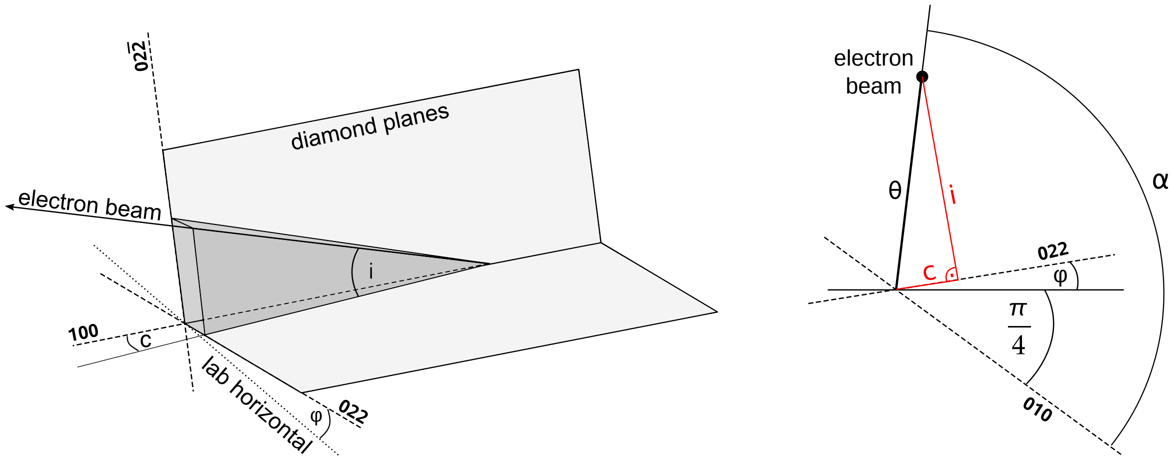

(a) Illustration of the scattering angles c, i and ϕ.

(b) Relation between the angles c, i and ϕ and the crystal angles θ, α and ϕ.

Figure 5.1: Definition of the scattering angles c, i and ϕ.

plane. For a diamond cut in [1,0,0] direction, the value of c can be determined via:

$$c \simeq \frac{m_e a}{4\sqrt{2}\pi h_k E_0^2 \left[\frac{1}{E} - \frac{1}{E_0}\right]} \tag{5.1}$$

m_e = electron mass in MeV
a = 923.7 diamond lattice constant
h_k = ±2, ±4, ... Miller indices
E_0 = primary electron beam energy in MeV
E = desired position of main coherent edge

- i: while c controls the main peak and its subsequent harmonics, the angle i between the electron beam and the [0,2,$\bar{2}$] affects the orthogonally contributing reciprocal lattice vectors. By choosing it larger than c ($i = 9 \cdot c$ at the BGO-OD experiment) the coherent contributions from the orthogonal planes are positioned to higher photon energies not being able to interfere destructively with the main coherent contribution of the [0,2,2].

- ϕ: the angle ϕ defines the position of the polarisation plane with respect to the horizontal in the laboratory frame.

To be able to determine the expected degree of polarisation, it is important to know the relation between (α, θ) and (c, i) which is shown in figure 5.1.

In general, angular offsets between the primary electron beam and the diamond exist. These offsets have to be determined and can be compensated by the goniometer system. In the following section, the offsets between the different coordinate systems are introduced.

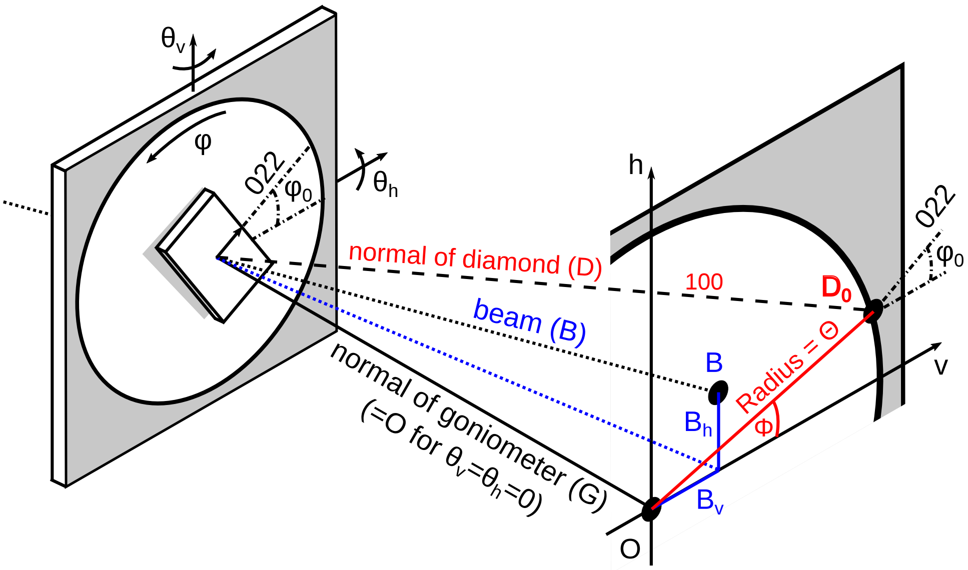

Figure 5.2: Angular offsets between primary electron beam (**B**), diamond (**D**) and goniometer (**G**) system.

5.1.2 Definition of angles and offsets

The goniometer system contains three motorised positioning units allowing rotations along all spacial axis (ϕ, θ_v, θ_h) as indicated in figure 5.2. For $\theta_v = \theta_h = 0$ the origin is defined by the normal of the goniometer system (G). All rotational axis of the goniometer system intersect in one-point in which the middle of the diamond radiator is installed. Due to a possible displacement of the diamond in the goniometer system, the direction of the reciprocal lattice vector [1,0,0] does not correspond to the goniometer normal. The offsets between the diamond and the goniometer system are considered as follows:

- ϕ_0: azimuthal offset between the direction of the [0,2,2] reciprocal lattice vector and the horizontal rotation axis θ_h.
- Θ: polar displacement between the origin and the direction of the [1,0,0] reciprocal lattice vector.
- Φ: azimuthal displacement between the horizontal rotation axis and the direction of the [1,0,0] reciprocal lattice vector.

Each experimental running period, the primary electron beam is aligned with respect to the experimental setup, but the primary electron beam direction does not fully fall close with the normal of the goniometer system. The offsets between the primary electron beam and the goniometer system are considered as follows:

- B_h: horizontal displacement between the origin and the primary electron beam.
- B_v: vertical displacement between the origin and the primary electron beam.

If all five offsets are known, the goniometer system can be used to move the diamond from its initial position D_0 into a position $D_{c,i,\phi}$ in which the angles c, i and ϕ engage their desired values with respect to the primary electron beam direction and therefore set the position of the main coherent peak in the bremsstrahlung spectrum. It can be seen in figure 5.3, that the relocation of the diamond takes place by applying the goniometer coordinates G_a, G_v and G_h on the goniometer's azimuthal, vertical and horizontal axis. First, the azimuthal coordinate G_a is applied to set the orientation ϕ of the polarisation

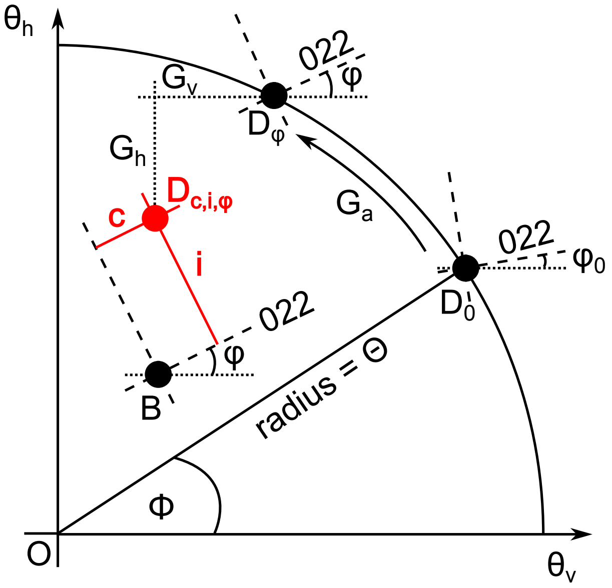

Figure 5.3: Required goniometer angles G_h, G_v and G_a to move the diamond radiator from D_0 to $D_{c,i,\phi}$

plane given by the [0,2,2] reciprocal lattice vector and therefore moving the [1,0,0] reciprocal lattice vector from D_0 to D_ϕ. Secondly, to bring the diamond from D_ϕ to position $D_{c,i,\phi}$ to set the angles c and i with respect to the primary electron beam direction, the goniometer's vertical and horizontal coordinates G_v and G_h are applied. By using trigonometry, the goniometer coordinates G_a, G_v and G_h are determined from figure 5.3 to:

$$G_a = \phi - \phi_0 \tag{5.2}$$

$$G_v = c\cos\phi - i\sin\phi - \Theta\cos(G_a + \Phi) + B_v \tag{5.3}$$

$$G_h = c\sin\phi + i\cos\phi - \Theta\sin(G_a + \Phi) + B_h \tag{5.4}$$

If needed, due to the four fold symmetry of the diamond around the [1,0,0] axis of the diamond, one can rotate the polarisation plane by $\pi/2$ by interchanging the values of c and i. Hence, the main coherent peak in the diamond bremsstrahlung spectrum is caused by the $[0,2,\bar{2}]$ reciprocal lattice vector.

It was shown that, applying the goniometer coordinates G_a, G_v and G_h leads to a one-point diamond bremsstrahlung spectrum with a main coherent peak caused by the [0,2,2] reciprocal lattice vector under an azimuthal angle ϕ with respect to the laboratory horizontal plane. Before G_a, G_v and G_h can be set, one has to determine the five angular offsets ϕ_0, Φ, Θ, B_v and B_h. The *Stonehenge technique* is used at the BGO-OD experiment to obtain the values of the angular offsets and will be presented in the following section.

5.1.3 Stonehenge

The *Stonehenge technique* uses the bremsstrahlung process of the diamond radiator itself to determine the angular offsets introduced before. In general, the position of the main peak in the bremsstrahlung spectrum is changed by systematic change of the goniometer coordinates G_v and G_h. The diamond is moved by the goniometer system such, that the [1,0,0] reciprocal lattice vector describes a cone of angular radius θ_r around an arbitrary origin S with respect to the origin of the goniometer system O:

$$G_v = S_v + \theta_r \cos\phi_r \tag{5.5}$$

$$G_h = S_h + \theta_r \sin\phi_r \tag{5.6}$$

where ϕ_r is increased from 0° to 360° in steps of 2°. For each set of G_v and G_h, a diamond bremsstrahlung spectrum is measured with the photon tagger. To enhance the coherent peaking in the bremsstrahlung spectrum, the diamond spectra are normalised with an amorphous copper bremsstrahlung spectrum. The normalised diamond bremsstrahlung spectra for ϕ_r between 0° and 360° are shown in figure 5.4a. The grey scale shows the relative intensity. The bright curves correspond to the coherent contributions of the [0,2,2] and [0,4,0] reciprocal lattice vectors moving through the kinematically allowed range of the bremsstrahlung process (see section 2.1). The strongest contribution is given by the [0,2,2] reciprocal lattice vectors. Figure 5.4b shows a normalised bremsstrahlung spectrum for the goniometer angle $\phi_r = 244°$. With increasing tagger channel index, the three contributing reciprocal lattice vectors (0,4,0), (0,2,$\bar{2}$) and (0,2,2) are visible. A *Stonehenge* plot, like it is shown in figure 5.5, is made by drawing the measured relative bremsstrahlung spectra shown in figure 5.4a radial in dependence of G_v and G_h. Either the coherent contributions of the [0,2,2] and the [0,4,0] reciprocal lattice vectors converge for $E_\gamma = 0$ at a given position defined by G_v and G_h. The coherent contributions will lie in the measured *Stonehenge* plot symmetrically around the convergence points. These convergence points indicate the position for which the reciprocal lattice vectors are perpendicular to the primary electron beam. Using the convergence points, the direction of the primary electron beam relative to the [1,0,0] reciprocal lattice vector is determined in the following way. Opposing convergence points of same reciprocal lattice vectors are connected with each other by two crossing orthogonal lines. In figure 5.5, the lines are indicated in red, where the thick lines connect the [0,2,2] reciprocal lattice vectors while the thin lines, rotated by 45° with respect to the thick lines, connect the [0,4,0] ones. The intersection point of those lines indicate the position of the primary electron beam direction with respect to the chosen origin S (see equations 5.5

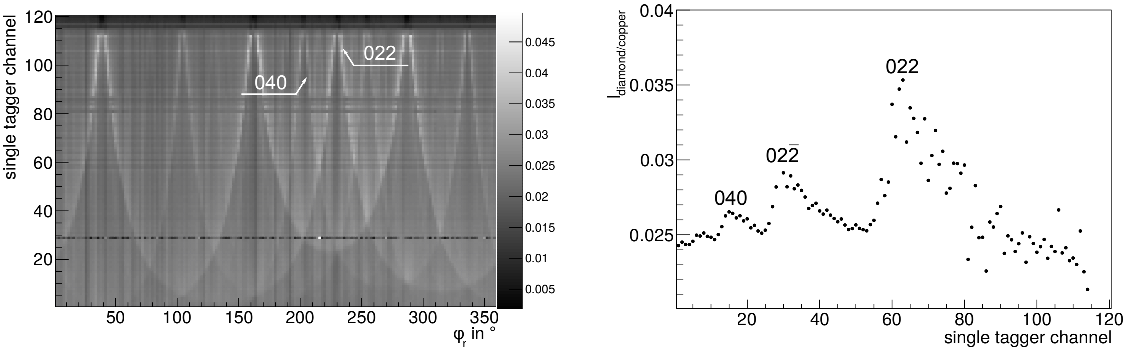

(a) Normalised bremsstrahlung spectrum as a function of the goniometer angle ϕ_r. Higher tagger channel corresponds to higher electron energies. The gray code gives the relative intensity. The bright lines indicate the coherent contributions of different reciprocal lattice vectors. Channel 29 had a malfunction during the *Stonehenge* scan.

(b) Normalised bremsstrahlung spectrum for the goniometer angle $\phi_r = 244°$. With increasing tagger channel index, the three contributing reciprocal lattice vectors (0,4,0), (0,2,$\bar{2}$) and (0,2,2) are visible.

Figure 5.4: *Stonehenge* scan on an uncalibrated diamond radiator. A conus with an opening angle of 60 mrad was scanned with 180 steps, each 2° large. Each measured diamond bremsstrahlung spectrum is normalised with an amorphous bremsstrahlung spectrum to enhance the coherent contributions.

and 5.6). The azimuthal offset ϕ_0 is given through the angle between the thick connection lines with respect to the goniometer axis G_v and G_h. ϕ_0 ranges between 0° and 90°, due to the four-folded symmetry of the diamond. The vector between the [1,0,0] reciprocal lattice vector and the direction of the primary electron beam is determined by $\overrightarrow{BD_0} = -(\vec{S} + \overrightarrow{SB})$. During the first performance of a *Stonhenge* scan, the origin S is set to $S_v = S_h = 0$. The displacement $\overrightarrow{BD_0}$ is compensated and the measured azimuthal offset ϕ_0 is set to 45° with the goniometer system. A cross check of the determined angular offsets is performed with an additional *Stonhenge* scan shown in figure 5.6. It is visible that the crystal is now aligned with respect to the primary electron beam direction and the thick red connecting lines take an angle of 45° with the goniometer axis G_v and G_h. To determine the remaining angular offsets B_v, B_h, Θ and Φ, which indicate the displacement of the crystal relative to the goniometer system, a second *Stonehenge* scan at a known azimuthal position ϕ_s with respect to the position of D_0 has to be performed (see figure 5.7). From the second *Stonhenge* scan one obtains another vector $\overrightarrow{BD_1} = (\theta_{v1}, \theta_{h1})$ being different from $\overrightarrow{BD_0} = (\theta_{v0}, \theta_{h0})$. Using $\overrightarrow{BD_0}$ and $\overrightarrow{BD_1}$ the remaining offsets can be determined via:

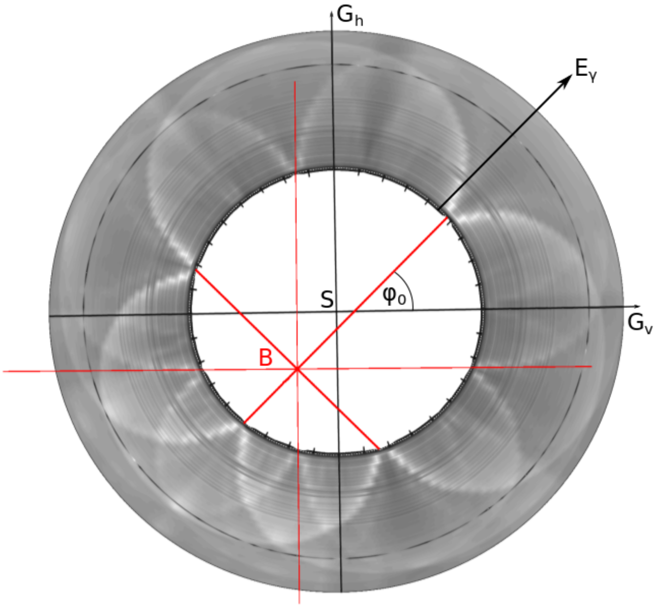

Figure 5.5: *Stonehenge* plot achieved by connecting both ends of figure 5.4. Red lines connect convergence points of [0,2,2] and [0,4,0] reciprocal lattice vectors. Intersection point of red lines defines primary electron beam position on the crystal.

$$B_v = -\left[\frac{\theta_{v0} + \theta_{v1}}{2} - \frac{\theta_{h1} - \theta_{h0}}{2\tan\left(\frac{\phi_s}{2}\right)}\right] \tag{5.7}$$

$$B_h = -\left[\frac{\theta_{h0} + \theta_{h1}}{2} + \frac{\theta_{v1} - \theta_{v0}}{2\tan\left(\frac{\phi_s}{2}\right)}\right] \tag{5.8}$$

$$\Phi = \arctan\left(\frac{B_h + \theta_{h0}}{B_v + \theta_{v0}}\right) \tag{5.9}$$

$$\Theta = \sqrt{(B_v + \theta_{v0})^2 + (B_h + \theta_{h0})^2} \tag{5.10}$$

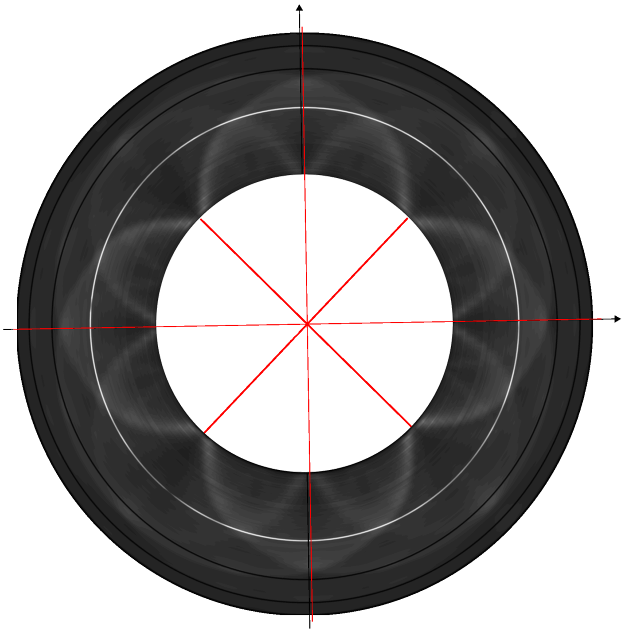

Figure 5.6: *Stonehenge* plot of a calibrated diamond radiator. The two black and the white circle originate from malfunctioning tagger channels.

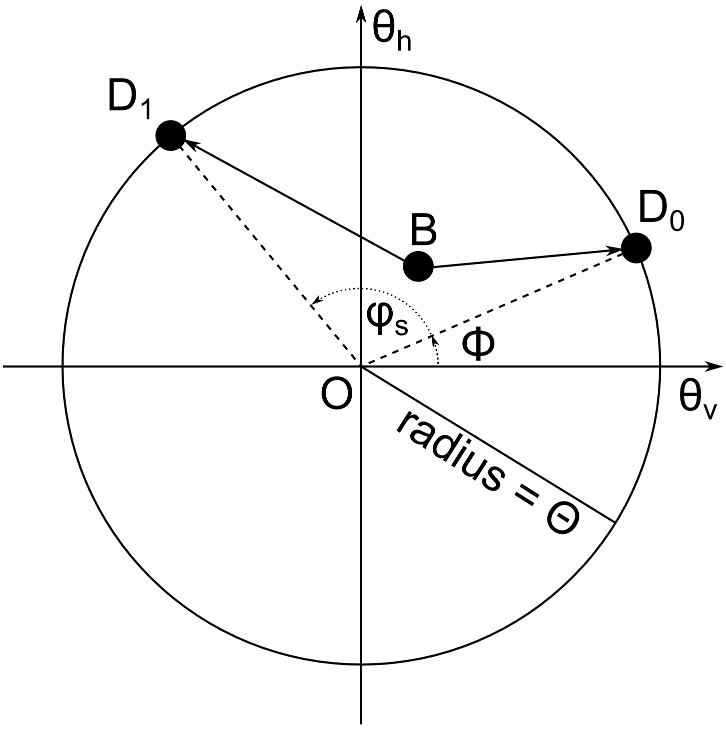

Figure 5.7: Determination of angular offsets B_v, B_h, Θ and Φ.

After all angular offsets are determined, the goniometer rotates the crystal to the correct position in order to get a one-point coherent bremsstrahlung spectrum. The main coherent peak caused by the [0,2,2] reciprocal lattice vector can be set at any bremsstrahlung photon energies.

5.1.4 Polarisation Planes

Within this thesis, the photon beam asymmetry Σ (see chapter 1) is determined in π^0 photo-production off the proton, to perform a cross check on the analytical determination of the expected degree of linear polarisation (section 5.2). The azimuthal dependence on the detection efficiency $\epsilon(\phi)$ of the experimental setup can be removed in the measurement of the photon beam asymmetry Σ by performing the experiment with two different polarisation planes. An azimuthal orientation of the polarisation planes with 90° between each other is required. Due to a larger horizontal electron beam divergence, the optimal azimuthal orientation of the polarisation planes is ±45° [51]. It is shown in section 2.2.4, that the electron beam divergence smears out the shape of the coherent contribution and consequently lowers the expected degree of polarisation. Hence, is has to be assured, that the coherent bremsstrahlung spectra have the same shape for both polarisation planes. Figure 5.8 shows the comparison of the normalised diamond bremsstrahlung spectra for both polarisation planes. The bremsstrahlung spectra look generally the same. A relative deviation of $\sim 2.5\%$ of the relative intensity between both polarisation planes is present in the energy range between 1800 MeV and 2100 MeV. This deviation can be related to the extraction of the primary electron beam discussed in section 5.1.5.

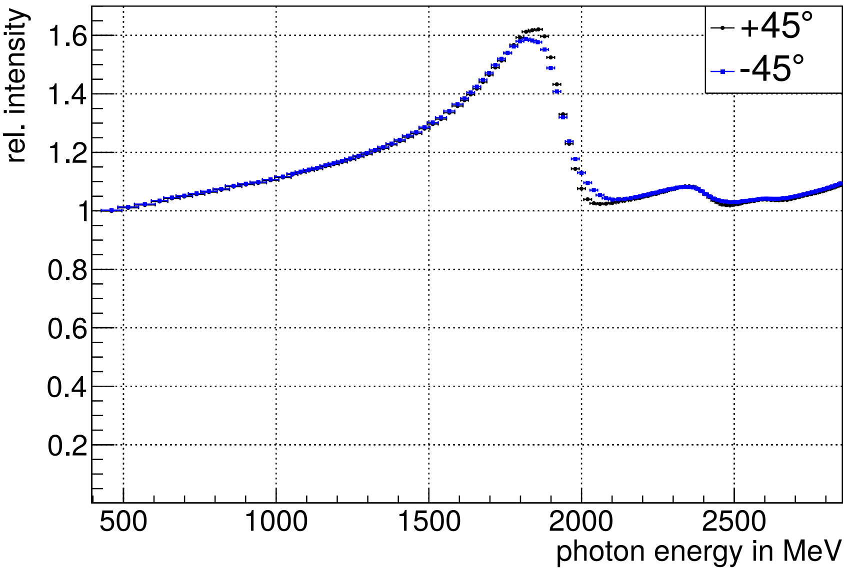

Figure 5.8: Normalised diamond bremsstrahlung spectra for azimuthal orientations of ±45°.

By setting the orientation of the polarisation planes to ±45°, the $\cos 2\phi$ modulation of the differential cross section (section 1) will change into a $\sin 2\phi$ modulation. The measured normalised distributions

$\tilde{N}(\phi_\gamma, E_\gamma, \theta, \phi)$ of the photoproduced meson for both polarisation planes are given through

$$\begin{aligned}
\tilde{N}(\phi_\gamma = +45^\circ, E_\gamma, \theta, \phi) &= \tilde{N}(\phi_\gamma = +45^\circ, E_\gamma, \theta)\epsilon(\phi)[1 - P_{\gamma,l}(E_\gamma)\Sigma(E_\gamma, \theta)\cos(2(\phi + 45^\circ))] \\
&= \tilde{N}(\phi_\gamma = +45^\circ, E_\gamma, \theta)\epsilon(\phi)[1 + P_{\gamma,l}(E_\gamma)\Sigma(E_\gamma, \theta)\sin(2\phi)] \qquad (5.11) \\
\tilde{N}(\phi_\gamma = -45^\circ, E_\gamma, \theta, \phi) &= \tilde{N}(\phi_\gamma = -45^\circ, E_\gamma, \theta)\epsilon(\phi)[1 - P_{\gamma,l}(E_\gamma)\Sigma(E_\gamma, \theta)\cos(2(\phi - 45^\circ))] \\
&= \tilde{N}(\phi_\gamma = +45^\circ, E_\gamma, \theta)\epsilon(\phi)[1 - P_{\gamma,l}(E_\gamma)\Sigma(E_\gamma, \theta)\sin(2\phi)], \qquad (5.12)
\end{aligned}$$

with ϕ_γ being the azimuthal orientation of the polarisation plane, the produced bremsstrahlung photon energy E_γ, the polar angle θ of the emitted meson in the centre of mass frame and the azimuthal emission angle ϕ. The angular photoproduced meson distributions can be combined such, that the detection efficiency cancels out through

$$\frac{\tilde{N}(\phi_\gamma = +45^\circ, E_\gamma, \theta, \phi) - \tilde{N}(\phi_\gamma = -45^\circ, E_\gamma, \theta, \phi)}{\tilde{N}(\phi_\gamma = +45^\circ, E_\gamma, \theta, \phi) + \tilde{N}(\phi_\gamma = -45^\circ, E_\gamma, \theta, \phi)} = P_{\gamma,l}(E_\gamma)\Sigma(E_\gamma, \theta)\sin(2\phi). \qquad (5.13)$$

5.1.5 Monitoring of the relative diamond bremsstrahlung spectra

The position of the coherent edge in the diamond bremsstrahlung spectrum is set using equation 5.1. During longer data taking periods a displacement of the primary electron beam may occur, changing the position of the coherent edge in the bremsstrahlung spectrum. Hence, the bremsstrahlung spectrum is monitored to be able to react on such variations. For the monitoring, the diamond bremsstrahlung spectrum is used by itself and observed with a frequency of 20 Hz simultaneously to the data taking. To gain enough statistics, the scaler information of the coincidence channels of the tagger hodoscope is used. Each bremsstrahlung spectrum is normalised by a reference copper bremsstrahlung spectrum which is recorded every eighth hours.

An example of the normalised spectrum is given in figure 5.9a. The distribution of the normalised spectrum in the region of the main peak is fitted by the empiric function

$$f(x) = pol(0) + (1 - Erf((x - p_0)/p_1)) \cdot pol(3). \qquad (5.14)$$

were p_0 indicates the position of the main peak in the bremsstrahlung spectrum, p_1 the width of the error function and $pol(2)$ and $pol(3)$ are polynomials of zeroth and third order. During the data taking the normalised spectrum and its fit (as figure 5.9a) are visualised online to monitor the stability of the coherent main peak's position. The extracted position of the coherent edge is also plotted on a time axis, as illustrated in figure 5.9b. Shown is the position of the coherent edge in the bremsstrahlung spectrum, localised at around 1950 MeV for both polarisation planes which were introduced in section 5.1.4. The hole in between 11:37 and 11:38 corresponds to the time were the diamond was rotated from one polarisation plane to the other. In addition, several thinner holes are visible, corresponding to the spill wise extraction of the primary electron beam. The monitoring of the position of the coherent edge is kept under control also within the spill (figure 5.10).

By looking at the position of the coherent edge during the extraction time, it is visible that the position of the coherent edge is very unstable in the first second of the primary electron beam extraction. At the beginning of each spill, the position of the coherent edge is off by about 50 MeV and moves rapidly to the desired value. From chapter 2 it is known that a displacement of the coherent edge is caused by an angular displacement of the primary electron beam on the crystal. Using the formulae introduced in chapter 2 an angular change of ~0.1 mrad is expected to shift the coherent edge by 50 MeV. An angular shift of the primary electron beam of ~0.1 mrad was already assumed in section 4.4.4 to explain the

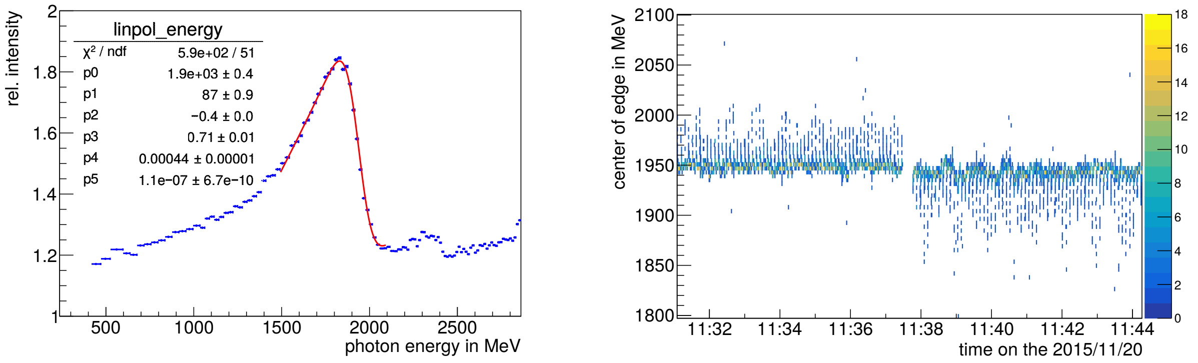

(a) Normalised diamond spectrum fitted by equation 5.14.

(b) From equation 5.14 extracted position of the coherent edge as a function of time during data taking. The colour code gives the number of entries.

Figure 5.9: Online monitoring of the position of the coherent contribution of the (0,2,2) reciprocal lattice vector.

deviation of the measured energy mean values compared to simulated data. During the remaining four seconds in the spill, the position of the coherent edge changes by about 10 MeV.

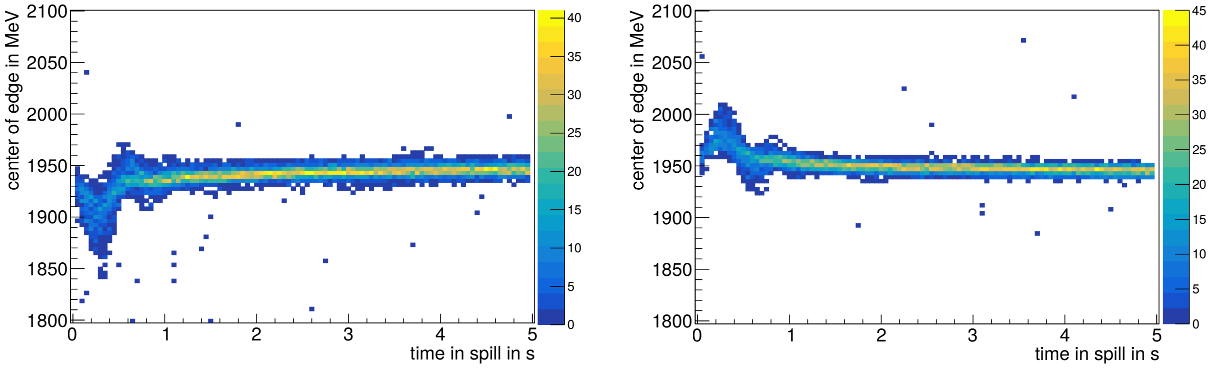

(a) Position of coherent edge for positive polarisation plane.

(b) Position of coherent edge for negative polarisation plane.

Figure 5.10: Fitted position of the coherent edge according to equation 5.14 as a function of time during spill. The colour code gives the number of entries. In the first second of each spill the position of the coherent edge is very unstable.

5.2 Determination of the degree of polarisation

For the determination of the degree of polarisation, diamond bremsstrahlung spectra taken with the general data trigger conditions introduced in chapter 3 are analysed. In order to not get biased by any trigger and making use of the large gate of 2 μs for data acquisition, only events not correlated to the trigger timing are considered. The diamond bremsstrahlung spectra are normalised with amorphous bremsstrahlung spectra and compared to analytical calculations performed with the program CORBIS[1] [2] which is mainly based on the formulae introduced in chapter 2. In the calculation of the

---

[1] **C**alculation **O**f **R**elative **B**remsstrahlung **I**ntensity **S**pectra

bremsstrahlung spectra, experimental effects such as primary electron beam divergence, primary electron beam spot size and multiple scattering in the radiator are simulated by Gaussian distributions. The input parameters required for the production of a calculated diamond bremsstrahlung spectrum are listed in table 5.1. Since the incoherent contribution is underestimated by the calculations, an incoherent scaling factor of ~1.18 has to be introduced. An additional scaling factor for the incoherent contribution is also required at the CB/ELSA, MAMI A2 and CLAS experiments, which lies between 1.3 and 1.5. Figure 5.11 shows the comparison of an uncollimated relative diamond bremsstrahlung spectrum with the prediction of COBRIS together with the expected degree of polarisation.

Electron beam	Radiator	Collimator	Other
Energy in MeV Divergence$_{hor}$ in mrad Divergence$_{ver}$ in mrad Spot size$_{hor}$ in mm Spot size$_{ver}$ in mm	Proton nr$_{cry}$ Proton nr$_{amo}$ Thickness in μm Temperature in K Lattice vectors c in mrad i in mrad ϕ in degree	Diameter in mm Length in cm Distance to radiator in m	Incoherent scaling

Table 5.1: Input parameters for COBRIS.

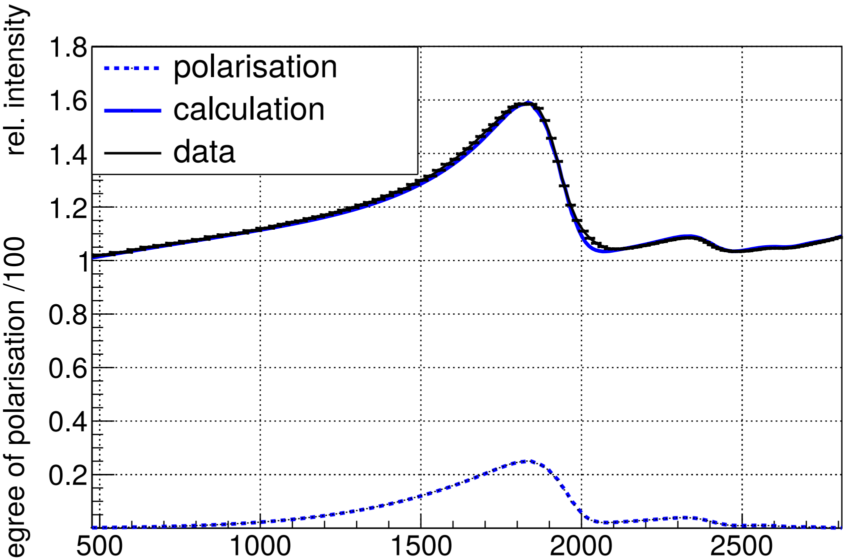

Figure 5.11: Relative uncollimated diamond bremsstrahlung spectrum in black compared to calculations performed with COBRIS in blue. The dashed blue line indicates the expected degree of polarisation.

By collimating the produced bremsstrahlung photon beam, the incoherent contribution in the diamond bremsstrahlung spectrum can be reduced and according to equation 2.45 the degree of polarisation increased. Requiring a temporal coincidence between the tagger hodoscope and the FluMo detector, a collimated bremsstrahlung spectrum is achieved. Figure 5.12 shows a measured uncollimated and collimated relative diamond bremsstrahlung spectrum compared with the predictions of COBRIS. The collimation of the photon beam results in an enhancement of the relative intensity of almost 25%. Hence, the expected maximum degree of polarisation increased by ~6% absolute. To determine the error of the expected degree of polarisation a fitting routine which describes the relative diamond bremsstrahlung spectra is implemented in COBRIS using the TF1 class of root[2]. The variable parameters used by the fit function are listed in table 5.2. After fitting a relative bremsstrahlung spectrum, the expected degree of polarisation is calculated within the errors of the parameters given by the fitting procedure. A band for the expected degree of polarisation can be calculated. Figure 5.13 shows a fitted relative diamond bremsstrahlung spectrum. Here, p_0 corresponds to the angle i affecting the orthogonally contributing reciprocal lattice vectors at higher photon energies, p_1 to the angle c which defines the position of the coherent edge and p_2 to the angle ϕ which defines the polarisation plane. The values of p_0 and p_1 are given in mrad, while p_2 is given in degrees. Parameters p_3 and p_4 corresponds to the horizontal and vertical beam divergence given in mrad. Since both act the same, only one parameter is varied. P_5 is the incoherent scaling factor which has the largest uncertainty. The parameters for which the error is 0 are not free in the fit. The calculated expected degree of polarisation within the errorband coming from the errors of the fit is shown in figure 5.13. A relative uncertainty in the expected degree of polarisation of ~1% is determined from the fit.

Electron beam	Radiator	Other
Divergence$_{hor}$ in mrad Divergence$_{ver}$ in mrad	c in mrad i in mrad ϕ in degree	Incoherent scaling

Table 5.2: Input parameters of the fitting routine.

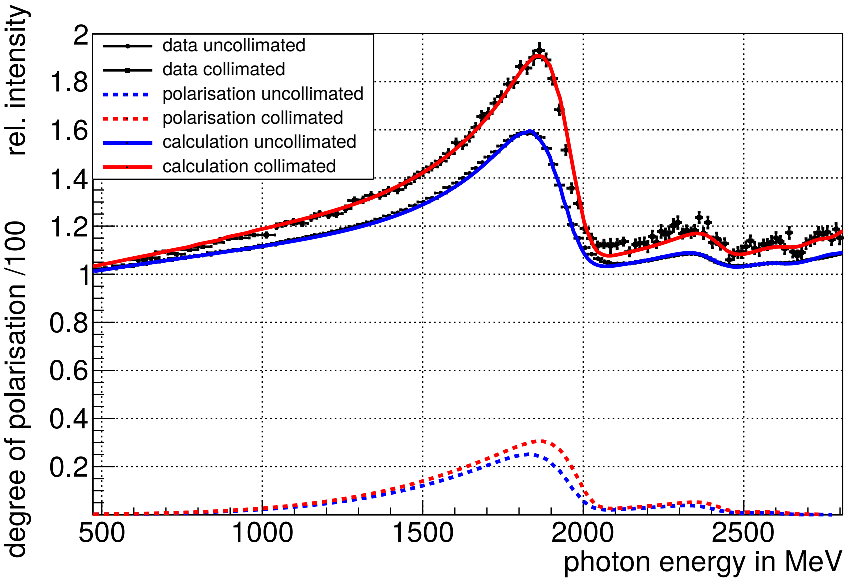

Figure 5.12: Relative uncollimated and collimated diamond bremsstrahlung spectra compared to calculations performed with COBRIS. The dashed lines show the corresponding expected degree of polarisation. By collimating the produced bremsstrahlung photon beam, the degree of polarisation can be significantly increased.

---

[2] https://root.cern.ch/

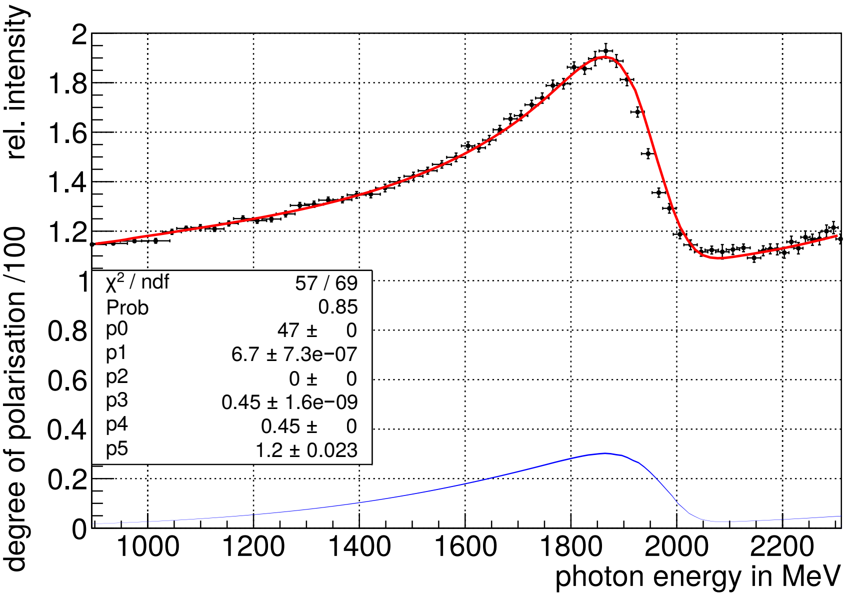

Figure 5.13: Determination of the error on the expected degree of polarisation. The relative collimated diamond bremsstrahlung spectrum is fitted for varied parameters being the scattering angle i, the horizontal beam divergence and the incoherent scaling factor. The blue band indicates the calculated polarisation band within the errors of the varied parameters from the fit. A relative uncertainty of the expected degree of polarisation of ±1% is determined.

The expected degree of polarisation can be verified by measuring and comparing the photon beam asymmetry Σ for example in π^0 meson photo-production, for which very precise results already exits. A comparison of the measured photon beam asymmetry Σ is shown in the following chapter.

CHAPTER 6

First extraction of the photon beam asymmetry at the BGO-OD experiment

At the BGO-OD experiment, a linearly polarised photon beam is produced via coherent bremsstrahlung. The degree of polarisation of the photon beam is not measured directly. Instead, it is determined analytically (see chapter 5.2). A further goal of this thesis is to perform a cross check on the determined degree of polarisation. This is done through the extraction of the already well measured photon beam asymmetry Σ in π^0 photo-production off the proton using linearly polarised photons. Since the dominant decay mode of the η is equivalent to the one of the π^0, the photon beam asymmetry is also extracted in η photo-production. Even if the smaller cross section in the η channel do not allow the extraction of the photon beam asymmetry with the same precision as in the π^0 channel, it is interesting to see if the extracted photon beam asymmetry is consistent also in the η channel. In this chapter are presented the various steps of the data analysis and the results of the extracted photon beam asymmetry Σ in π^0 and η photo-production off the proton compared to calculations of the BnGn [3] parametrisation and to already existing precise data.

6.1 Detector calibration

The data taken with the experimental setup introduced in chapter 3 consists mainly of ADC and TDC values. This kind of data is converted into physical quantities like energy and time information by performing appropriate calibrations. In the following the calibration methods of the various detectors are introduced.

6.1.1 Time calibration

Two different kinds of TDC are in use at BGO-OD, which require different calibration procedures. A commercial CAEN CV 1290 TDC used for MOMO is calibrated through the relation

$$t = mx + b, \tag{6.1}$$

where $x \in \mathbb{N}$ denotes the TDC bin, $m \in \mathbb{R}$ is the width of each TDC bin in ps, being equal to 97.65625 ps for this model, b is the offset which originates e.g. from cable lengths or light propagation in the detector material.

For the remaining detectors, the same TDC as for the photon tagger is used (see section 4.2). With a clock of 200 MHz, the TDC samples the input signal with the tapped delay method. The taps are not equidistant. The inter-tap time distances are calibrated through a complicated procedure explained in [50]. Together with the clock cycle and the inter-tap time distances, the width of the TDC channels is obtained. Also for this TDC, the time information is affected by a channel dependent offset. The offset is determined on software level. For each detector channel, the time difference with respect to the trigger time is determined. The time difference distribution is fitted with a Gaussian function. Subsequently, the time of each detector channel is corrected by the mean of the Gaussian fit.

The BGO calorimeter is the only detector for which a time calibration is not necessary. It is equipped with a Wiener AVM 16 sampling ADC which already provides the time information in ns through feature extraction [52]. In this case the time defined by the sampling is further improved by reconstructing the intersection point between the leading edge of the signal and its baseline.

6.1.2 Gain matching and energy calibration of the BGO calorimeter

The gain matching and the energy calibration of the BGO calorimeter is performed with ^{22}Na sources. ^{22}Na decays with a probability of ~89% via β^+ decay. The e^+ annihilates within the radioactive source and therefore two photons with an energy of 0.511 MeV are produced. The β^+ decay is followed immediately after ~3 ps by a γ decay with an energy of 1.27 MeV. For each signal, the sampling ADC is able to perform feature extraction [52] on the sampled pulse. It looks for the baseline and subtract it automatically from the pulse. Figure 6.1 shows in logarithmic scale the measured ADC spectrum of one BGO crystal using a ^{22}Na source. The measured ADC spectrum is fitted with the sum of an exponential background, an approximation for the Compton edge and two Gaussian functions, which describe the 0.511 MeV photon contribution through $e^+ + e^-$ annihilation and the 1.27 MeV γ decay photons. The HV of photomultipliers are adjusted such that the photon peak is located for all bgo crystals at ADC channel 400±20. Since the baseline is already subtracted from the ADC spectrum, the decay photon peak position corresponds to 1.27 MeV.

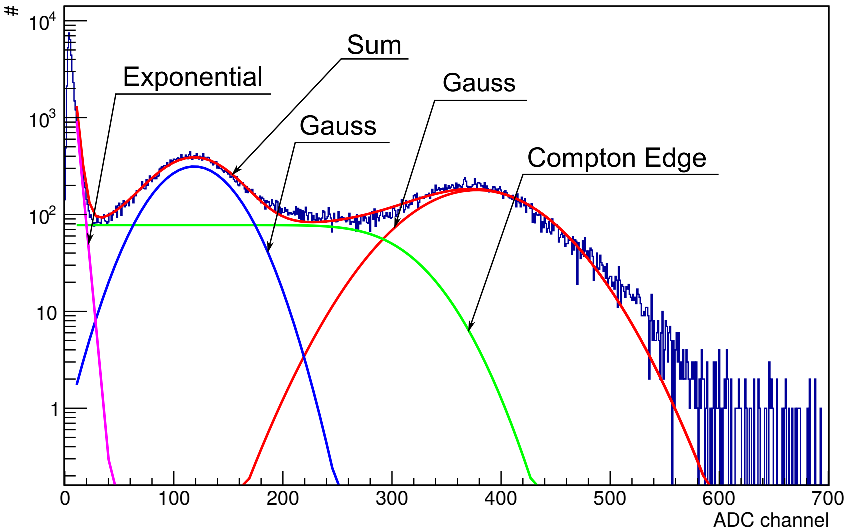

Figure 6.1: ADC channel spectrum for one BGO crystal in logarithmic scale. The 0.511 MeV and 1.27 MeV photons of the ^{22}Na source were measured and fitted with a Gaussian function. In addition, an exponential background and a Compton edge approximation were considered in the fit.

6.2 Data analysis

The analysis is performed on the data set acquired during the June/July 2015 beam time. It was optimised for the analysis of the photon beam asymmetry in η' photo-production near threshold. Hence, the diamond radiator was aligned such that the coherent edge was located at a bremsstrahlung photon energy of around 1620 MeV. The maximum degree of polarisation of about 28.5% was expected at a bremsstrahlung photon energy of around 1530 MeV with a primary electron beam energy of 2900 MeV. Data was acquired for two perpendicularly orientated polarisation planes with azimuthal angles of ±45° with respect to the vertical axis. During this beam time the three photomultipliers of the tagger hodoscope located closest to the primary electron beam were turned off due to saturation. In this section, constraints which were set on the data samples are illustrated on the data set taken with the negatively orientated polarisation plane.

6.2.1 Cluster reconstruction and their interpretation in terms of neutral and charged particles

The calibrated detector signals are used to reconstruct four momenta of photons or charged particles. To do so, the information of the energy deposition and the detection position in the detector is required.

A photon deposits its energy through the development of an electromagnetic shower over several adjacent BGO crystals. These adjacent crystals form a cluster. The sum of the deposited energies of each crystal containing in the cluster corresponds to the energy of the detected photon. It is possible that two photons are detected close to each other, which results in overlapping clusters. A standard cluster algorithm named *Local Maxima Clustering* is used to reconstruct the clusters, and if necessary, to disentangle overlapping ones [45].

First, it is searched for the crystal with the largest energy deposition. Subsequently, adjacent crystals are added. If two crystals in a cluster are geometrically separated by at least one crystal with a lower energy deposition, the cluster algorithm splits this cluster into two separate ones. Statistical fluctuations in the energy deposition can occur at the edge of a cluster, resulting in the reconstruction of multiple clusters. To reduce this effect, only crystals with at least 1.5 MeV deposit energy are used in the cluster reconstruction. Once all clusters are reconstructed, the cluster algorithm discriminates the ones with an energy smaller than 25 MeV to reduce background coming from low energetic particles. The position of the reconstructed clusters or equivalently of the detected photons is determined by the energy weighted sum of the crystal positions within the detector with respect to the centre of the target

$$\vec{x}_\gamma = \frac{\sum_{i=0}^{N} \cdot \vec{x}_i \cdot \sqrt{E_{i,dep}}}{\sum_{i=0}^{N} \cdot \sqrt{E_{i,dep}}} \tag{6.2}$$

Detected clusters are treated as a photon, if no temporal and spacial coincidence with hits in the scintillator barrel is observed. On the contrary, if a hit in the scintillator barrel is found in geometrical and time correlation with a cluster in the BGO, the cluster is ascribed to the passage of a charged particle (e.g. protons, charged pions or kaons). Compared to photons and electrons, heavy charged particles like protons, charged pion or kaons do not lose their energy through an electromagnetic shower. In general, they are detected within 1 or 2 crystals. As an example, protons with kinetic energies up to 500 MeV are stopped inside the BGO. Protons with higher kinetic energies punch through the crystals instead. The resolution of their reconstructed position is then dominated by the granularity of the BGO calorimeter.

Since the forward angles from 10° to 25° are only covered by SciRi, a coincidence with a second detector can not be required. Hence, any particle seen by SciRi is treated as charged.

6.2.2 Event reconstruction

The hadronic reactions of interest in this analysis are $\gamma + \mathrm{p} \rightarrow \mathrm{p} + \pi^0 \rightarrow \mathrm{p} + \gamma\gamma$ and $\gamma + \mathrm{p} \rightarrow \mathrm{p} + \eta \rightarrow \mathrm{p} + \gamma\gamma$. In both cases two photons and at least one proton in the final state are required for the identification of the hadronic reaction. Possible meson candidates are obtained by determining the invariant mass from the measured four momenta of the two decay photons

$$m_{meson} = \sqrt{\left(\sum_{i=1}^{2} E_{i,\gamma}\right)^2 - \left(\sum_{i=1}^{2} \vec{p}_{i,\gamma}\right)^2} \,. \tag{6.3}$$

The invariant mass of two photons is determined under the condition, that both decay photons are seen within 10 ns. The corresponding time cut is shown in figure 6.2a. Figure 6.2b shows the invariant 2γ mass spectrum obtained from the measured four momenta of the photons. Two peaks are visible at 140 MeV and 580 MeV. The peak at lower energies is close to the π^0 mass of 135 MeV, while the position of the second peak is located at the η meson mass being off by 32 MeV. The main effect for the offsets in mass is a shifted target by ~1.6 cm downstream with respect to the bremsstrahlung photon beam. This offset leads to differently measured polar angles and therefore a change in the invariant mass of the 2γ system. The effect of the shifted target will be visible in further shown plots of different kinematical variables.

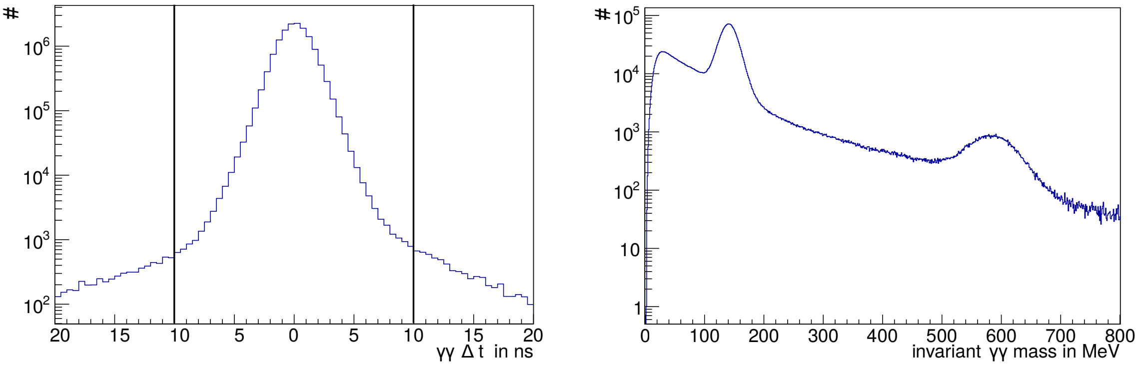

(a) Time difference spectrum of the 2 decay photons in logarithmic scale. The black vertical lines indicate the applied condition.

(b) 2γ invariant mass spectrum in logarithmic scale.

Figure 6.2: 2γ invariant mass spectrum obtained after applied time cut.

6.2.3 Event selection

The energy of the incoming bremsstrahlung photon is used to apply kinematical conditions. However, it happens that more than one bremsstrahlung electron is detected in the tagger hodoscope within one trigger event. Therefore it is necessary to select the proper post-bremsstrahlung electron corresponding to the produced bremsstrahlung photon which caused the hadronic reaction. The prompt peak, which corresponds to the post-bremsstrahlung electrons that caused the trigger, can be isolated from the 2 ns bunch structure of the extracted primary electron beam (see section 4.4.3). Selecting the events which lie by ±1.5 ns around the prompt peak show a multiplicity of one post-bremsstrahlung electron in 93.5% of the selected events.

Proper hadronic events can be selected through combinatorics and four-momentum conservation

$$\begin{pmatrix} E_\gamma \\ \vec{p}_\gamma \end{pmatrix}_{beam} + \begin{pmatrix} m_p \\ \vec{0}_p \end{pmatrix}_{target} = \begin{pmatrix} E_p \\ \vec{p}_p \end{pmatrix} + \begin{pmatrix} E_m \\ \vec{p}_m \end{pmatrix} \tag{6.4}$$

The first term in equation 6.4 is the four momentum of the incoming bremsstrahlung photon, with the energy measured by the photon tagger and the momentum along z. The second term corresponds to the target proton at rest. On the right side are written the four momenta of the outgoing proton and the photoproduced meson.

First, hadronic events with wrongly assigned tagged bremsstrahlung electrons are rejected. The three photomultipliers of the tagger hodoscope located closest to the primary electron beam were turned off due to saturation. Hence, bremsstrahlung photons with energies up to 470 MeV were not tagged. These photons can cause the trigger in the BGO calorimeter with an arbitrary simultaneously detected electron in the photon tagger. Photons with an energy of ~340 MeV preferentially excite the $\Delta^+(1232)$ resonance which decays into $p\pi^0$ and $n\pi^+$. Since such bremsstrahlung photons are not tagged, it is expected that such trigger events occur often. This is checked by solving equation 6.4 in dependence of the photon energy

$$E_{\gamma,calc} = \frac{m_p E_m + \frac{1}{2}\left(E_m^2 - \vec{p}_m^{\,2}\right)}{m_p - E_m + p_{m,z}}. \tag{6.5}$$

Here, the nominal mass of the proton is used. Figure 6.3a shows the calculated tagger photon energy versus the measured ones. One can see, that many untagged reactions with bremsstrahlung photon energies of ~340 MeV occurred. These reactions are assigned to wrong photon energies and will disturb in the further analysis of the photon beam asymmetry at higher photon energies. Hence, a linear cut is applied on the tagged photon energies which is shown in figure 6.3b. After cleaning the events from untagged reactions, events for which the corresponding bremsstrahlung photon energy is between 950 MeV and 1700 MeV, respectively around the coherent edge, were kept.

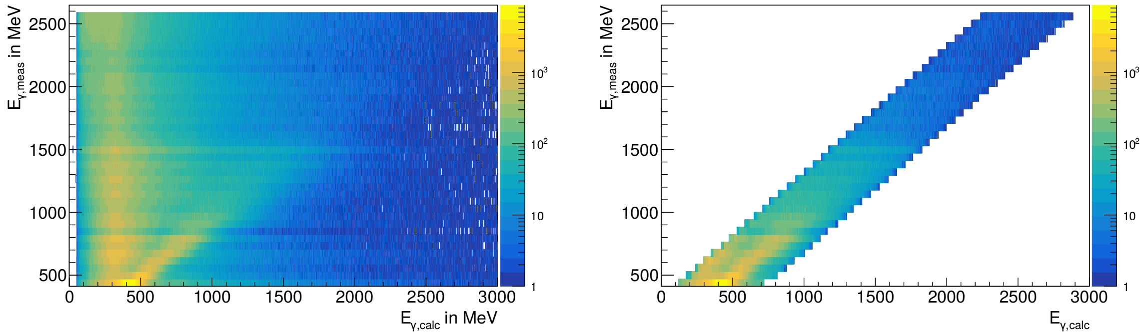

(a) The diagonal band corresponds to events, for which measured and calculated bremsstrahlung photon energy is equivalent. A vertical band is visible at a calculated energy of ~340 MeV. These events correspond to untagged bremsstrahlung photons, which excited a $\Delta^+(1232)$ resonance.

(b) A linear cut was applied to the bremsstrahlung photon energy to mainly remove untagged reactions and events for which the outgoing baryon does not correspond to a proton.

Figure 6.3: Measured versus calculated bremsstrahlung photon energy. The colour code denotes the number of entries in logarithmic scale.

At this level of the analysis the multiplicity of the detected tagger electrons may still be larger than one. In this case, the missing proton mass is determined with the four momenta of the bremsstrahlung photon and the detected meson candidate via

$$m_{p,miss} = \sqrt{\left(E_\gamma + m_p - E_m\right)^2 - \left(\vec{p}_\gamma - \vec{p}_m\right)^2}. \tag{6.6}$$

The tagged bremsstrahlung photon for which the missing mass deviates less from the nominal proton mass is kept. Figure 6.4 shows the missing mass plotted against the 2γ invariant mass for the best matching tagger photon. Two peaks at the π^0 and η mass are visible correlated with the missing proton mass.

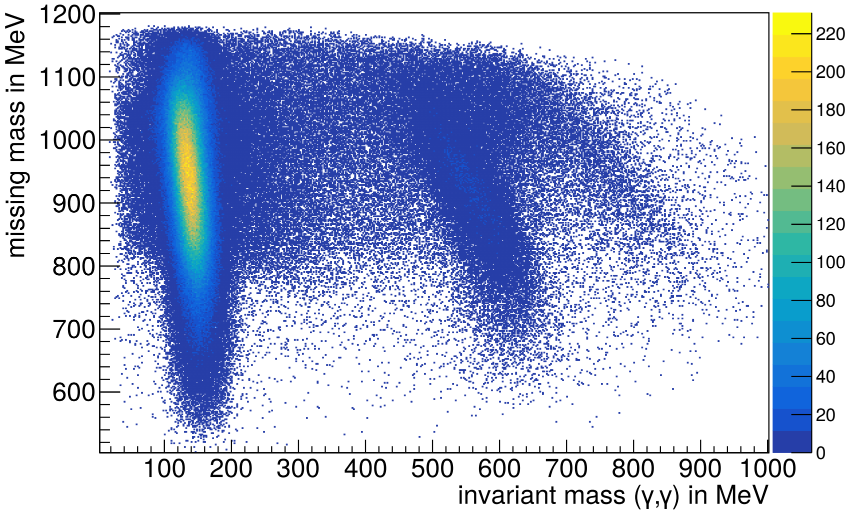

Figure 6.4: Missing mass plotted against 2γ invariant mass. The colour code denotes the number of entries.

Additional kinematical cuts are applied to reduce further background, by using the information of the detected proton candidates. Figure 6.5 shows the charged particle multiplicity in the BGO calorimeter and the SciRi detector for different conditions. One can see, that if charged particles were detected in only one detector, the multiplicity is for ~1% of all events larger than one. However, more than one charged particles are seen by both detectors simultaneously in ~10% of all events. Hence, it is important to find the correct outgoing proton candidate to be able to perform additional kinematical cuts. To select the proper outgoing proton candidate, the angular deviation of the outgoing detected particle with respect to the calculated missing proton is determined via

$$D = \sqrt{(\phi_{miss} - \phi_{meas})^2 + (\theta_{miss} - \theta_{meas})^2}. \tag{6.7}$$

The proton candidate with the smallest angular deviation D is kept. Figure 6.6a shows the distribution of the smallest angular deviation $\Delta\phi$ against $\Delta\theta$. While the distribution in $\Delta\phi$ is centred around zero, an offset of ~3.5° exists. The origin of this offset is due to the shifted target. The direction of the best fitting proton candidate is shown in figure 6.6b. It can be seen, that the proton candidate preferentially goes into forward angles of the BGO calorimeter and SciRi.

Once the proton candidate is fixed, the azimuthal angle between the proton candidate and the meson is determined. Since the initial state has no transversal momentum, the transversal momenta of the outgoing proton and meson candidate must be anti parallel. Hence, an azimuthal angle between the proton-meson pair of 180° is expected (coplanarity). Figure 6.7a shows the azimuthal angle ϕ between the proton and meson candidate in dependence of the polar difference $\Delta\theta_p$ of the measured proton

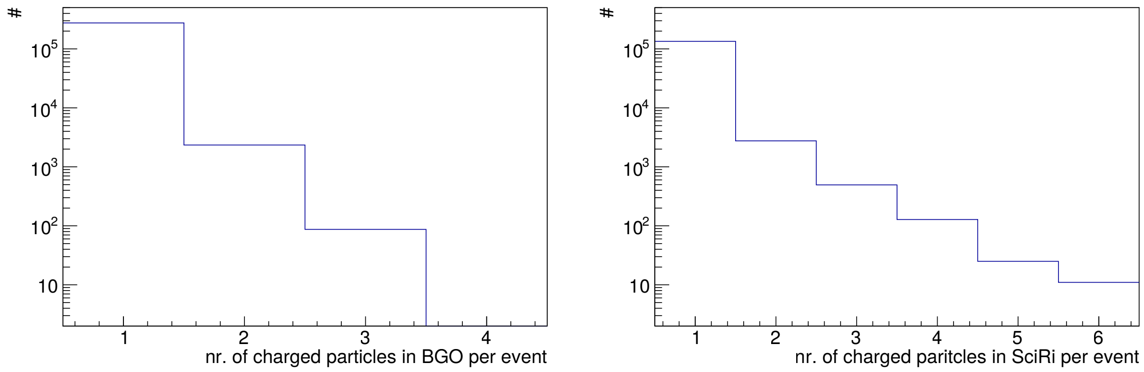

(a) Charged particle multiplicity in BGO if SciRi was not hit.

(b) Charged particle multiplicity in SciRi if BGO was not hit by charged particles.

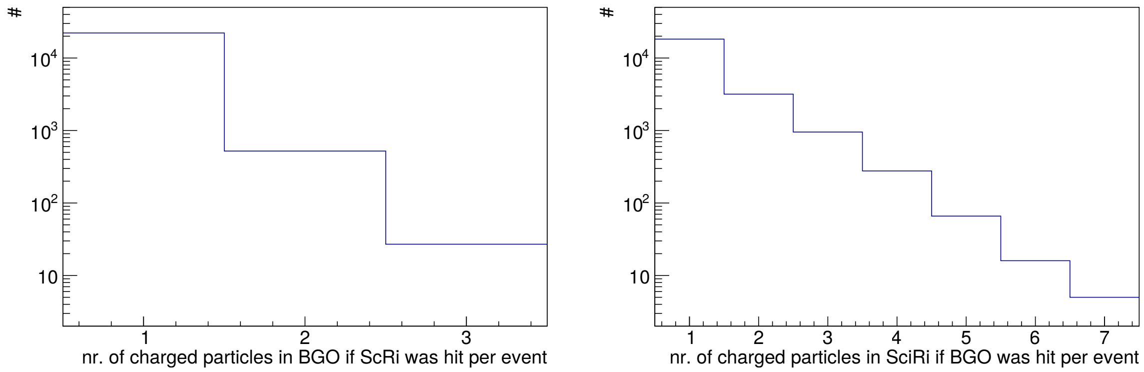

(c) Charged particle multiplicity in BGO if SciRi was hit.

(d) Charged particle multiplicity in SciRi if BGO was hit by charged particles.

Figure 6.5: Charged particle multiplicity in the BGO calorimeter and the SciRi detector in logarithmic scale for a smaller data sample.

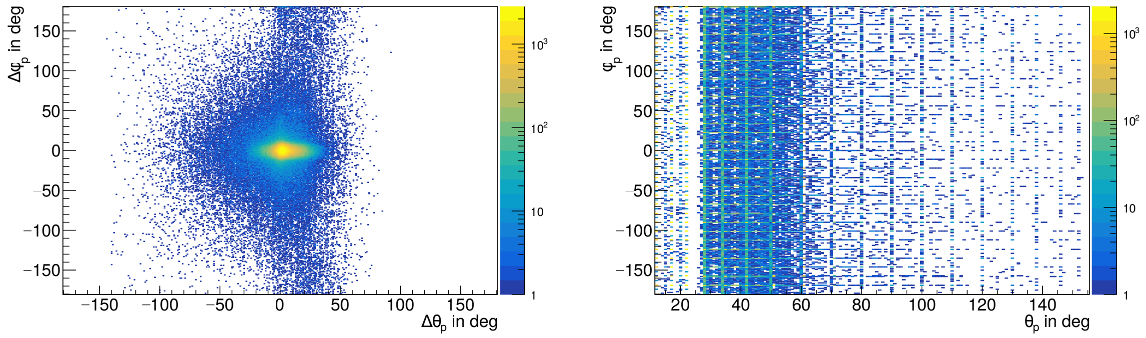

(a) Angular difference between best fitting proton candidate and missing proton. The colour code denotes the number of entries. An offset in θ of ~3.5° is present.

(b) Best fitting proton candidate angles. The colour code denotes the number of entries. The proton candidate preferentially goes into forward angles of the BGO calorimeter and SciRi.

Figure 6.6: Best fitting proton candidate directions.

candidate and the missing proton. The θ distribution shows an offset of ~3.5° originating from the shifted target. To select proper events, the $\Delta\theta$-coplanarity distribution is fitted with a two dimensional

Gaussian distribution. The events are selected according to the condition

$$\frac{(x-\mu_x)^2}{\sigma_x^2} + \frac{(y-\mu_y)^2}{\sigma_y^2} - \frac{2c\,(x-\mu_x)\,(y-\mu_y)}{\sigma_x\sigma_y} \leq \sigma^2(1-c^2) = 9(1-c^2), \tag{6.8}$$

with σ being set to 3 to consider almost all the events lying within the Gaussian distribution. μ_x and μ_y indicate the mean, σ_x and σ_y are the widths and c corresponds to the correlation parameter. The selected events by applying the two dimensional cut are shown in figure 6.7b.

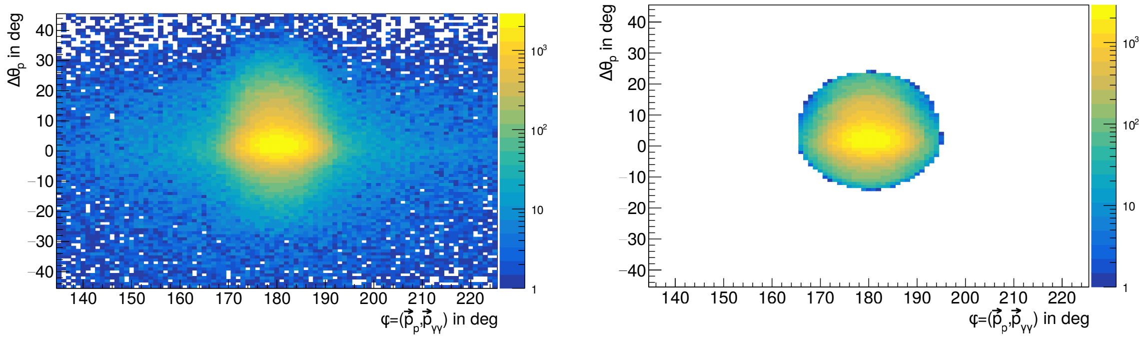

(a) The distribution of the azimuthal angle between the proton and the meson candidate has its maximum as expected at 180°. An offset of ~3.5° on the polar angle is visible.

(b) Selected events based on a two dimensional Gaussian fit.

Figure 6.7: Azimuthal angle ϕ between the proton and meson candidate in dependence of the polar angle difference $\Delta\theta_p$ between the measured proton candidate and the missing proton. The colour code denotes the number of entries in logarithmic scale.

A second kinematical cut is applied by comparing the expected energy of the meson candidate with the measured one. The comparison was performed for π^0 and η candidates separately. A broad cut on the 2γ invariant mass was performed from 40 MeV to 240 MeV to select π^0 candidates and from 400 MeV to 800 MeV to select η candidates. Using the information of the bremsstrahlung photon and of the meson and the proton candidates, the expected meson energy is determined via

$$E_{m,calc} = E_{\gamma,bs} \frac{\sin(\theta_p)\cos(\phi_m)}{\cos(\theta_p)\cdot(\sin(\theta_m)\cos(\phi_m) - \cos(\theta_m)\sin(\theta_p)\cos(\phi_p)/\cos(\theta_p))}. \tag{6.9}$$

Figure 6.8a and 6.8c show the deviation of the missing proton mass against the deviation of the expected meson energy for π^0 and η candidates. The spectra are again fitted with two dimensional Gaussian functions and the event selection was done according to equation 6.8. Events that did survive the kinematical conditions are shown in figure 6.8b and 6.8d.

By restricting the kinematics of the detected reactions, the background in figure 6.9a is strongly reduced. Figures 6.9b and 6.9c show the impact of the kinematical cuts on the missing mass versus 2γ invariant mass spectrum. The final π^0 and η candidates for the determination of the photon beam asymmetry in their 2γ decay channel are selected through a two dimensional Gaussian fit on the missing mass versus 2γ invariant mass spectrum (see figure 6.9c). The selection is shown in figure 6.9d.

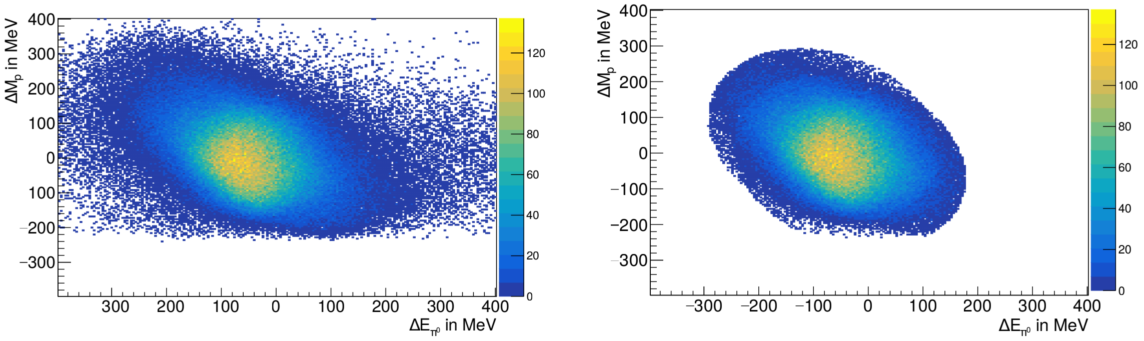

(a) Proton missing mass to nominal difference in MeV against measured to expected energy difference of meson candidate π^0 in MeV.

(b) Figure 6.8a after two dimensional Gaussian cut.

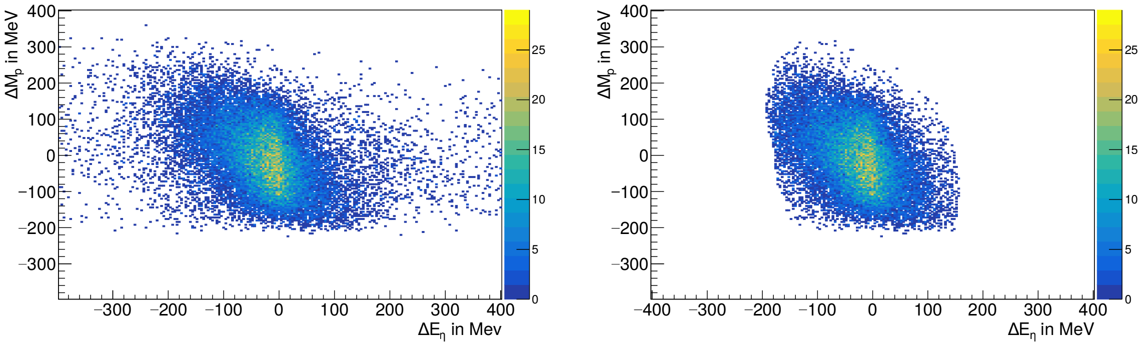

(c) Proton missing mass to nominal difference in MeV against measured to expected energy difference of meson candidate η in MeV.

(d) Figure 6.8c after two dimensional Gaussian cut.

Figure 6.8: Proton missing mass to nominal difference in MeV against measured to expected energy difference of meson candidates π^0 and η in MeV. The colour code denotes the number of entries.

6.3 Extraction of the photon beam asymmetry Σ

The photon beam asymmetry in $\gamma + \mathrm{p} \rightarrow \mathrm{p} + \pi^0 \rightarrow \mathrm{p} + \gamma\gamma$ and $\gamma + \mathrm{p} \rightarrow \mathrm{p} + \eta \rightarrow \mathrm{p} + \gamma\gamma$ is determined according to the formulae introduced in section 5.1.4 using the selected events shown in figure 6.9d. The azimuthal distribution of the reconstructed π^0 and η candidates is analysed for different incoming photon energy bins and different polar angle bins in the centre of mass system. As an example, figure 6.10a shows the azimuthal distribution of reconstructed π^0 candidates in an incoming photon energy range from 1100 MeV to 1150 MeV for the negatively orientated polarisation plane. It shows holes at azimuthal angles of 88° and -98° over the full polar angle range. The two holes are a consequence of a gap of 5 mm between the two halves of the BGO, which were not completely closed during the data taking. Since SciRi is connected to the structure of the BGO calorimeter, a gap in SciRi is also present. According to section 5.1.4, the acceptance hole does not affect the extraction of the photon beam asymmetry Σ, performed by the study of the azimuthal distribution of the ratio

$$\frac{\tilde{N}(\phi_\gamma = +45^\circ, E_\gamma, \theta, \phi) - \tilde{N}(\phi_\gamma = -45^\circ, E_\gamma, \theta, \phi)}{\tilde{N}(\phi_\gamma = +45^\circ, E_\gamma, \theta, \phi) + \tilde{N}(\phi_\gamma = -45^\circ, E_\gamma, \theta, \phi)} = P_{\gamma,l}(E_\gamma)\Sigma(E_\gamma, \theta)\sin(2\phi), \tag{6.10}$$

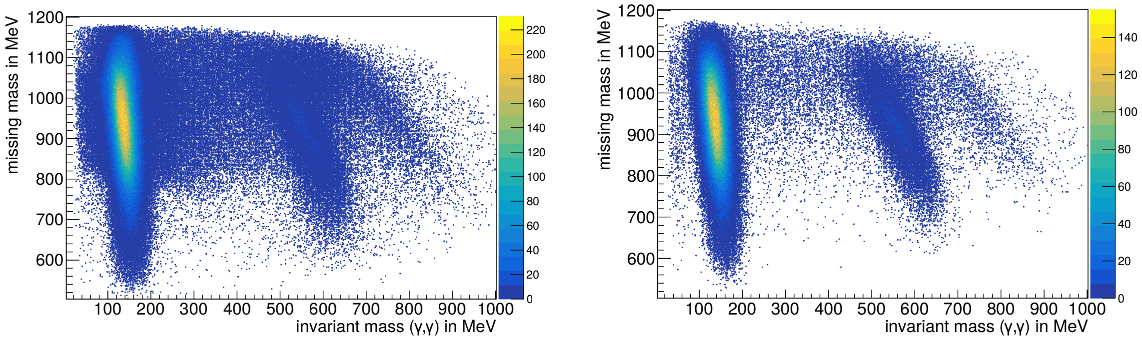

(a) Proton missing mass against 2γ invariant mass spectrum after fixing the bremsstrahlung photon.

(b) Proton missing mass against 2γ invariant mass spectrum after cut on the polar difference to the missing proton and cut on the azimuthal angle between proton and meson.

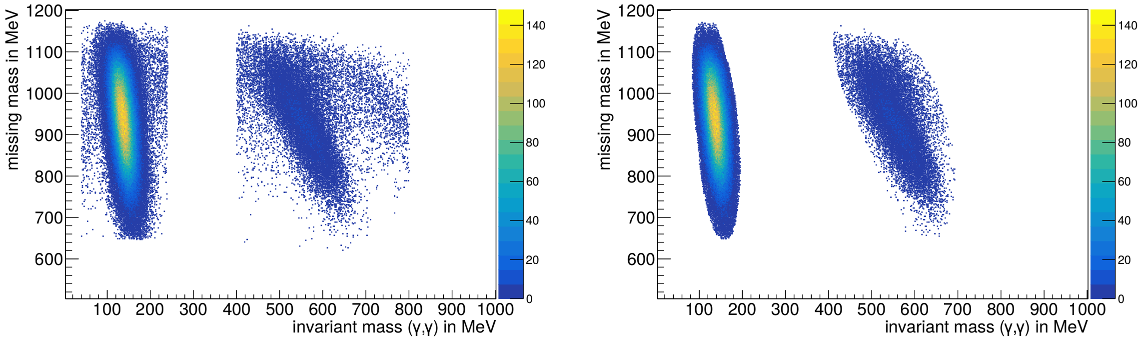

(c) Proton missing mass against 2γ invariant mass spectrum after cut on the missing to nominal proton mass difference and on the measured to expected meson energy difference.

(d) Proton missing mass against 2γ invariant mass spectrum after selecting π^0 and η candidates for the determination of the photon beam asymmetry.

Figure 6.9: Proton missing mass against 2γ invariant mass spectra for different conditions. The colour code denotes the number of entries.

where the detection inefficiencies cancel out. Since more data was taken with negatively orientated polarisation plane, the angular distribution of the reconstructed meson candidates was normalised by the yield for each bremsstrahlung photon energy bin. Figure 6.10b shows a typical $\sin(2\phi)$ modulation in π^0 photo-production in a bremsstrahlung photon energy bin of 1100 MeV to 1150 MeV for θ in the cms system between 50° to 70°. The $\sin(2\phi)$ modulation is fitted via

$$f(x) = a + b\sin(2(\phi + c)), \tag{6.11}$$

were a corresponds to an offset, b is the product $P\Sigma$ and c is a phase shift. The error bars shown in figure 6.10b correspond to the statistical error. The fit parameters corresponding to the offset and the phase shift of the azimuthal modulation are zero within their errors. From these results, one can conclude that the normalisation performed on the data is correct and the alignment of the polarisation planes works. The photon beam asymmetry is determined by dividing the fitted parameter b by the degree of linear polarisation P. Figure 6.11 shows the extracted photon beam asymmetry Σ for the reconstructed π^0 candidates plotted in incoming photon energy bin of 50 MeV from 1100 MeV to 1500 MeV and polar

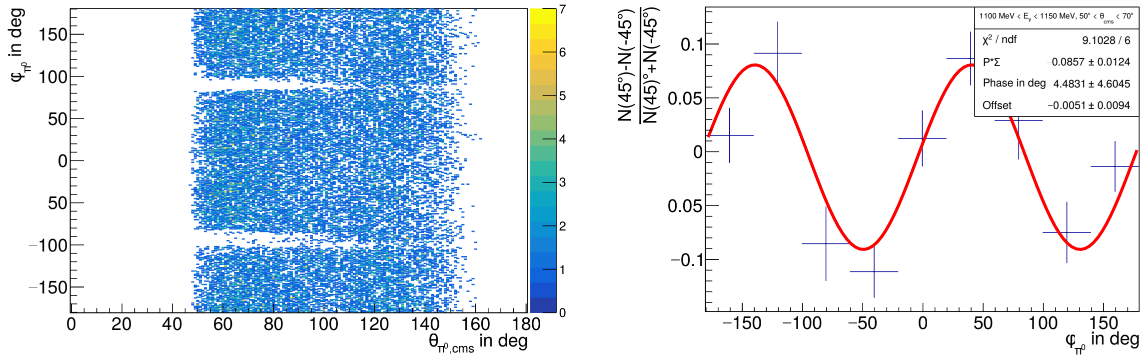

(a) Two dimensional angular distribution of reconstructed π^0 candidates in the cms system. The colour code denotes the number of entries. Holes at azimuthal angles of 88° and -98° over the full polar angle range are present due to a 5 mm gap between the two halves of the BGO calorimeter and SciRi.

(b) $\sin(2\phi)$ distribution in π^0 photo-production in a bremsstrahlung photon energy bin of 1100 MeV to 1150 MeV for θ in the cms system between 50° to 70° fitted with equation 6.11. Data points show the expected $\sin(2\phi)$ distribution. Offset and phase shift are zero within the errors.

Figure 6.10: Angular distribution of reconstructed π^0 candidates in the cms system.

angular steps of 20° compared with calculations of the BnGn parametrisation and the most precise data [53] used by BnGn. The error of the photon beam asymmetry correspond to the error of the fitted parameter b divided by the linear degree of polarisation P. Compared to the number of reconstructed π^0 candidates, the yield of reconstructed η candidates is smaller by a factor of ~10. Hence, the the photon beam asymmetry is extracted in larger energy and θ bins: four 100 MeV incoming energy bins from 1100 to 1400 MeV and a 150 MeV bin from 1400 MeV to 1550 MeV. The bin width in θ was increases to 30°. Due to the reduced statistics and based on the results of the photon beam asymmetry for π^0 photo-production, the azimuthal distribution is fitted by

$$f(x) = b\sin(2\phi), \tag{6.12}$$

putting the offset and the relative phase to zero. Figure 6.12 shows the extracted photon beam asymmetry Σ for the reconstructed η candidates with calculations of the BnGn parametrisation and the most precise data [54] used by BnGn.

6.4 Determination of systematic errors

Main sources of systematic errors are the absolute value of the polarisation degree and the possible background contamination of the selected signal sample. The systematic error on the polarisation degree is estimated with the analytical description of relative bremsstrahlung spectra (see section 5.2). The effect of the background on the photon beam asymmetry can be investigated through the variation of the applied kinematical cuts. By changing the relative background contribution, a change in the photon beam asymmetry is expected even if the background carries the azimuthal asymmetry.

The systematic error on the extracted photon beam asymmetry Σ is evaluated through variation of the kinematical cuts applied to select the signal events. To evaluate the effect of a remaining background contamination on the results of the photon beam asymmetry, the size of the cuts are varied from 3σ to 2σ width. Assuming a constant background, the signal to background ratio is then expected to increase, albeit on cost of statistics.

The variation has been applied for each cut individually (see section 6.2.3), in order to estimate the specific effect on the extracted photon beam asymmetry. As an example, the size of the kinematical cut applied on the coplanarity (see figure 6.7b) is varied from 3σ to 2σ without changing the size of the other selections. The photon beam asymmetry Σ is extracted for the reduced kinematical cut on the coplanarity and compared with the results of the 3σ case.

In case of correlated distributions, for example the meson energy and the missing proton mass (see figure 6.8a), the kinematical cuts are simultaneously changed from 3σ to 2σ. In addition, the photon beam asymmetry is extracted also with a simultaneously reduced size of all kinematical cuts to 2σ. The results are shown in figure 6.13 for the $p + \pi^0$ final state and in figure 6.14 for the $p + \eta$ final state.

6.5 Results and Discussion

Using the data set taken in June/July 2015, the photon beam asymmetry Σ in π^0 photo-production was determined with the goal to validate the alignment of the polarisation planes and the calculated results of the degree of polarisation of the produced bremsstrahlung photon beam.

The azimuthal distributions of the reconstructed π^0 candidates can be described with a $\sin 2\phi$ modulation. A fit with three parameters was used to extract the photon beam asymmetry in π^0-photo-production (see figure 6.10b). The fit parameters correspond to the amplitude, to the offset of the amplitude and to the azimuthal phase shift of the azimuthal modulation. Since the offset as well as the phase shift are zero within their errors it can be concluded that the alignment procedure of the polarisation planes works.

The extracted photon beam asymmetries for π^0-photo-production are shown in figure 6.11. In addition, the calculation of the BnGn parametrisation as a representation of the existing precise experimental results and the most precise data [53] used by BnGn are shown for comparison. The errors on the photon beam asymmetry resulting from the fit of the azimuthal modulations are based on statistics and range from $\Delta\Sigma = 0.08$ to $\Delta\Sigma = 0.17$. The results agree within the errors with the BnGn parametrisation as well with the data from CB/ELSA.

Systematic studies through sliding cuts show (see figure 6.13) that for a variation of the kinematical cuts, the photon beam asymmetry mostly changes well within the errors of the 3σ results. Additionally, no specific kinematical cut shows a systematic change to higher or smaller values of the photon beam asymmetry.

From this it can be concluded that the determination of the degree of polarisation of the produced bremsstrahlung photon beam is consistent with the results of the photon beam asymmetry determined in this thesis.

Since the dominant decay mode of the η is equivalent to the one of the π^0, the same analysis for the extraction of the photon beam asymmetry was applied to the η-photo-production channel, which is well measured in other experiments, too. Due to the smaller cross section in the η channel, the statistics available in the same data sample from June/July 2015 do not allow the extraction of the photon beam asymmetry with the same precision as the π^0 channel. However, it is interesting to see if the extracted photon beam asymmetry in the η channel generally follows the BnGn parametrisation.

The resulting photon beam asymmetries in η-photo-production are shown in figure 6.12 along with the BnGn parametrisation and the most precise data [54] used by BnGn. The errors on the photon beam asymmetry resulting from the fit of the azimuthal modulations are based on statistics and are between $\Delta\Sigma = 0.13$ and $\Delta\Sigma = 0.27$. With the given statistical errors a general agreement is obtained without observing an obvious inconsistency. Systematic studies through sliding cuts were also performed on the η channel, but conclusions can be hardly drawn from figure 6.14 due to the limited available statistics.

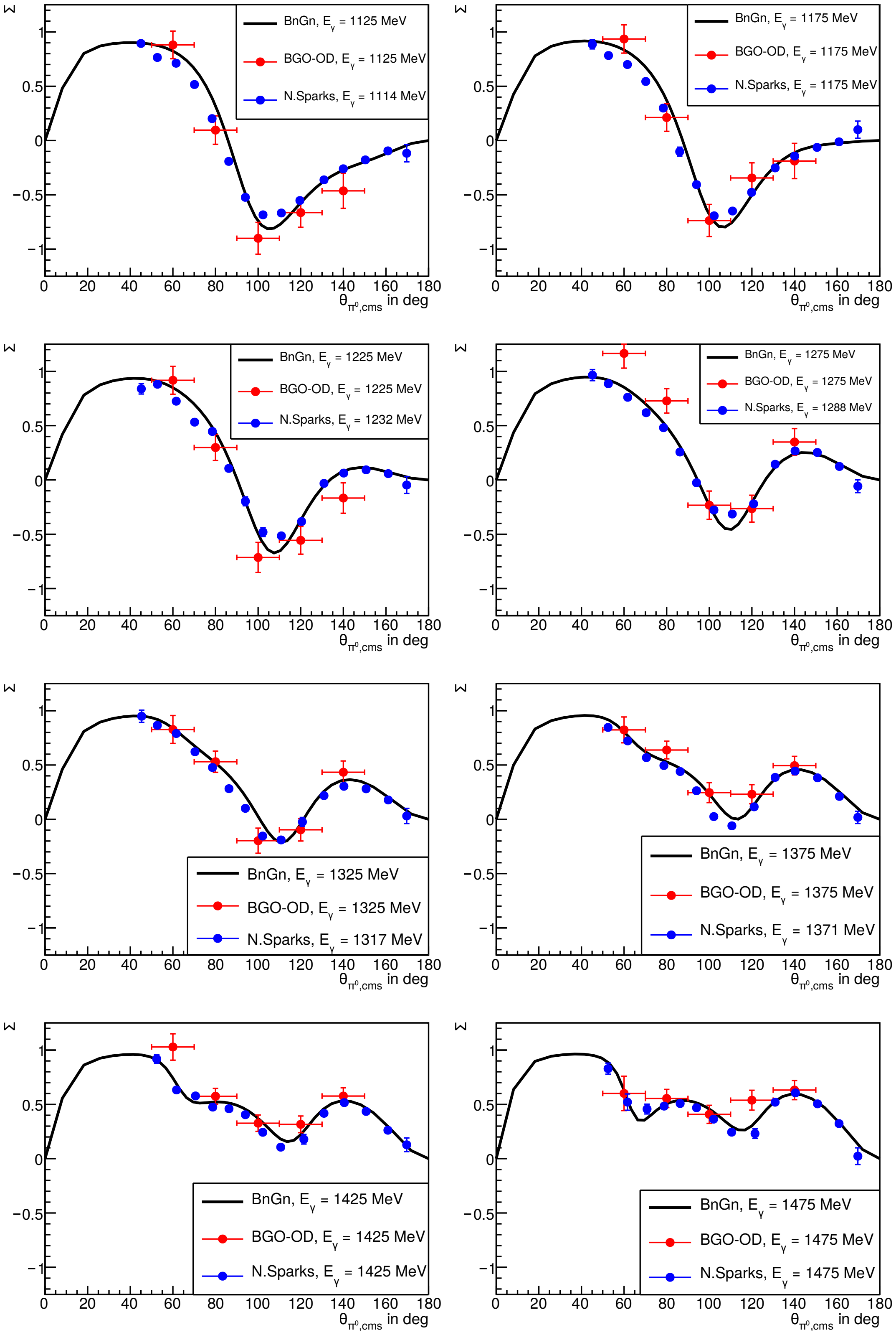

Figure 6.11: Extracted photon beam asymmetry Σ for π^0 photo-production (red points) compared to BnGn2014_02 (black line) and most precise data from N. Sparks (blue points) [53] used by BnGn. The errors are based on statistics.

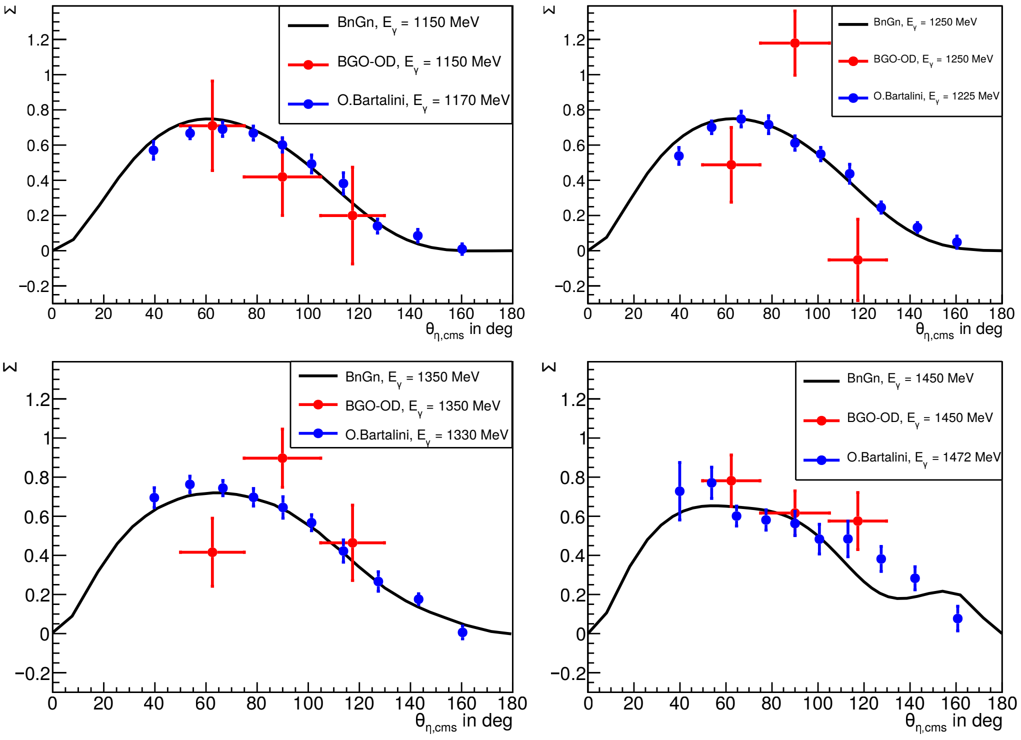

Figure 6.12: Extracted photon beam asymmetry Σ for η photo-production (red points) compared to BnGn2014_02 (black line) and most precise data from O. Bartalini (blue points) [54] used by BnGn. The errors are based on statistics.

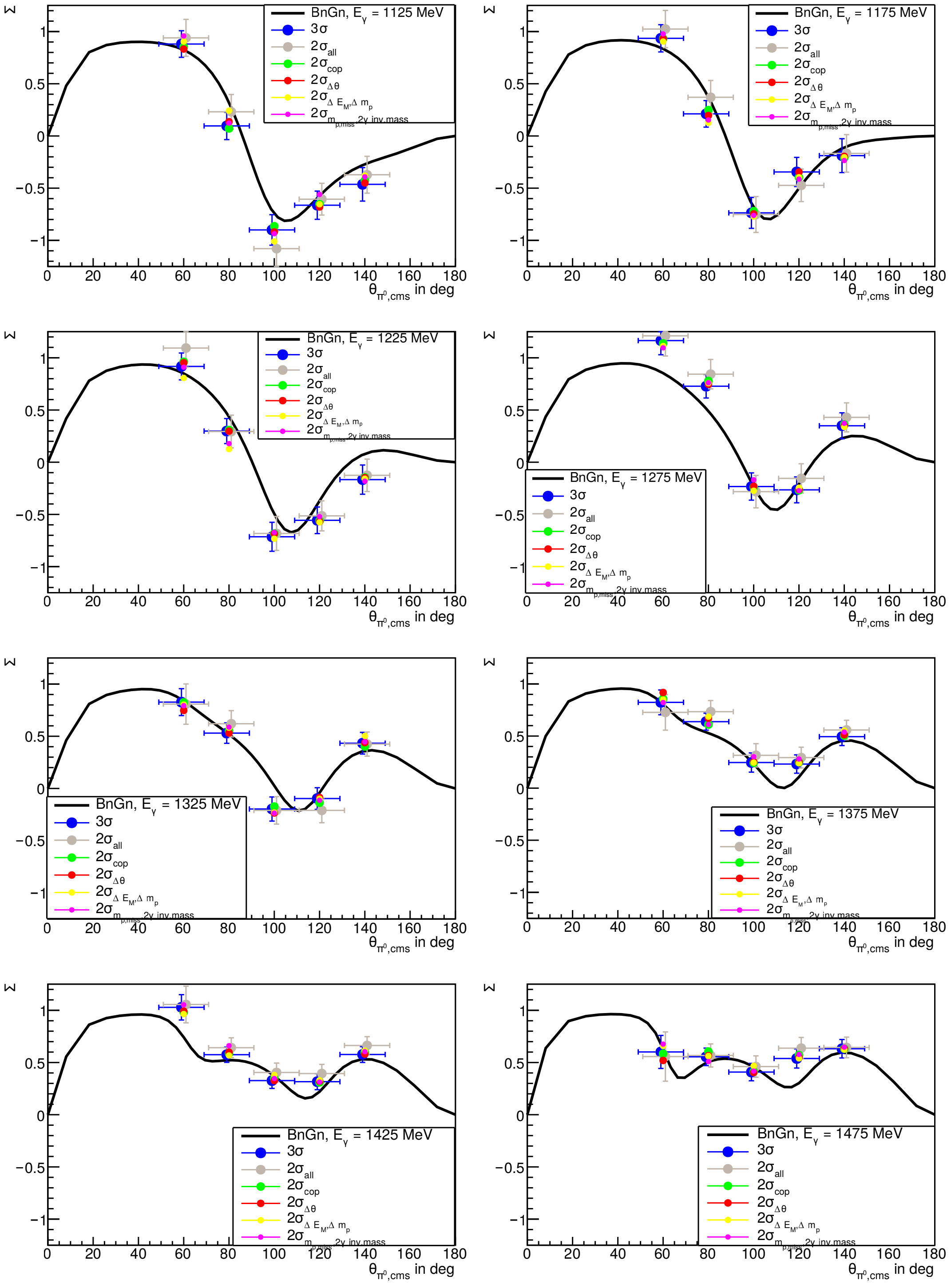

Figure 6.13: Extracted photon beam asymmetry Σ for π^0 photo-production for different kinematical restrictions. Blue (grey) data points correspond to the results for a selection size of 3σ (2σ) applied on all kinematical conditions. Green corresponds to an individually reduced cut size on the coplanarity, red on the polar angle difference of the recoil proton, yellow on the missing proton mass difference and meson energy difference, and purple on the missing proton mass and the 2γ invariant mass. The blue and grey data points were shifted by -1° respectively +1° to increase the visibility. For the same reason the errors for the green, red, yellow and purple data point are not plotted. The black curve shows the BnGn2014_02 parametrisation.

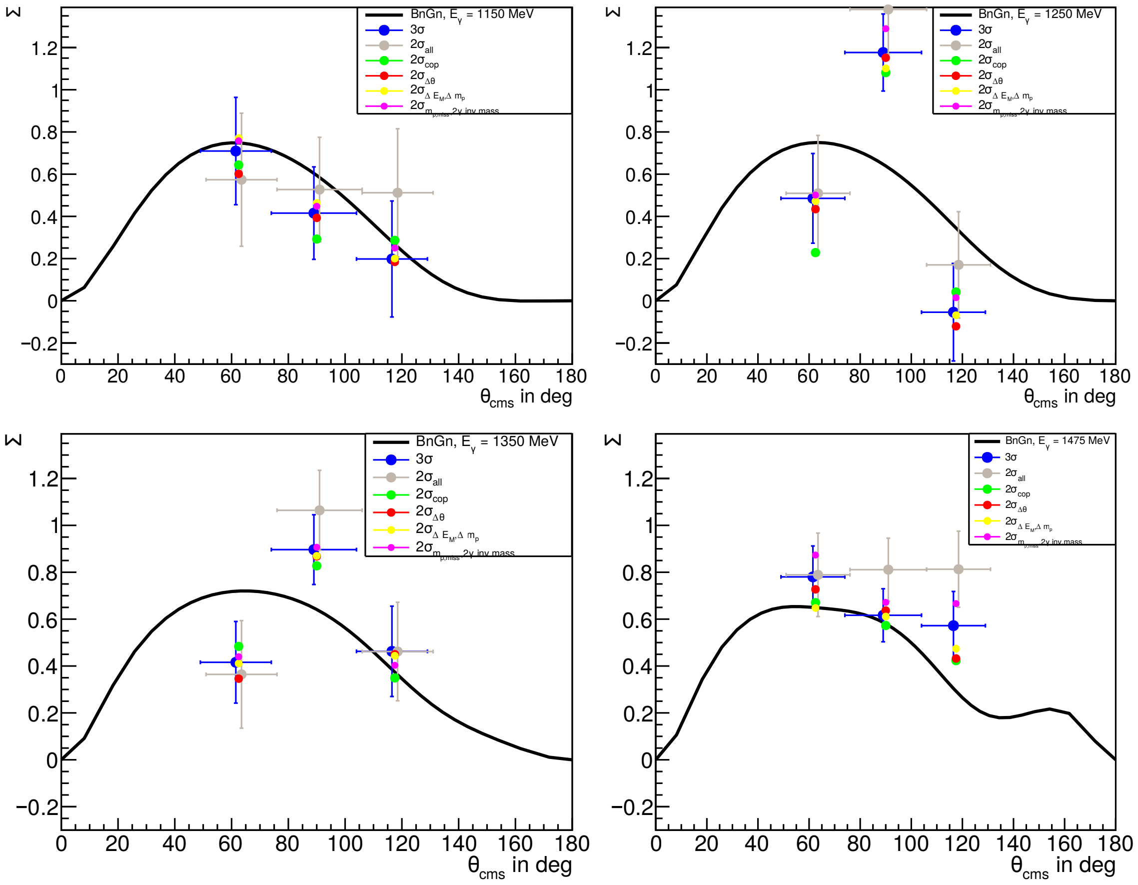

Figure 6.14: Extracted photon beam asymmetry Σ for η photo-production for different kinematical restrictions. Blue (grey) data points correspond to the results for a selection size of 3σ (2σ) applied on all kinematical conditions. Green corresponds to an individually reduced cut size on the coplanarity, red on the polar angle difference of the recoil proton, yellow on the missing proton mass difference and meson energy difference, and purple on the missing proton mass and the 2γ invariant mass. The blue and grey data points were shifted by -1° respectively +1° to increase the visibility. For the same reason the errors for the green, red, yellow and purple data point are not plotted. The black curve shows the BnGn2014_02 parametrisation.

CHAPTER 7

Summary and Conclusion

The BGO-OD experiment is a newly commissioned meson photo-production experiment located at the electron stretcher facility ELSA in Bonn. The highly energetic photon beam is produced via bremsstrahlung of electrons scattering off an amorphous or crystalline radiator. In the latter case, the process of coherent bremsstrahlung and therefore the production of linearly polarised photon beams is possible. The energy spectrum of bremsstrahlung is continuous and therefore the energy of a produced bremsstrahlung photon is a priori unknown. A *photon tagger*, which consists mainly of a dipole magnet and a scintillator hodoscope, allows to determine the energy of the produced bremsstrahlung photon event-by-event through the measurement of the momentum of the corresponding post-bremsstrahlung electron.

The main part of this thesis comprises the design, the assembling and the commissioning of the hodoscope of the photon tagger system of the BGO-OD experiment.

The mechanical frame of the hodoscope is developed with *Autodesk Inventor*, based on the scintillator arrangement computed in [48]. Due to spatial restrictions given by the dipole magnet and the beam dump, the hodoscope is split into two parts. One part lies horizontally within the focal plane of the dipole magnet, while the second part is mounted vertically close to the beam dump.

A coverage of an energy range between 10% and 90% of the incoming primary electron beam energy E_0 is achieved with 120 partly overlapping scintillator bars. Energy calibrations were performed with different primary electron beam energies to determine the mean energy values and the energy widths of each coincidence channel defined by the overlap of two adjacent scintillator bars. The energy widths amount to $0.55\%E_0$ for the horizontal hodoscope and range between $0.79\%E_0$ and $2.28\%E_0$ within the vertical part.

The mechanical frame of the hodoscope is designed such, that maintenance and exchange of scintillator bars do not affect the energy calibration of the hodoscope. Tests on the stability of the energy calibration with respect to the reinstallation of scintillator bars show that the energy information remains stable within its errors.

Since the tagger system defines the start time of a trigger event during data taking, a good time resolution and a stable operation at high rates is required. With the electronic setup used for the photon tagger, a stable operation at rate >50 MHz can be guaranteed with a time resolution of better than 210 ps.

Tools for the production of linearly polarised photon beams at the BGO-OD experiment are made operational within this work and are successfully used since November 2014. Linearly polarised photon beams are produced through coherent bremsstrahlung off a diamond radiator, properly aligned with respect to the direction of the primary electron beam. The precise positioning is enabled through a commercial goniometer system. The goniometer also serves to determine the important angular offsets between the diamond lattice and the primary electron beam via the *Stonehenge technique* [1].

The absolute degree of linear polarisation of the photon beam is determined from the post-bremsstrahlung electron spectrum. The analytical calculation is performed using a C++ based program called COBRIS [2]. A fitting routine based on the ROOT framework was added to COBRIS in the course of this thesis. It improves the calculation of the degree of polarisation and the determination of the error based on the uncertainty of the input parameters.

Finally, to perform a cross check of the determination of the degree of linear polarisation, the photon beam asymmetry Σ is determined in π^0 photo-production off the proton. Data taken in June/July 2015 are analysed, for which the main coherent contribution is set at 1550 MeV for a primary electron beam energy of 2900 MeV. The maximum expected degree of linear polarisation amounts to $\sim 28.8\%$. The energy range from 1100 MeV to 1500 MeV is used in the analysis, where the expected degree of linear polarisation is $>10\%$.

Within the statistical errors, the extracted photon beam asymmetries in π^0 photo-production are consistent with the BnGn parametrisations as well as with the data from N. Sparks [53].

Since the dominant decay mode of the η is equivalent to the one of the π^0, the photon beam asymmetry is also extracted in η photo-production. Albeit with less precision due to limited statistics, the extracted photon beam asymmetries in η photo-production also generally follow the BnGn parametrisations and the data from O. Bartalini [54].

The relative error on the degree of polarisation derived from the error on the photon beam asymmetry in π^0 photo-production is in the order of 10%. This is limited by the statistical precision reached in the photon beam asymmetry measurement using the limited data set described. A more likely relative error on the degree of polarisation of $1\% - 2\%$ is determined from COBRIS (see section 5.2). It will be possible with future measurements to parasitically prove the accuracy of the determined degree of polarisation with more statistics.

APPENDIX A

System of Units

The natural unit system is used in chapter 2 of this Phd thesis and definded by

$$\hbar = c == m_e = 1. \tag{A.1}$$

Due to this definition different physical units getting the same dimension:

$$[\text{mass}] = [\text{energy}] = [\text{momentum}] = [\text{length}]^{-1} = [\text{time}]^{-1} \tag{A.2}$$

Si units are recovered by multiplying

$$\begin{aligned} \text{length by } \lambda &= \frac{\hbar}{m_e c} = 3.8616 \cdot 10^{-13}\,\text{m} \\ \text{momentum by } m_e c &= \frac{0.511\,\text{MeV}}{c} = 2.731 \cdot 10^{-22}\frac{\text{kg}\cdot\text{m}}{\text{s}^2} \\ \text{energy by } m_e c^2 &= 0.511\,\text{MeV} = 8.1872 \cdot 10^{-14}\frac{\text{kg}\cdot\text{m}^2}{\text{s}^2} \end{aligned}$$

The lattice constant is given by

$$a = 3.567 \cdot 10^{-10}\,m = 923.7 \tag{A.3}$$

Cross sections are given in units of $\bar{\sigma}$

$$\bar{\sigma} = Z^2 r^2 \alpha = 0.57947\,Z^2 = Z^2\alpha^3 \tag{A.4}$$

APPENDIX B

Scintillator material Ejen EJ-204

EJ-204 PLASTIC SCINTILLATOR

In addition to providing the highest scintillation efficiency of any plastic scintillator, EJ-204 delivers the excellent combination of high speed and good attenuation length. It is thus particularly well suited for high-performance detector systems for nuclear and high energy physics research.

It's emission wavelength near 400 nm couples ideally with bialkali phototubes while still being long enough to be effectively used with UVT light guides.

Physical and Scintillation Constants:

Light Output, % Anthracene	68
Scintillation Efficiency, photons/1 MeV e$^-$	10,400
Wavelength of Max. Emission, nm	408
Rise Time, ns	0.7
Decay Time, ns	1.8
Pulse Width, FWHM, ns	2.2
No. of H Atoms per cm^3, x 10^{22}	5.15
No. of C Atoms per cm^3, x 10^{22}	4.68
No. of Electrons per cm^3, x 10^{23}	3.33
Density, g/cc:	1.023

Polymer Base: ………… Polyvinyltoluene
Refractive Index: ……….1.58
Vapor Pressure: ……….. Is vacuum-compatible
Coefficient of Linear
Expansion: ……………… 7.8 x 10^{-5} below +67°C

Light Output vs. Temperature:
At +60°C, L.O. = 95% of that at +20°C
No change from +20°C to -60°C

Chemical Compatibility: Is attacked by aromatic solvents, chlorinated solvents, ketones, solvent bonding cements, etc. It is stable in water, dilute acids and alkalis, lower alcohols and silicone greases. It is safe to use most epoxies and "super glues" with EJ-204.

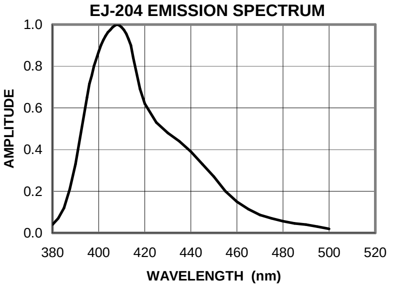

ELJEN TECHNOLOGY
1300 W Broadway
Sweetwater TX 79556 USA

Tel: (325) 235-4276 or (888) 800-8771
Fax: (325) 235-0701
Website: www.eljentechnology.com

APPENDIX C

Photomultipliers

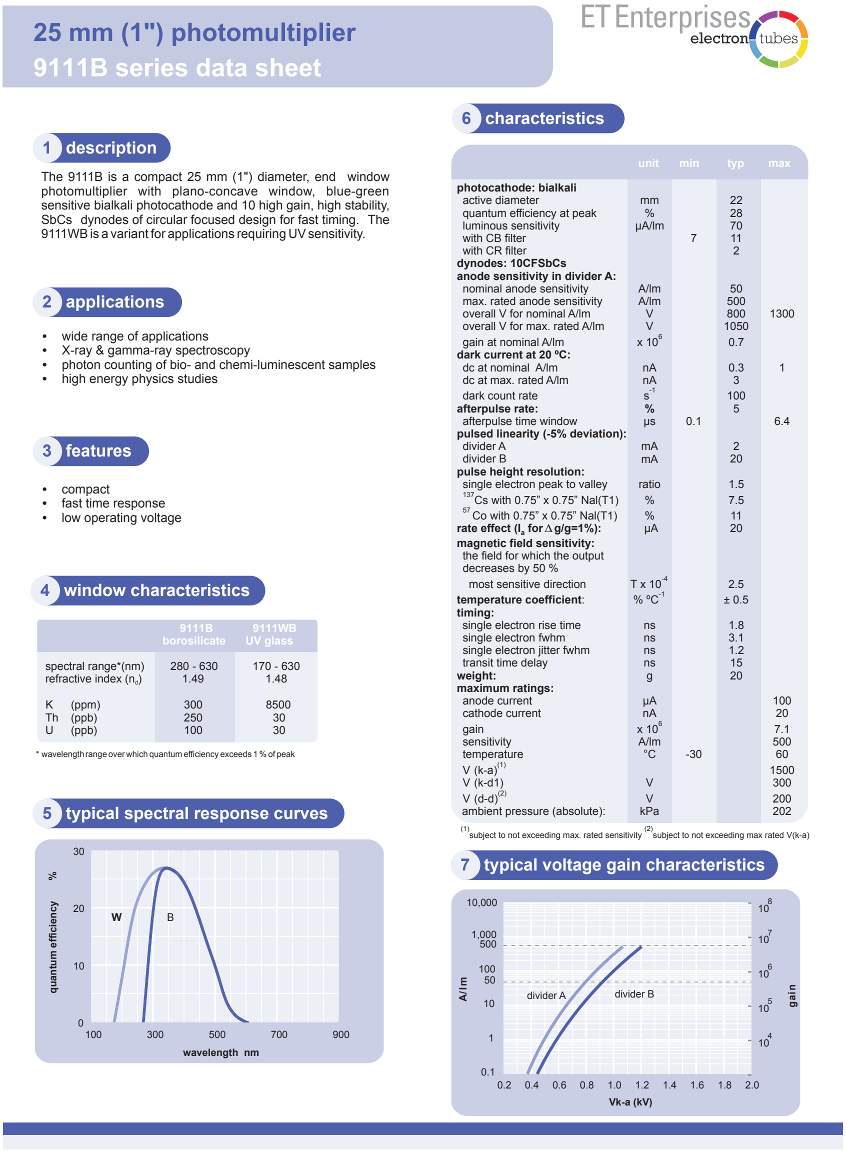

25 mm (1") photomultiplier
9111B series data sheet

ET Enterprises
electron tubes

1 description

The 9111B is a compact 25 mm (1") diameter, end window photomultiplier with plano-concave window, blue-green sensitive bialkali photocathode and 10 high gain, high stability, SbCs dynodes of circular focused design for fast timing. The 9111WB is a variant for applications requiring UV sensitivity.

2 applications

- wide range of applications
- X-ray & gamma-ray spectroscopy
- photon counting of bio- and chemi-luminescent samples
- high energy physics studies

3 features

- compact
- fast time response
- low operating voltage

4 window characteristics

	9111B borosilicate	9111WB UV glass
spectral range*(nm)	280 - 630	170 - 630
refractive index (n_d)	1.49	1.48
K (ppm)	300	8500
Th (ppb)	250	30
U (ppb)	100	30

* wavelength range over which quantum efficiency exceeds 1 % of peak

5 typical spectral response curves

6 characteristics

	unit	min	typ	max
photocathode: bialkali				
active diameter	mm		22	
quantum efficiency at peak	%		28	
luminous sensitivity	µA/lm		70	
with CB filter		7	11	
with CR filter			2	
dynodes: 10CFSbCs				
anode sensitivity in divider A:				
nominal anode sensitivity	A/lm		50	
max. rated anode sensitivity	A/lm		500	
overall V for nominal A/lm	V		800	1300
overall V for max. rated A/lm	V		1050	
gain at nominal A/lm	x 10^6		0.7	
dark current at 20 ºC:				
dc at nominal A/lm	nA		0.3	1
dc at max. rated A/lm	nA		3	
dark count rate	s^{-1}		100	
afterpulse rate:	**%**		5	
afterpulse time window	µs	0.1		6.4
pulsed linearity (-5% deviation):				
divider A	mA		2	
divider B	mA		20	
pulse height resolution:				
single electron peak to valley	ratio		1.5	
^{137}Cs with 0.75" x 0.75" NaI(T1)	%		7.5	
^{57}Co with 0.75" x 0.75" NaI(T1)	%		11	
rate effect (I_a for $\Delta g/g$=1%):	µA		20	
magnetic field sensitivity:				
the field for which the output decreases by 50 %				
most sensitive direction	T x 10^{-4}		2.5	
temperature coefficient:	% ºC^{-1}		± 0.5	
timing:				
single electron rise time	ns		1.8	
single electron fwhm	ns		3.1	
single electron jitter fwhm	ns		1.2	
transit time delay	ns		15	
weight:	g		20	
maximum ratings:				
anode current	µA			100
cathode current	nA			20
gain	x 10^6			7.1
sensitivity	A/lm			500
temperature	°C	-30		60
V (k-a)(1)				1500
V (k-d1)	V			300
V (d-d)(2)	V			200
ambient pressure (absolute):	kPa			202

(1) subject to not exceeding max. rated sensitivity (2) subject to not exceeding max rated V(k-a)

7 typical voltage gain characteristics

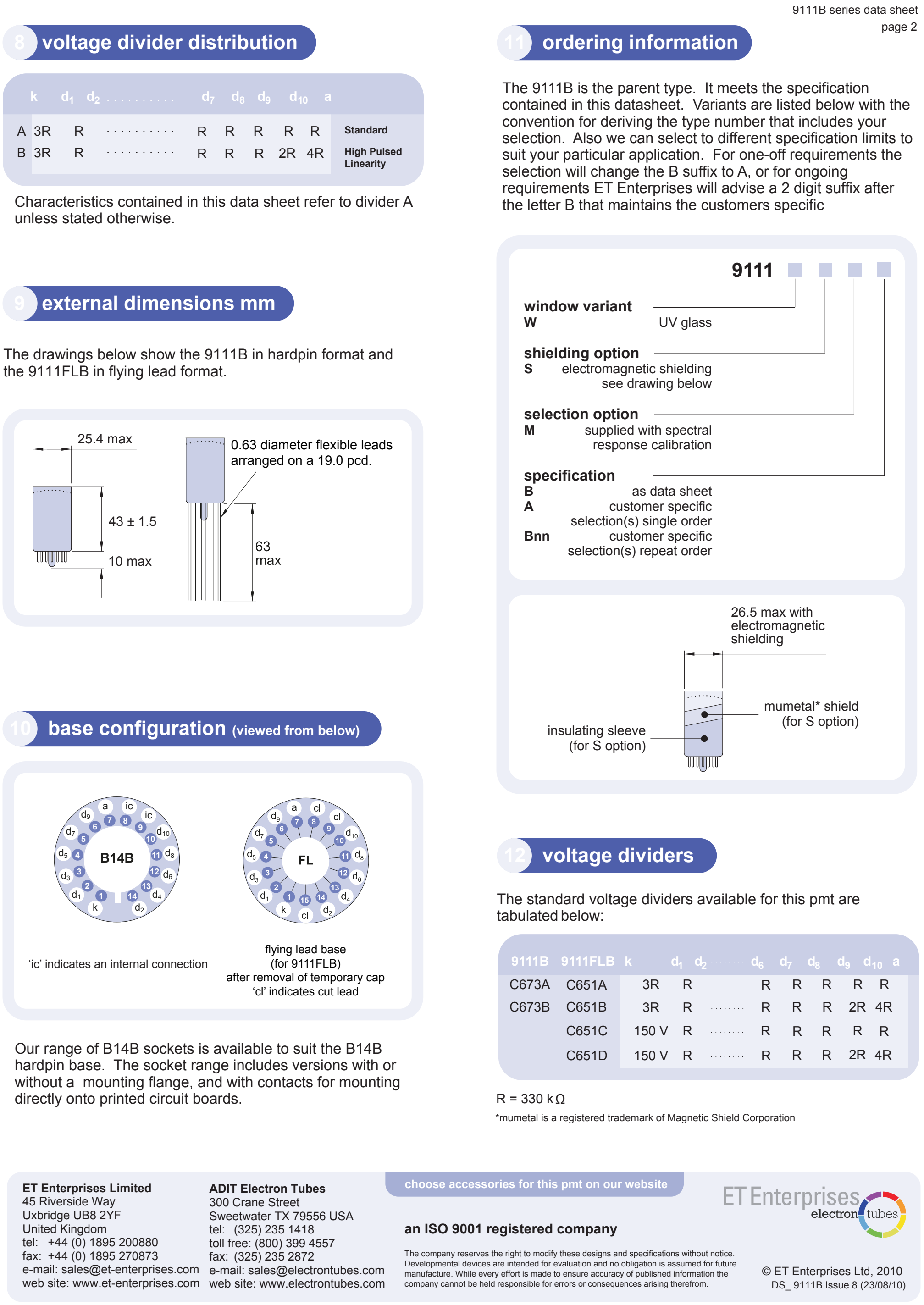

8 voltage divider distribution

	k	d1	d2	d7	d8	d9	d10	a	
A	3R	R	....	R	R	R	R	R	**Standard**
B	3R	R	....	R	R	R	2R	4R	**High Pulsed Linearity**

Characteristics contained in this data sheet refer to divider A unless stated otherwise.

9 external dimensions mm

The drawings below show the 9111B in hardpin format and the 9111FLB in flying lead format.

10 base configuration (viewed from below)

‘ic’ indicates an internal connection

flying lead base
(for 9111FLB)
after removal of temporary cap
‘cl’ indicates cut lead

Our range of B14B sockets is available to suit the B14B hardpin base. The socket range includes versions with or without a mounting flange, and with contacts for mounting directly onto printed circuit boards.

11 ordering information

The 9111B is the parent type. It meets the specification contained in this datasheet. Variants are listed below with the convention for deriving the type number that includes your selection. Also we can select to different specification limits to suit your particular application. For one-off requirements the selection will change the B suffix to A, or for ongoing requirements ET Enterprises will advise a 2 digit suffix after the letter B that maintains the customers specific

9111 ■ ■ ■ ■

window variant
W UV glass

shielding option
S electromagnetic shielding see drawing below

selection option
M supplied with spectral response calibration

specification
B as data sheet
A customer specific selection(s) single order
Bnn customer specific selection(s) repeat order

12 voltage dividers

The standard voltage dividers available for this pmt are tabulated below:

9111B	9111FLB	k	d1	d2 ········	d6	d7	d8	d9	d10	a
C673A	C651A	3R	R	········	R	R	R	R	R	
C673B	C651B	3R	R	········	R	R	R	2R	4R	
	C651C	150 V	R	········	R	R	R	R	R	
	C651D	150 V	R	········	R	R	R	2R	4R	

R = 330 kΩ

*mumetal is a registered trademark of Magnetic Shield Corporation

ET Enterprises Limited
45 Riverside Way
Uxbridge UB8 2YF
United Kingdom
tel: +44 (0) 1895 200880
fax: +44 (0) 1895 270873
e-mail: sales@et-enterprises.com
web site: www.et-enterprises.com

ADIT Electron Tubes
300 Crane Street
Sweetwater TX 79556 USA
tel: (325) 235 1418
toll free: (800) 399 4557
fax: (325) 235 2872
e-mail: sales@electrontubes.com
web site: www.electrontubes.com

choose accessories for this pmt on our website

an ISO 9001 registered company

ET Enterprises electron tubes

DS_ 9111B Issue 8 (23/08/10)

HAMAMATSU

METAL PACKAGE PHOTOMULTIPLIER TUBE R7400U SERIES

Compact size (16 mm diameter, 12 mm seated length), Fast Time response (rise time 0.78 ns)

The R7400U series is a subminiature photomultiplier tube with a 16 mm diameter and 12 mm seated length. A precision engineered 8-stage electron multiplier (composed of metal channel dynodes) is incorporated in the TO-8 package to produce a noise free gain of 700,000 times (R7400U). The R7400U series also features excellent response time with a rise time of 0.78 ns. Various types of the R7400U series are available with different spectral response and gain ranges, including those selected specifically for photon counting applications. Hamamatsu also provides a lens input option to the series (R7401 and R7402), effectively doubling the active area.

Left: R7400U Right: R7401/R7402

FEATURES

- World's smallest photomultiplier tubes assembled. (1/7th of the Hamamatsu R647)
  The necessary components are built into a TO-8 package while retaining full photomultiplier tube performance to create a new generation of photosensors.
- Specially selected on account of low noise and high gain. For use in photon counting applications.
- The lens window type doubles the effective input area to 12 mm in diameter.

SERIES

	Solar Blind	UV to Visible Range		Visible Range	Visible to Near IR Range			UV to Near IR Range
Standard	R7400U-09	R7400U-03	R7400U-06	R7400U	R7400U-01	R7400U-02	R7400U-20	R7400U-04
For Photon Counting	—	—	—	R7400P, R7401P	—	—	—	—
With Lens	—	—	—	R7401	R7402	R7402-02	R7402-20	—

SPECIFICATIONS

GENERAL

Parameter		Description/Value	Unit
Minimum Effective Area		ϕ8	mm
Dynode	Structure	Metal Channel	—
	Number of Stages	8	—
Weight	Without Lens	Approx. 5.3	g
	With Lens	Approx. 6.3	g
Operating Ambient Temperature and Storage Temperature	Without Lens	-80 to +50	°C
	With Lens	-30 to +50	°C

VOLTAGE DISTRIBUTION RATIO

Electrodes	K		Dy1		Dy2		Dy3		Dy4		Dy5		Dy6		Dy7		Dy8		P
Ratio		1		1		1		1		1		1		1		1		0.5	

Supply Voltage: 800 V K: Cathode Dy: Dynode P: Anode

METAL PACKAGE PHOTOMULTIPLIER TUBE R7400U SERIES

CHARACTERISTICS (at 25 °C)

Type No.	Remarks	Spectral Response		Photo-cathode Material	Window Material	Out-line No.(a)	Maximum Ratings		Cathode Characteristics				
		Range (nm)	Peak Wave-length (nm)				Anode to Cathode Voltage (V)	Average Anode Current(b) (mA)	Luminous Min. (μA/lm)	Luminous Typ. (μA/lm)	Blue Sensitivity Index (CS 5-58) Typ.	Red/White Ratio (R-68) Typ.	Radiant Typ. (mA/W)
R7400U-09	Solar Blind	160 to 320	240	Cs-Te	Synthetic silica	w	1000	0.01	—	—	—	—	10(c)
R7400U	Visible	300 to 650	420	Bialkali	Borosilicate glass	q	1000	0.1	40	70	8	—	62
R7400U-03	UV to Visible	185 to 650	420	Bialkali	UV glass	q	1000	0.1	40	70	8	—	62
R7400U-06	UV to Visible	160 to 650	420	Bialkali	Synthetic silica	w	1000	0.1	40	70	8	—	62
R7400U-01	Visible to Near IR	300 to 850	400	Multialkali	Borosilicate glass	q	1000	0.1	80	150	—	0.20	60
R7400U-02	Visible to Near IR	300 to 880	500	Multialkali	Borosilicate glass	q	1000	0.1	200	250	—	0.25	58
R7400U-20	Visible to Near IR	300 to 920	630	Multialkali	Borosilicate glass	q	1000	0.1	350	500	—	0.45	78
R7400U-04	UV to Near IR	185 to 850	400	Multialkali	UV glass	q	1000	0.1	80	150	—	0.20	60
R7401	With Lens	300 to 650	420	Bialkal	Borosilicate glass	e	1000	0.1	40	70	8	—	62
R7402	With Lens	300 to 850	400	Multialkali	Borosilicate glass	e	1000	0.1	80	150	—	0.20	60
R7402-02	With Lens	300 to 880	500	Multialkali	Borosilicate glass	e	1000	0.1	200	250	—	0.25	58
R7402-20	With Lens	300 to 920	630	Multialkali	Borosilicate glass	e	1000	0.1	350	500	—	0.45	78

(a): See figure 11.   (b): Averaged over any interval of 30 seconds maximum.   (c): Measured at 254 nm.   (d): Measured after 30 minutes storage in darkness.
(e): Measured at 410 nm, at -800 V, with an input pulse width less than 30 ps.   (f): Measured at a gain of 10^6.

Figure 1: Typical Spectral Response (Cs-Te)

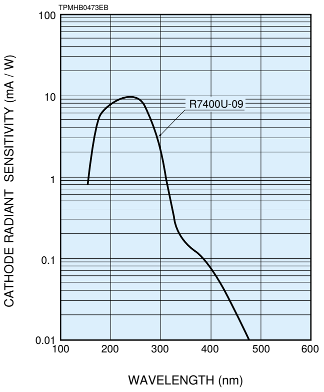

Figure 2: Typical Spectral Response (Bialkali)

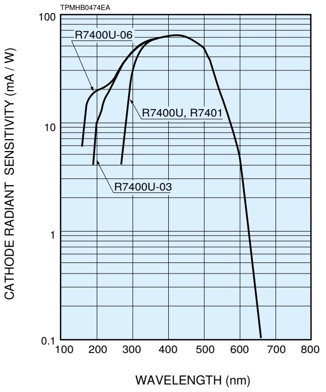

Figure 3: Typical Spectral Response (Multialkali)

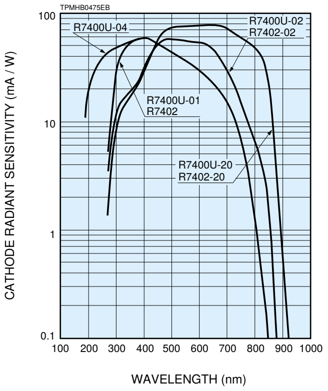

Anode to Cathode Supply Voltage (V)	Anode Characteristics									Type No.
	Anode Sensitivity			Gain Typ.	Anode Dark Current (d)		Time Response			
	Luminous		Radiant Typ. (A/W)		Typ. (nA)	Max. (nA)	RiseTime Typ. (ns)	Transit Time Typ. (ns)	Transit Time Spread (T.T.S.) (e) (ns)	
	Min. (A/lm)	Typ. (A/lm)								
800	—	—	1100(c)	5×10^4	0.025	0.5	0.78	5.4	0.23	R7400U-09
800	10	50	4.3×10^4	7×10^5	0.2	2	0.78	5.4	0.23	R7400U
800	10	50	4.3×10^4	7×10^5	0.2	2	0.78	5.4	0.23	R7400U-03
800	10	50	4.3×10^4	7×10^5	0.2	2	0.78	5.4	0.23	R7400U-06
800	15	75	3.0×10^4	5×10^5	0.4	4	0.78	5.4	0.23	R7400U-01
800	25	125	2.9×10^4	5×10^5	2	20	0.78	5.4	0.23	R7400U-02
800	35	250	3.9×10^4	5×10^5	2	20	0.78	5.4	0.23	R7400U-20
800	15	75	3.0×10^4	5×10^5	0.4	4	0.78	5.4	0.23	R7400U-04
800	10	50	4.3×10^4	7×10^5	0.2	2	0.78	5.4	0.23	R7401
800	15	75	3.0×10^4	5×10^5	0.4	4	0.78	5.4	0.23	R7402
800	25	125	2.9×10^4	5×10^5	2	20	0.78	5.4	0.23	R7402-02
800	35	250	3.9×10^4	5×10^5	2	20	0.78	5.4	0.23	R7402-20

For Photon Counting (P Type)				
Type No.	Gain		Dark Count (f) (s^{-1})	
	Min.	Typ.	Typ.	Max.
R7400P	7.5×10^5	1×10^6	80	400
R7401P	7.5×10^5	1×10^6	80	400

Figure 4: Typical Gain Characteristics

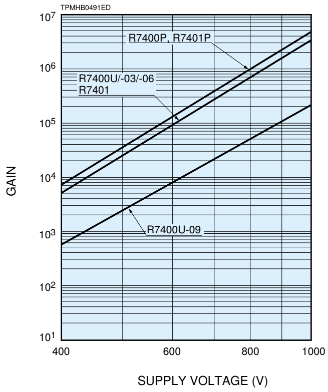

Figure 5: Typical Gain Characteristics

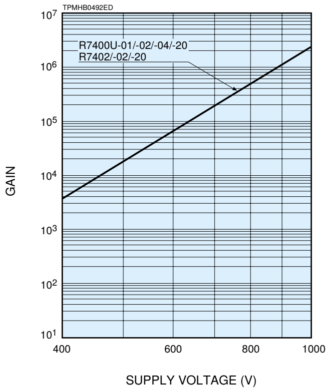

Figure 6: Anode Dark Current (v.s. Supply Voltage)

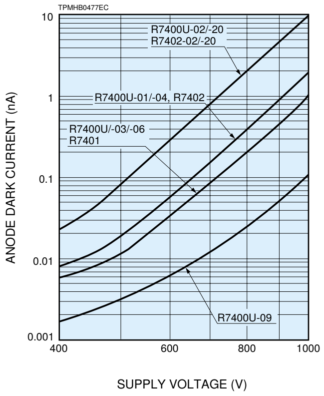

Figure 7: Anode Dark Current (v.s. Temperature)

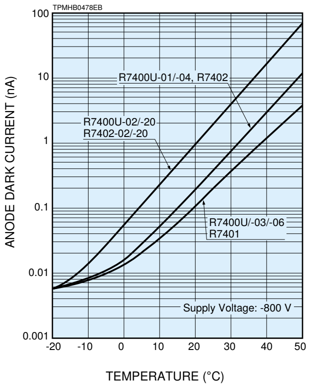

METAL PACKAGE PHOTOMULTIPLIER TUBE R7400U SERIES

Figure 8: Transmittance of Lens

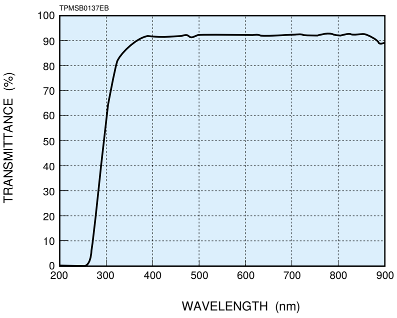

Figure 9: Lens Effect

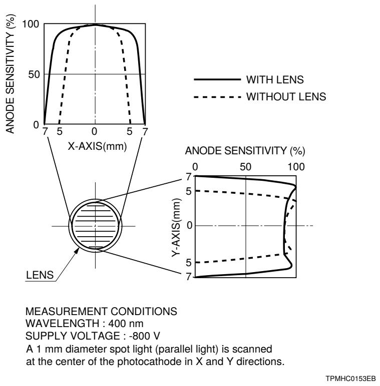

MEASUREMENT CONDITIONS
WAVELENGTH : 400 nm
SUPPLY VOLTAGE : -800 V
A 1 mm diameter spot light (parallel light) is scanned
at the center of the photocathode in X and Y directions.

Figure 10: Lens Effect

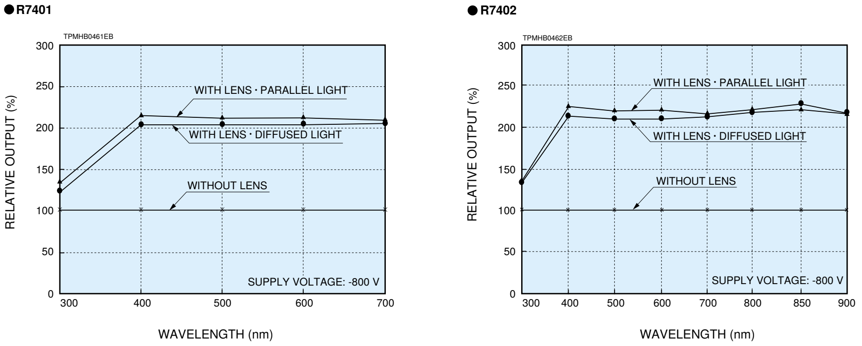

Parallel light : Parallel light from a 40 mm diameter parallel light source insuring uniform intensity over the entire active area of the photomultiplier tube.
Diffused light: Diffused light from a 40 mm diameter parallel light source and a diffuser placed 10cm from the detector. The entire active area of the PMT is exposed.

Figure 11: Dimensional Outline and Basing Diagram (Unit: mm)

1 R7400U/ -01/ -02/ -03/ -04/ -20, R7400P

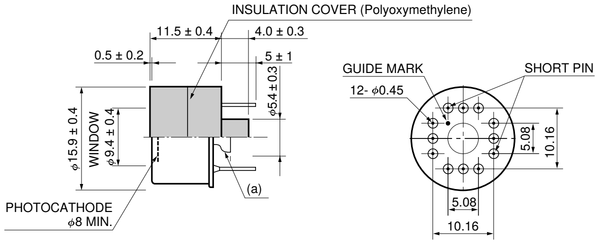

Side View **Bottom View**

(a) The R7400U-01, -02, -04 and -20 do not have.

2 R7400U-06/ -09

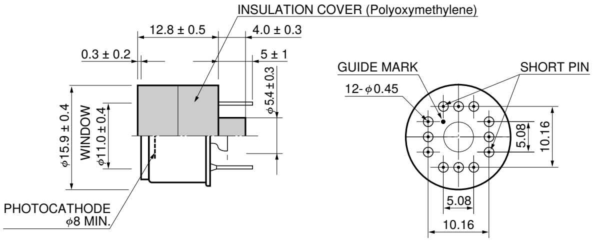

Side View **Bottom View**

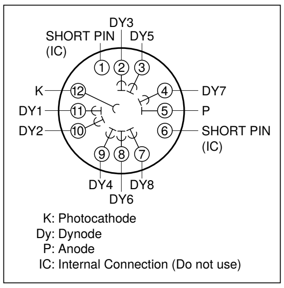

3 R7401, R7401P, R7402/ -02/ -20

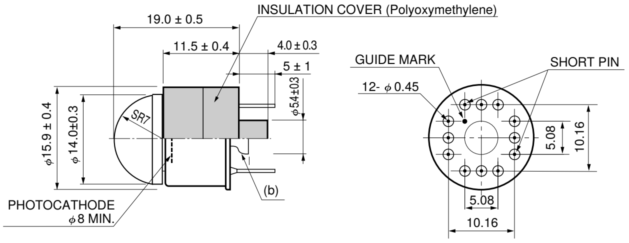

Side View **Bottom View**

(b) The R7402, -02, and -20 do not have.

METAL PACKAGE PHOTOMULTIPLIER TUBE R7400U SERIES

ACCESSORIES (Unit: mm) SOLD SEPARATELY

● Socket E678-12M

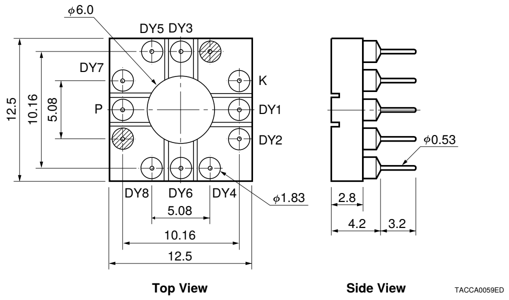

● D Type Socket Assemblies E5770/E5780

These are current-output type, small socket assemblies with an internal voltage divider circuit, specifically designed for use with the R7400U series.

Type No.	Grounded Electrode	Divider Resistance (Total)	Maximum Linear Output of Photomultiplier Tube (DC Mode)	Operating Ambient Temperature[c]	Storage Temperature[c]	Output Signal	
						Cathode Grounded	Anode Grounded
E5770[a]	Anode/Cathode	2.8 MΩ	13 μA	0 °C to +50 °C	-15 °C to +60 °C	Pulse	DC/Pulse
E5780[b]	Anode					—	DC/Pulse

(a): When operating the E5770 with the cathode grounded (positive high voltage applied to the anode), use a high-voltage resistant capacitor to isolate the signal from the positive high voltage.
(b): The E5780 must be operated with the anode grounded (negative high voltage applied to the cathode). If you need a variant type operating with the cathode grounded (positive high voltage applied to the anode), then consult with our sales office.
(c): No condensation

PC-board Mounting Type E5770

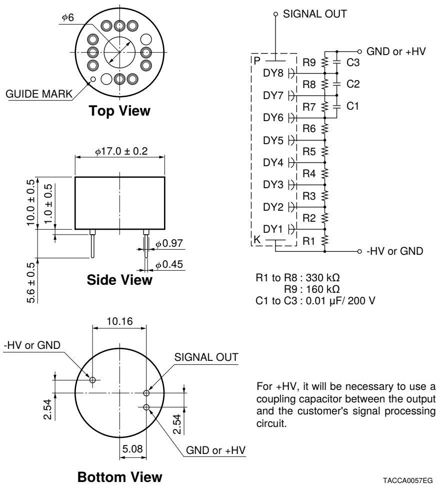

For +HV, it will be necessary to use a coupling capacitor between the output and the customer's signal processing circuit.

Cable Output Type E5780

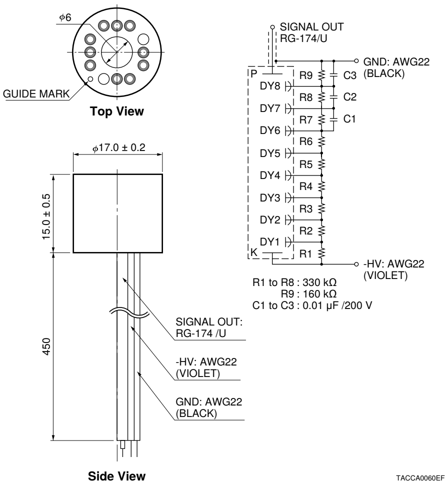

● DA Type Socket Assembly C5781

The C5781 is a subminiature socket assembly that incorporates a voltage divider circuit and a low-noise amplifier.

SPECIFICATIONS of Built-in Amplifier

Parameter		Value	Unit
Input Voltage for Amplifier		±15	V
Current to Voltage Conversion Factor		1	V/μA
Maximum Output Voltage (with no load resistor)		10	V
Bandwidth (-3 db)	Typ.	DC to 20	kHz
Operating Ambient Temperature [(a)]		0 to +40	°C
Storage Temperature [(a)]		-15 to +60	°C

(a): No condensation

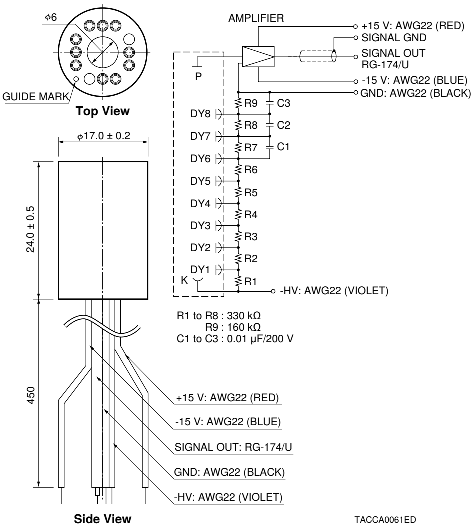

● Compact High Voltage Power Supply Units C4900 Series

The C4900 series is an on-board type high voltage power supply unit, with a design that aims at providing both “compactness and high performance”.

The newly developed circuit achieves high performance and low power consumption. The C4900 series in addition provides enhanced protective functions yet is offered at lower costs.

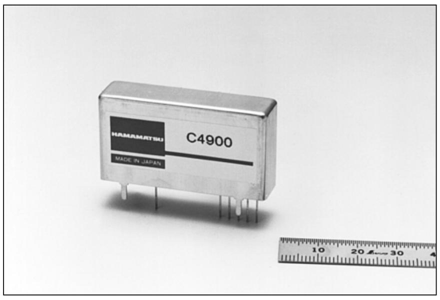

SPECIFICATIONS

Parameter		C4900	C4900-01	C4900-50	C4900-51
Input Voltage		+15 V	+12 V	+15 V	+12 V
Input Current [(a)]	1	14 mA	15 mA	14 mA	15 mA
	2	90 mA	95 mA	90 mA	95 mA
Variable Output Range		0 V to -1250 V		0 V to +1250 V	
Maximum Output Current		0.6 mA	0.5 mA	0.6 mA	0.5 mA
Ripple Noise (p-p)		0.007 % Typ.			
Line Regulation [(b)]		±0.01 % Typ.			
Load Regulation [(c)]		±0.01 % Typ.			
Operating Ambient Temperature [(d)]		0 °C to +50 °C			
Storage Temperature		-20 °C to +70 °C			
Dimension [(e)] (W×H×D)		46 mm × 24 mm × 12 mm			

1 With No Load
2 With Full Load
(a): At Maximum Output Voltage.
(b): Against ±1 V Change.
(c): Against 0 to 100 % Load Change.
(d): At Maximum Output Voltage and Current.
(e): Excluding Projecting Parts

METAL PACKAGE PHOTOMULTIPLIER TUBE R7400U SERIES

WARNING: HIGH VOLTAGE

HIGH VOLTAGE

The metal package photomultiplier tubes are operated by applying a high voltage. Use extreme caution to avoid electrical shock and damage to the peripheral equipment and be sure to provide adequate safety measures as needed. As safety measures, an insulation cover is fitted to the metal package which is electrically connected to the photocathode. When operated with the cathode at a high voltage (anode ground scheme), the metal package will be at this same high voltage level. Removing the insulation cover is extremely dangerous, so never attempt to remove it from the package.

RELATED PRODUCTS

PHOTOSENSOR MODULES H5773/H5783/H6779/H6780/H5784 SERIES

The H5773/H5783/H6779/H6780 series are photosensor modules that incorporate a metal package PMT along with a high-voltage power supply. These photosensor modules operate from a low-voltage supply (+15 V: H5773/H5783/H6779/H6780 series, -15 V: H5784 series) and feature higher sensitivity, wider dynamic range and faster time response compared to conventional photosensors.
The H5773 and H6779 series photosensor modules are a lead pin output type that can be directly mounted on a PC board. The H5783 and H6780 series photosensor modules are a flexible cable output type. The H5784 series is also a cable output type that further contains a low-noise amplifier circuit (DC to 20 kHz). When used with an optional optical fiber adapter (E5776), light can be directly guided to the photosensitive surface through an optical fiber.

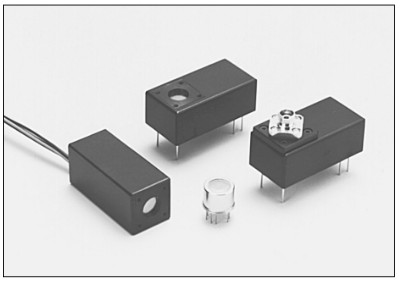

Left: H6780   Center: H6779 Right: H6779 with E5776
Front: METAL PACKAGE PMT

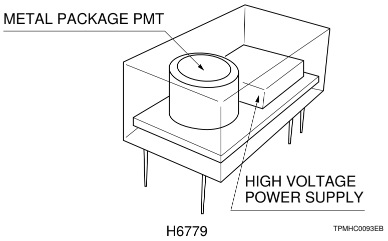

FEATURES

- **Low Power Consumption**
- **Low Voltage Drive**
- **Easy to Use**
- **High Sensitivity**
- **Wide Dynamic Range**
- **Fast Time Response**

H5773, H6779 Series: SIZE 25(W) × 18(H) × 50(D) mm WEIGHT: 60 g
H5783, H6780 Series: SIZE 22(W) × 22(H) × 50(D) mm WEIGHT: 80 g
H5784 Series : SIZE 22(W) × 22(H) × 60(D) mm WEIGHT: 100 g

*PATENT: USA: 5410211 and other(9), GBR: 551767 and other(9), DEU: 69209809 and other(9), FRA: 551767 and other(9), JPN: 3078905 and other(9)

HAMAMATSU
WEB SITE http://www.hamamatsu.com
HAMAMATSU PHOTONICS K.K., Electron Tube Division
314-5, Shimokanzo, Toyooka-village, Iwata-gun, Shizuoka-ken, 438-0193, Japan, Telephone: (81)539/62-5248, Fax: (81)539/62-2205
U.S.A.: Hamamatsu Corporation: 360 Foothill Road, P. O. Box 6910, Bridgewater. N.J. 08807-0910, U.S.A., Telephone: (1)908-231-0960, Fax: (1)908-231-1218 E-mail: usa@hamamatsu.com
Germany: Hamamatsu Photonics Deutschland GmbH: Arzbergerstr. 10, D-82211 Herrsching am Ammersee, Germany, Telephone: (49)8152-375-0, Fax: (49)8152-2658 E-mail: info@hamamatsu.de
France: Hamamatsu Photonics France S.A.R.L.: 8, Rue du Saule Trapu, Parc du Moulin de Massy, 91882 Massy Cedex, France, Telephone: (33)1 69 53 71 00, Fax: (33)1 69 53 71 10 E-mail: infos@hamamatsu.fr
United Kingdom: Hamamatsu Photonics UK Limited: 2 Howard Court, 10 Tewin Road Welwyn Garden City Hertfordshire AL7 1BW, United Kingdom, Telephone: 44-(0)1707-294888, Fax: 44(0)1707-325777 E-mail: info@hamamatsu.co.uk
North Europe: Hamamatsu Photonics Norden AB: Smidesvägen 12, SE-171-41 SOLNA, Sweden, Telephone: (46)8-509-031-00, Fax: (46)8-509-031-01 E-mail: info@hamamatsu.se
Italy: Hamamatsu Photonics Italia: S.R.L.: Strada della Moia, 1/E, 20020 Arese, (Milano), Italy, Telephone: (39)02-935 81 733, Fax: (39)02-935 81 741 E-mail: info@hamamatsu.it
TPMH1204E07
MAY 2004 IP
(1000)

APPENDIX D

Positioning and geometry of tagger scintillators

Scintillator positioning and geometry for the tagger hodoscope. The origin of the coordinate system is given by the middle of the lower edge of the beginning of the dipole magnet as shown in figure D.1. α is the angle between the the y-axis and the scintillator surface defined by Δx and Δz.

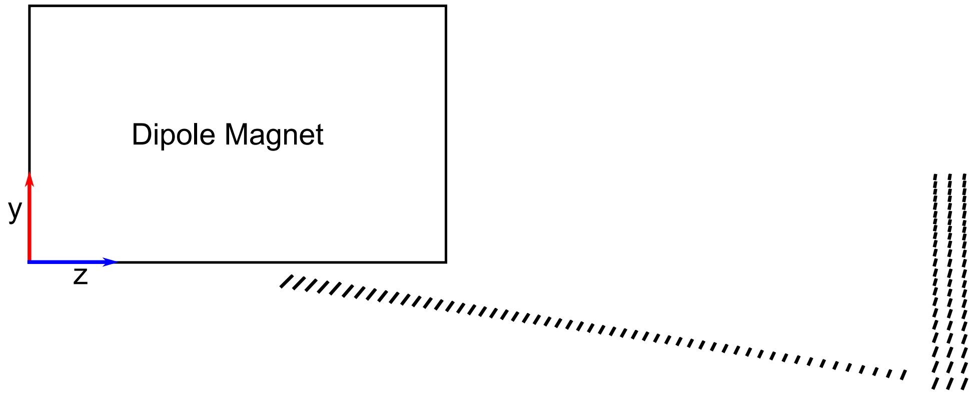

Figure D.1: Scintillator positioning and geometry for the tagger hodoscope.

index	x in cm	y in cm	z in cm	Δx in cm	Δy in cm	Δz in cm	α in deg
0	0.000	-4.923	99.598	6.200	0.500	3.400	45.211
1	0.000	-5.303	102.149	6.200	0.500	3.300	44.222
2	0.000	-5.723	104.632	6.200	0.500	3.100	43.298
3	0.000	-6.102	107.117	6.200	0.500	3.000	42.429
4	0.000	-6.402	109.632	6.200	0.500	3.100	41.610
5	0.000	-6.918	112.215	6.200	0.500	3.000	40.839
6	0.000	-7.226	114.665	6.200	0.500	2.800	40.033
7	0.000	-7.600	117.036	6.200	0.500	2.700	39.342
8	0.000	-7.976	119.389	6.200	0.500	2.600	38.685
9	0.000	-8.307	121.753	6.200	0.500	2.600	38.059
10	0.000	-8.680	124.069	6.200	0.500	2.500	37.463
11	0.000	-9.048	126.366	6.200	0.500	2.400	36.891
12	0.000	-9.379	128.679	6.200	0.500	2.400	36.346
13	0.000	-9.748	130.949	6.200	0.500	2.300	35.822
14	0.000	-10.076	133.234	6.200	0.500	2.300	35.319

Table D.1: Positioning and geometry of the tagger scintillators.

index	x in cm	y in cm	z in cm	Δx in cm	Δy in cm	Δz in cm	α in deg
15	0.000	-10.444	135.480	6.200	0.500	2.200	34.834
16	0.000	-10.772	137.745	6.200	0.500	2.200	34.369
17	0.000	-11.141	139.975	6.200	0.500	2.100	33.919
18	0.000	-11.466	142.224	6.200	0.500	2.100	33.484
19	0.000	-11.791	144.462	6.200	0.500	2.100	33.064
20	0.000	-12.163	146.674	6.200	0.500	2.000	32.658
21	0.000	-12.491	148.912	6.200	0.500	2.000	32.263
22	0.000	-12.816	151.143	6.200	0.500	2.000	31.879
23	0.000	-13.186	153.344	6.200	0.500	1.900	31.507
24	0.000	-13.517	155.576	6.200	0.500	1.900	31.144
25	0.000	-13.847	157.810	6.200	0.500	1.900	30.790
26	0.000	-14.176	160.044	6.200	0.500	1.900	30.445
27	0.000	-14.548	162.251	6.200	0.500	1.800	30.108
28	0.000	-14.887	164.498	6.200	0.500	1.800	29.780
29	0.000	-15.220	166.750	6.200	0.500	1.800	29.457
30	0.000	-15.559	169.012	6.200	0.500	1.800	29.141
31	0.000	-15.895	171.277	6.200	0.500	1.800	28.830
32	0.000	-16.237	173.555	6.200	0.500	1.800	28.528
33	0.000	-16.628	175.828	6.200	0.500	1.700	28.230
34	0.000	-16.969	178.128	6.200	0.500	1.700	27.935
35	0.000	-17.319	180.446	6.200	0.500	1.700	27.649
36	0.000	-17.674	182.788	6.200	0.500	1.700	27.366
37	0.000	-18.028	185.144	6.200	0.500	1.700	27.086
38	0.000	-18.389	187.524	6.200	0.500	1.700	26.811
39	0.000	-18.750	189.922	6.200	0.500	1.700	26.539
40	0.000	-19.116	192.341	6.200	0.500	1.700	26.271
41	0.000	-19.488	194.788	6.200	0.500	1.700	26.008
42	0.000	-19.906	197.234	6.200	0.500	1.600	25.747
43	0.000	-20.285	199.731	6.200	0.500	1.600	25.491
44	0.000	-20.670	202.259	6.200	0.500	1.600	25.238
45	0.000	-21.057	204.813	6.200	0.500	1.600	24.987
46	0.000	-21.456	207.410	6.200	0.500	1.600	24.740
47	0.000	-21.856	210.039	6.200	0.500	1.600	24.495
48	0.000	-22.259	212.696	6.200	0.500	1.600	24.252
49	0.000	-22.671	215.393	6.200	0.500	1.600	24.014
50	0.000	-23.090	218.131	6.200	0.500	1.600	23.777
51	0.000	-23.512	220.904	6.200	0.500	1.600	23.543
52	0.000	-23.942	223.717	6.200	0.500	1.600	23.313
53	0.000	-24.199	226.663	6.200	0.500	2.000	23.085
54	0.000	-25.970	233.237	6.200	0.500	2.400	22.858
55	0.000	-26.022	236.241	6.200	0.500	2.400	22.523
56	0.000	-26.069	239.244	6.200	0.500	2.400	22.194
57	0.000	-22.549	233.248	6.200	0.500	2.300	21.871
58	0.000	-22.639	236.249	6.200	0.500	2.300	21.554
59	0.000	-22.762	239.232	6.200	0.500	2.200	21.240

Table D.2: Positioning and geometry of the tagger scintillators.

index	x in cm	y in cm	z in cm	Δx in cm	Δy in cm	Δz in cm	α in deg
60	0.000	-19.439	233.235	6.200	0.500	2.100	20.932
61	0.000	-19.553	236.237	6.200	0.500	2.100	20.630
62	0.000	-19.660	239.239	6.200	0.500	2.100	20.334
63	0.000	-16.529	233.239	6.200	0.500	2.000	20.043
64	0.000	-16.667	236.240	6.200	0.500	2.000	19.758
65	0.000	-16.843	239.226	6.200	0.500	1.900	19.476
66	0.000	-13.884	233.226	6.200	0.500	1.800	19.202
67	0.000	-14.047	236.228	6.200	0.500	1.800	18.933
68	0.000	-14.203	239.229	6.200	0.500	1.800	18.671
69	0.000	-11.405	233.227	6.200	0.500	1.700	18.412
70	0.000	-11.586	236.229	6.200	0.500	1.700	18.159
71	0.000	-11.760	239.230	6.200	0.500	1.700	17.912
72	0.000	-9.113	233.228	6.200	0.500	1.600	17.670
73	0.000	-9.314	236.228	6.200	0.500	1.600	17.433
74	0.000	-9.505	239.229	6.200	0.500	1.600	17.200
75	0.000	-6.994	233.227	6.200	0.500	1.500	16.973
76	0.000	-7.259	236.213	6.200	0.500	1.400	16.751
77	0.000	-7.425	239.244	6.200	0.500	1.500	16.534
78	0.000	-5.091	233.209	6.200	0.500	1.400	16.336
79	0.000	-5.269	236.225	6.200	0.500	1.400	16.115
80	0.000	-5.493	239.226	6.200	0.500	1.400	15.912
81	0.000	-3.134	233.249	6.200	0.500	1.500	15.714
82	0.000	-3.269	236.227	6.200	0.500	1.700	15.520
83	0.000	-3.361	239.216	6.200	0.500	1.600	15.269
84	0.000	-1.038	233.215	6.200	0.500	1.500	15.025
85	0.000	-1.117	236.217	6.200	0.500	1.500	14.789
86	0.000	-1.191	239.219	6.200	0.500	1.500	14.558
87	0.000	0.987	233.217	6.200	0.500	1.400	14.335
88	0.000	0.883	236.218	6.200	0.500	1.400	14.117
89	0.000	0.782	239.220	6.200	0.500	1.400	13.906
90	0.000	2.828	233.217	6.200	0.500	1.300	13.701
91	0.000	2.699	236.219	6.200	0.500	1.300	13.502
92	0.000	2.575	239.219	6.200	0.500	1.300	13.308
93	0.000	4.502	233.216	6.200	0.500	1.200	13.120
94	0.000	4.355	236.217	6.200	0.500	1.200	12.937
95	0.000	4.212	239.218	6.200	0.500	1.200	12.758
96	0.000	6.033	233.214	6.200	0.500	1.100	12.585
97	0.000	5.871	236.214	6.200	0.500	1.100	12.415
98	0.000	5.713	239.215	6.200	0.500	1.100	12.251
99	0.000	7.437	233.211	6.200	0.500	1.000	12.090
100	0.000	7.262	236.211	6.200	0.500	1.000	11.934
101	0.000	7.091	239.212	6.200	0.500	1.000	11.782
102	0.000	8.875	233.237	6.200	0.500	1.200	11.633
103	0.000	8.795	236.217	6.200	0.500	1.400	11.488
104	0.000	8.824	239.218	6.200	0.500	1.400	11.278

Table D.3: Positioning and geometry of the tagger scintillators.

index	x in cm	y in cm	z in cm	Δx in cm	Δy in cm	Δz in cm	α in deg
105	0.000	10.564	233.217	6.200	0.500	1.300	11.074
106	0.000	10.509	236.209	6.200	0.500	1.200	10.878
107	0.000	10.504	239.210	6.200	0.500	1.200	10.689
108	0.000	12.119	233.208	6.200	0.500	1.100	10.506
109	0.000	12.086	236.209	6.200	0.500	1.100	10.329
110	0.000	12.054	239.210	6.200	0.500	1.100	10.158
111	0.000	13.557	233.213	6.200	0.500	1.000	9.993
112	0.000	13.517	236.211	6.200	0.500	1.100	9.841
113	0.000	13.548	239.226	6.200	0.500	1.200	9.677
114	0.000	15.009	233.208	6.200	0.500	1.200	9.527
115	0.000	15.074	236.210	6.200	0.500	1.200	9.333
116	0.000	15.137	239.211	6.200	0.500	1.200	9.148
117	0.000	16.567	233.209	6.200	0.500	1.100	8.969
118	0.000	16.597	236.211	6.200	0.500	1.100	8.798
119	0.000	16.625	239.212	6.200	0.500	1.100	8.633

Table D.4: Positioning and geometry of the tagger scintillators.

APPENDIX E

Coincidence channel to energy conversion for the tagger hodoscope

Dependency between the tagger coincidence channel and the energy of the post-bremsstrahlung electron E_{e^-} normalised to the primary electron beam energy E_0

$$\begin{aligned} E_{e^-} \text{ in } \%E_0 &= 0.91075 \text{ for channel } 119 \\ &= -1.12297 + 0.01706 \cdot x \text{ for channel } 114 \;-\; 118 \\ &= -0.61927 + 0.01262 \cdot x \text{ for channel } 103 \;-\; 113 \\ &= -0.19098 + 0.00845 \cdot x \text{ for channel } 82 \;-\; 102 \\ &= -0.01554 + 0.0063 \cdot x \text{ for channel } 54 \;-\; 81 \\ &= 0.09768 + 0.00418 \cdot x \text{ for channel } 1 \;-\; 53 \end{aligned} \tag{E.1}$$

APPENDIX F

Data points of the photon beam asymmetry in π^0 photo-production off the proton

The results of the photon beam asymmetry $\Sigma_{3\sigma}$ in π^0 photo-production off the proton are listed in table F.1. The errors $\sigma\Sigma_{3\sigma}$ result from the fit of the azimuthal modulations and are based on statistics. Additionally, the results of the photon beam asymmetry $\Sigma_{2\sigma}$ with reduced size of the kincematical cuts are listed together with their errors $\sigma\Sigma_{2\sigma}$. The value $\Delta\Sigma_{3\sigma-2\sigma}$ indicates the difference between the results of the photon beam asymmetry with nominal and reduced size of the kinematical cuts.

E_γ in MeV	θ_{cms} in degree	$\Sigma_{3\sigma}$	$\sigma\Sigma_{3\sigma}$	$\Sigma_{2\sigma}$	$\sigma\Sigma_{2\sigma}$	$\Delta\Sigma_{3\sigma-2\sigma}$
1125±25	60	0.8807	0.1273	0.9398	0.1769	-0.0591
	80	0.0962	0.1309	0.2313	0.1657	-0.1352
	100	-0.9001	0.1463	-1.0794	0.1701	0.1793
	120	-0.6633	0.1353	-0.6055	0.1520	-0.0578
	140	-0.4633	0.1605	-0.3714	0.1765	-0.0919
1175±25	60	0.9353	0.1303	1.0241	0.1784	-0.0888
	80	0.2118	0.1271	0.3706	0.1612	-0.1588
	100	-0.7366	0.1481	-0.7521	0.1717	0.0155
	120	-0.3446	0.1395	-0.4731	0.1556	0.1285
	140	-0.1884	0.1623	-0.1669	0.1799	-0.0215
1225±25	60	0.9175	0.1285	1.0934	0.1832	-0.1759
	80	0.2983	0.1199	0.2941	0.1565	0.0042
	100	-0.7143	0.1387	-0.6824	0.1624	-0.0319
	120	-0.5564	0.1272	-0.5139	0.1438	-0.0425
	140	-0.1668	0.1400	-0.1256	0.1552	-0.0412
1275±25	60	1.1650	0.1357	1.2106	0.1932	-0.0456
	80	0.7279	0.1127	0.8435	0.1410	-0.1156
	100	-0.2329	0.1306	-0.2819	0.1552	0.0490
	120	-0.2648	0.1240	-0.1550	0.1402	-0.1098
	140	0.3490	0.1242	0.4295	0.1390	-0.0805
1325±25	60	0.8270	0.1286	0.8080	0.1930	0.0190
	80	0.5301	0.0977	0.6198	0.1257	-0.0897
	100	-0.1969	0.1156	-0.2099	0.1316	0.0130
	120	-0.0965	0.1034	-0.2099	0.1183	0.1135
	140	0.4334	0.1038	0.4251	0.1155	0.0082

E_γ in MeV	θ_{cms} in degree	$\Sigma_{3\sigma}$	$\sigma\Sigma_{3\sigma}$	$\Sigma_{2\sigma}$	$\sigma\Sigma_{2\sigma}$	$\Delta\Sigma_{3\sigma-2\sigma}$
1375±25	60	0.8234	0.1190	0.7274	0.1707	0.0960
	80	0.6380	0.0814	0.7340	0.1070	-0.0959
	100	0.2458	0.0921	0.3149	0.1121	-0.0691
	120	0.2312	0.0880	0.2932	0.0998	-0.0620
	140	0.4940	0.0855	0.5581	0.0930	-0.0642
1425±25	60	1.0285	0.1214	1.0557	0.1756	-0.0272
	80	0.5747	0.0729	0.6419	0.0947	-0.0672
	100	0.3268	0.0750	0.4044	0.0904	-0.0776
	120	0.3163	0.0768	0.3942	0.0876	-0.0779
	140	0.5768	0.0758	0.6630	0.0846	-0.0862
1475±25	60	0.6011	0.1582	0.5674	0.2359	0.0337
	80	0.5545	0.0835	0.5571	0.1106	-0.0026
	100	0.4084	0.0832	0.4612	0.1026	-0.0528
	120	0.5385	0.0916	0.6374	0.1026	-0.0989
	140	0.6319	0.0883	0.6443	0.0989	-0.0125

Table F.1: Photon beam asymmetry Σ in π^0 photo-production off the proton

APPENDIX G

Data points of the photon beam asymmetry in η photo-production off the proton

The results of the photon beam asymmetry $\Sigma_{3\sigma}$ in η photo-production off the proton are listed in table G.1. The errors $\sigma\Sigma_{3\sigma}$ result from the fit of the azimuthal modulations and are based on statistics. Additionally, the results of the photon beam asymmetry $\Sigma_{2\sigma}$ with reduced size of the kincematical cuts are listed together with their errors $\sigma\Sigma_{2\sigma}$. The value $\Delta\Sigma_{3\sigma-2\sigma}$ indicates the difference between the results of the photon beam asymmetry with nominal and reduced size of the kinematical cuts.

E_γ in MeV	θ_{cms} in degree	$\Sigma_{3\sigma}$	$\sigma\Sigma_{3\sigma}$	$\Sigma_{2\sigma}$	$\sigma\Sigma_{2\sigma}$	$\Delta\Sigma_{3\sigma-2\sigma}$
1150±50	62.5	0.7096	0.2543	0.5737	0.3152	0.1359
	90	0.4154	0.2191	0.5272	0.2476	-0.1118
	117.5	0.1981	0.2748	0.5119	0.3034	-0.3137
1250±50	62.5	0.4854	0.2125	0.5093	0.2742	-0.0238
	90	1.1765	0.1826	1.3805	0.2107	-0.2040
	117.5	-0.0541	0.2311	0.1703	0.2521	-0.2244
1350±50	62.5	0.4159	0.1741	0.3643	0.2294	0.0516
	90	0.8965	0.1488	1.0642	0.1706	-0.1677
	117.5	0.4626	0.1927	0.4618	0.2101	0.0008
1475±75	62.5	0.7802	0.1319	0.7890	0.1780	-0.0088
	90	0.6165	0.1132	0.8110	0.1344	-0.1945
	117.5	0.5722	0.1458	0.8128	0.1623	-0.2407

Table G.1: Photon beam asymmetry Σ in η photo-production off the proton

Bibliography

[1] K. Livingston,
The Stonehenge Technique. A method for aligning coherent bremsstrahlung radiators,
Nucl. Instrum. Methods A **603** (2009) 205–213 (cit. on pp. iii, 59, 89).

[2] A. Bella, *Setup of a Goniometer System for the Production of Linearly Polarised Photons for the BGO-OD Experiment at ELSA*, Diploma Thesis: University of Bonn, 2011
(cit. on pp. iii, 68, 90).

[3] URL: `http://pwa.hiskp.uni-bonn.de/baryon_x.htm` (cit. on pp. iii, 3, 73).

[4] K. A. Olive et al., *Review of Particle Physics*, Chinese Physics C **38** (2014) (cit. on p. 2).

[5] O. Bartholomy et al.,
Neutral-Pion Photoproduction off Protons in the Energy Range 0.3 GeV > E_γ > 3 GeV,
Phys. Rev. Lett. **94** (2005) 012003 (cit. on p. 2).

[6] E. F. McNicoll et al., *Experimental study of the $\gamma p \rightarrow \eta p$ reaction with the Crystal Ball detector at the Mainz Microtron (MAMI-C)*, Phys. Rev. C **82** (2010) 035208 (cit. on p. 2).

[7] M. Fuchs, *Photoproduktion neutraler Pionpaare mit dem Crystal-Barrel-Detektor an ELSA*,
Phd Thesis: University of Bonn, 2005 (cit. on p. 2).

[8] C. Wu et al., *Photoproduction of ρ-mesons and Δ-baryons in the reaction $\gamma p \rightarrow p\pi^+\pi^-$ at $\sqrt{s}$ energies up to $s = 2.6$ GeV*,
The European Physical Journal A - Hadrons and Nuclei **23.2** (2005) 317–344 (cit. on p. 2).

[9] R. Bradford et al., *Differential cross sections for $\gamma + p \rightarrow K^+ + Y$ for Λ and Σ^0 hyperons*,
Phys. Rev. C **73** (2006) 035202 (cit. on p. 2).

[10] W.-T. Chiang and F. Tabakin,
Completeness rules for spin observables in pseudoscalar meson photoproduction,
Phys. Rev. C **55** (1997) 2054–2066 (cit. on p. 2).

[11] H. Schmieden, *Photoproduction of ω-Mesons at ELSA and the Role of Azimuthal Asymmetries*,
Chinese Physics C **33** (2009) 1146–1152 (cit. on p. 3).

[12] M. Burkardt, C. Miller and W.-D. Nowak,
Spin-polarized high-energy scattering of charged leptons on nucleons, arXiv (0812.2208 2009)
(cit. on p. 3).

[13] A. V. Anisovich et al.,
Properties of baryon resonances from a multichannel partial wave analysis,
The European Physical Journal A **48** (2012) 1–13 (cit. on p. 3).

[14] S.-K. Choi et al.,
Observation of a Narrow Charmoniumlike State in Exclusive $B^\pm \rightarrow K^\pm\pi^+\pi^- J/\Psi$ Decays,
Phys. Rev. Lett. **91** (2003) 262001 (cit. on p. 4).

[15] R. Aaij et al.,
Observation of J/Ψ Resonances Consistent with Pentaquark States in $\Lambda_b^0 \to J/\Psi K^- P$ Decays,
Phys. Rev. Lett. **115** (2015) 072001 (cit. on p. 4).

[16] R. Ewald et al., *Anomaly in the photoproduction cross section off the proton at the threshold*,
Physics Letters B **713** (2012) 180–185 (cit. on p. 4).

[17] U. Timm, *Coherent Bremsstrahlung in Crystals*, Fortschritte der Physik **17** (1969) 765–808
(cit. on pp. 7, 9, 10, 12, 15–19).

[18] E. Haug, *The elementary process of Bremsstrahlung*, World Scientific, 2004 (cit. on pp. 7, 10).

[19] L. Landau and E. Lifschitz, *Lehrbuch der theoretischen Physik*, Akademie-Verlag, 1986
(cit. on pp. 7, 11).

[20] H. Überall, *High-Energy Interference Effect of Bremsstrahlung and Pair Production in Crystals*,
Phys. Rev. **103** (1956) 1055–1067 (cit. on p. 9).

[21] D. Elsner, *Untersuchung kleiner Partialwellenbeiträge in der Nähe dominierender Resonanzzustände des Protons mit linear polarisierten Photonen*,
Dissertation: University of Bonn, 2007 (cit. on p. 11).

[22] R. Mößbauer, *Kernresonanzfluoreszenz von Gammastrahlung in Ir*^{191},
Zeitschrift für Physik **151** (1958) 124–143 (cit. on p. 11).

[23] C. Kittel, *Einführung in die Festkörperphysik*, Oldenbourg Wissenschaftsverlag, 2006
(cit. on p. 12).

[24] M. von Laue, *Röntgenstrahlinterferenzen*, Akademische Verlagsgesellschaft, 1960
(cit. on p. 13).

[25] G. Diambrini, *High-Energy Bremsstrahlung and Electron Pair Production in Thin Crystals*,
Rev. Mod. Phys. **40** (1968) 611–631 (cit. on p. 15).

[26] J. Wheeler and W. Lamb, *Influence of Atomic Electrons on Radiation and Pair Production*,
Phys. Rev. **55** (1939) 858 (cit. on p. 16).

[27] H. Bethe, *The influence of screening on the creation and stopping of electrons*,
Phil. Soc. **30** (1934) 524–539 (cit. on p. 19).

[28] B. Reitz, *Erzeugung linear polarisierter Photonen für das BGO-OD-Experiment*,
Bachelor Thesis: University of Bonn, 2013, URL: `https://www.hsag.physik.uni-bonn.de/forschung/diplom-doktorarbeiten/bachelorarbeiten` (cit. on p. 25).

[29] T. Zimmermann, *Circularly polarised photons at the BGO-OD experiment at ELSA*,
Phd Thesis: University of Bonn, in preparation (cit. on p. 25).

[30] K. Fornet-Ponse,
Die Photonenmarkierungsanlage für das Crystal-Barrel/TAPS-Experiment an ELSA,
Phd Thesis: University of Bonn, 2009, URL: `https://www.hsag.physik.uni-bonn.de/forschung/diplom-doktorarbeiten/doktorarbeiten` (cit. on pp. 25, 26).

[31] T. Zimmermann, *Photon Flux Monitor for the BGO-OD experiment*,
Diploma Thesis: University of Bonn, 2012 (cit. on pp. 27, 28).

[32] M. Romaniuk, *Target system*, BGO-OD internal note **BGO-OD-016-2012** (2012) (cit. on p. 28).

[33] A. Braghieri,
The Project for a new set of 2-Multi Wire Proportional Chamber for the B1 Collaboration
(2009) (cit. on p. 29).

[34] URL: `https://bgo-od.physik.uni-bonn.de/ExperimentalSetup/BgoBall` (cit. on p. 29).

[35] A. Zucchiatti et al., *Optimization of response of BGO sectors for a 4π electromagnetic calorimeter*, Nucl. Instrum. Methods A **317** (1992) 492–497 (cit. on p. 30).

[36] M. Castoldi et al., *The temperature monitoring system of a BGO calorimeter*, Nucl. Instrum. Methods A **403** (1998) 22–30 (cit. on p. 30).

[37] P. Levi Sandri et al., *Performance of a BGO calorimeter in a tagged photon beam from 260 to 1150 MeV*, Nucl. Instrum. Methods A **370** (1996) 396–402 (cit. on p. 30).

[38] F. Ghio et al., *The GRAAL high resolution BGO calorimeter and its energy calibration and monitoring system*, Nucl. Instrum. Methods A **404** (1998) 71–86 (cit. on p. 30).

[39] R. Joosten, *Aufbau und Inbetriebnahme eines hochgranularen Vertexdetektors aus szintilierenden Fasern fuer das Experiment MOMO an COSY - Erste Ergebnisse zur Reaktion p + d -> ^{3}He + π^+ + π^-*, Dissertation: University of Bonn, 1996 (cit. on p. 30).

[40] S. Böse, *Aufbau und Test eines neuen Szintillationsfaser-Detektors für das neue Vorwärtsspektrometer an ELSA*, Dissertation: University of Bonn, 2015 (cit. on p. 30).

[41] URL: `https://bgo-od.physik.uni-bonn.de/ExperimentalSetup/Magnet` (cit. on p. 30).

[42] URL: `https://bgo-od.physik.uni-bonn.de/ExperimentalSetup/DriftChamber` (cit. on p. 30).

[43] P. Meiß, *The Time of Flight Spectrometer of the BGO-OD Experiment*, Diploma Thesis: University of Bonn, 2013, URL: `https://www.hsag.physik.uni-bonn.de/forschung/diplom-doktorarbeiten/diplom-masterarbeiten` (cit. on p. 31).

[44] URL: `https://bgo-od.physik.uni-bonn.de/ExperimentalSetup/MRPC` (cit. on p. 31).

[45] G. Scheluchin, *Meson photoproduction on the proton using the BGO-OD detector complemented by a new Scintillating Ring (SciRi)*, Master Thesis: University of Bonn, 2015 (cit. on pp. 31, 75).

[46] D. Hammann, *The data acquisition for the BGO-OD experiment*, Phd Thesis: University of Bonn, 2016 (cit. on p. 31).

[47] J. Bieling, *FPGA module and firmware descriptions*, BGO-OD internal note **BGO-OD-008-2011** (2012) (cit. on p. 31).

[48] G. Siebke, *Design of the BGO-OD Tagging System and Test of a Detector Prototype*, Diploma Thesis: University of Bonn, 2010, URL: `https://www.hsag.physik.uni-bonn.de/forschung/diplom-doktorarbeiten/diplom-masterarbeiten` (cit. on pp. 33, 34, 36, 42, 89).

[49] F. Messi, *The Tagging System of the BGO-OD experiment*, Phd Thesis: University of Bonn, 2015 (cit. on p. 34).

[50] J. Bieling, URL: `https://github.com/jobisoft` (cit. on pp. 35, 73).

[51] H. Eberhardt, *Bestimmung von Polarisationsobservablen in der π^0 und ω Photoproduktion am Proton mit dem CBELSA/TAPS-Experiment*, Dissertation: University of Bonn, 2012 (cit. on p. 66).

[52] URL: `http://www.wiener-d.com/sc/modules/vme--modules/avm16.html` (cit. on p. 74).

[53] N. Sparks et al., *Measurement of the beam asymmetry Σ in the forward direction for $\vec{\gamma} p \to p\pi^0$*, Phys. Rev. C **81** (2010) 065210 (cit. on pp. 83–85, 90).

[54] O. Bartalini et al., *Measurement of η photoproduction on the proton from threshold to 1500 MeV*, The European Physical Journal A **33** (2007) 169–184 (cit. on pp. 83, 84, 86, 90).

List of Figures

List of Tables